

DEVELOPING A MULTI-TONE LOAD-PULL  
SYSTEM FOR THE DIRECT EXTRACTION OF  
CARDIFF BEHAVIOURAL MODEL  
COEFFICIENTS



**AZAM AL-RAWACHY**

DEPARTMENT OF ELECTRICAL ENGINEERING

CARDIFF UNIVERSITY

THIS DISSERTATION IS SUBMITTED FOR THE DEGREE OF

***Doctor of Philosophy***

This thesis is dedicated to my beloved parents

## DECLARATION

This work has not previously been accepted in substance for any degree and is not concurrently submitted in candidature for any degree.

Signed ..... (Candidate)      Date .....

### STATEMENT 1

This thesis is being submitted in partial fulfilment of the requirements for the degree of PhD

Signed ..... (Candidate)      Date .....

### STATEMENT 2

This thesis is the result of my own work/investigation, except where otherwise stated. Other sources are acknowledged by explicit references.

Signed ..... (Candidate)      Date .....

### STATEMENT 3

I hereby give consent for my thesis, if accepted, to be available for photocopying and for inter-library loan, and for the title and summary to be made available to outside organisations.

Signed ..... (Candidate)      Date .....

### STATEMENT 4

I hereby give consent for my thesis, if accepted, to be available for photocopying and for inter-library loans after expiry of a bar on access previously approved by the Graduate Development Committee.

Signed ..... (Candidate)      Date .....

## ACKNOWLEDGEMENT

First and foremost, I thank **Allah**, the Almighty, for keeping my family safe and alive throughout my study at Cardiff University. I lived the most difficult three years in my life where all my family, relatives and friends have lived under the ISIS regime but thank Allah who helped me to remain focused and able to concentrate on my project.

I would like to dedicate my gratitude to the fountain of knowledge **Prof Paul J. Tasker** for his highly intellectual supervision and for devoting the infinite amount of time to share knowledge and thoughts to me. His invaluable support, excellent advice and academic wisdom turn my fear and anxiety to confidence, which helps me a lot to overcome the painful periods in my study.

I would like to profoundly thank my Co-supervisor **Dr James W. Bell**, for his support and knowledge in behavioural modelling, which helps me a lot to understand this complicated topic. He is a friend before being a supervisor who always guides me to the right path. Without his vital support, it would be challenging to finish the project.

Thanks, should also go to the members at the Centre of High Frequency who have been keen to support whenever they ask for. The

head of the department Prof Adrian Porch, Dr Thoalfukar Husseini, Dr Roberto Quaglia, Syed Anera, Kauser Chaudhry, Alex Alt, Kevin and May Estephan.

I am also grateful to RF Engineer Timothy Sileo from National Instrument (NI) for his exceptional support to tackle some problems in LabVIEW code, which would have never been done without his knowledge and cooperation.

There are not enough words to describe how thankful I am to my beloved parents. Thank you for your endless amounts of love. I sincerely thank them for their encouragement, praying, and teaching me to be who I am. Also, my brothers and my sister for their continuous support and encouragement.

My deepest appreciation goes to my beloved wife “Abeer” for sacrificing her life to bring up our children Maryam and Malak, also, for tolerance, patience and understanding to be neglected for most of the time during my journey in this work.

Finally, my sincere thanks and appreciation go to the “Higher Committee for Education Development” (HCED) in Iraq for supporting and funding this project. This work would not be possible without their support. Words cannot express how much their support means to me.

---

## **ABSTRACT**

The main objective of this thesis is to develop and utilize a high-speed measurement system based on PXIe modules for multi-tone measurements. This thesis addresses challenges that have been tackled during developing an accurate LabVIEW software to measure the multi-tone signal. Having solved these problems, the system's functionality was demonstrated by using it to extract some useful data such as stability and gain information for RF designers in, 'real time' during active load-pull measurements. In the final part of the thesis, the system was used to aid the development of the Cardiff behavioural model. One of the main challenges in the development of the Cardiff behavioural model is to correctly select the required mixing terms to have an accurate model. Initial work has been focused on determining the correct, phase polynomial coefficients of the Cardiff Model. The first technique presented in this thesis utilises two-tone measurements and the Fast Fourier Transform (FFT) to observe the mixing order from the resultant intermodulation (IMD) products, which are directly associated with the Cardiff Model coefficients. Employing the IFFT, the selected tones have been transferred to the time-domain travelling-wave. This allowed for b-wave analysis and load modulation coverage to be seen on the Smith Chart. The resultant load-modulation from the two-tone measurements has been used as a target for CW impedance measurements to verify whether the identification holds for the CW domain. The result shows there is an

---

offset between the CW measurements and the two-tone measurements for larger annuli as the  $a_{21}$  exhibits magnitude and phase variation. Nevertheless, the maximum model order, obtained from the two-tone measurements, is acceptable for CW measurements when  $NMSE < -40\text{dBm}$ .

The second technique in this thesis demonstrates the model complexity identification for both magnitude and phase related mixing terms. It utilizes a multi-tone measurements approach. Load-pull measurements are performed using an engineered multi-tone active load-pull excitation,  $A_{21}(t)$ , involving a carrier phase and amplitude modulation components. The tone frequencies are set to a prime number, which, enables clear identification of model complexity of the device response  $B_{21}(t)$ , by avoiding spectral overlap of the associated mixing terms. This is considered an essential step in correctly and accurately modelling the device and the ability to visualize all the intermodulation (IMD) products. Formulating the Cardiff behavioural model in the frequency domain, with this selected multi-tone stimulus, allowed for the first time the direct extraction of the model coefficients. Additionally, formulating the model coefficient least mean square (LMS) extraction process using the FFT transformed data provides for a very robust, direct extraction, solution for model coefficient determination. Utilising the FFT to optimise least mean square (LMS) algorithm for model extraction gives a very robust, direct extraction, solution for model coefficient determination.

## LIST OF PUBLICATIONS

- [1] **A. Al-Rawachy**, T. Hussein, J. Benedikt, P. Tasker, and J. Bell, "Cardiff Behavioural Model Analysis using a Two-Tone Stimulus," in *2019 IEEE Topical Conference on RF/Microwave Power Amplifiers for Radio and Wireless Applications (PAWR)*, 2019, pp. 1-4.
- [2] **A. Al-Rawachy**, T. Hussein, J. Benedikt, J. Bell, and P. Tasker, "Behavioural Model Extraction using Novel Multi-tone Active Load-pull," to be published in *2019 IEEE/MTT-S International Microwave Symposium-IMS*, 2019
- [3] T. Hussein, **A. Al-Rawachy**, J. Benedikt, J. Bel, and P. Tasker, "Automating the Accurate Extraction and Verification of the Cardiff Model via the Direct Measurement of Load-Pull Power Contours," in *2018 IEEE/MTT-S International Microwave Symposium-IMS*, 2018, pp. 544-547.
- [4] T. Hussein, **A. Al-Rawachy**, S. S. Anera, J. Bell, P. Tasker, and J. Benedikt, "On the Effective Modeling of the Test-Set Non-linearity," in *2018 91st ARFTG Microwave Measurement Conference (ARFTG)*, 2018, pp. 1-4.
- [5] T. Hussein, **A. Al-Rawachy**, J. Benedikt, J. Bel, and P. Tasker, "Global Behavioural Model Generation Using Coefficients interpolation," in 2019 to be published in *IEEE/MTT-S International Microwave Symposium-IMS*, 2019.

## LIST OF ABBREVIATION

ADC	Analogue to Digital Converter
ADS	Agilent's Advanced Design System simulation software.
AM-AM	Amplitude to Amplitude Distortion
AM-FM	Amplitude to Phase Distortion
ALP	Active Load-Pull
CAD	Computer-Aided Design
CW	Continuous Wave
DUT	Device Under Test
DWLUT	Direct Wave Look-Up Table.
ESG	Agilent's E-type Signal Generator.
FFT	Fast Fourier Transform
GUI	Graphical User Interface
IC	Integrated Circuit
IFFT	Inverse Fast Fourier Transform
LabVIEW	Laboratory Virtual Instrument Engineering Workbench
LMS	Least Mean Square
LO	Local Oscillator
LSNA	Large-Signal Network Analyser
LUT	Look-Up Table

MMIC	Monolithic Microwave Integrated Circuit
MTA	Microwave Transition Analyser.
NMSE	Normalised Mean Square Error
NVNA	Nonlinear Vector Network Analyser
NI	National Instrument
PA	Power Amplifier
PCIe	Peripheral Component Interconnect Express
PFI	Programmable Function Interface
PHD	Poly Harmonic Distortion Model
PNA-X	Phase Network Analyser-X Parameter
RF	Radio Frequency.
S-parameters	Scattering Parameters
T-Clk	Trigger Clock
VNA	Vector Network Analyser
VSA	Vector Signal Analyser
VSG	Vector Signal Generator

# TABLE OF CONTENTS

<b>Abstract .....</b>	<b>VI</b>
<b>List of publications.....</b>	<b>VIII</b>
<b>List of Abbreviation .....</b>	<b>IX</b>
<b>Table of Contents.....</b>	<b>XI</b>
<b>1 Introduction.....</b>	<b>1</b>
<b>1.1 Background.....</b>	<b>1</b>
<b>1.2 Device Modelling Branches .....</b>	<b>2</b>
1.2.1 Small-Signal Modelling .....	3
1.2.2 Large-Signal Modelling .....	3
<b>1.3 Measurements Strategies for Model Extraction .....</b>	<b>5</b>
<b>1.4 Thesis Objectives .....</b>	<b>7</b>
<b>1.5 Thesis Outline .....</b>	<b>8</b>
<b>References.....</b>	<b>11</b>
<b>2 LITERATURE REVIEW.....</b>	<b>13</b>
<b>2.1 Background.....</b>	<b>13</b>
<b>2.2 Linear Measurement Architecture .....</b>	<b>14</b>
<b>2.3 Non-Linear Measurement Architecture.....</b>	<b>16</b>
2.3.1 Development of Non-Linear Measurement Systems .....	17
<b>2.4 CW Load-Pull Measurement .....</b>	<b>21</b>
<b>2.5 Advancement in Load-Pull Systems .....</b>	<b>22</b>
2.5.1 Load-Pull Technique for Modulated Signal .....	25
2.5.2 Multi-tone Envelope Load-Pull Technique .....	26
2.5.3 Wideband Open-Loop Load-Pull Setup .....	29
<b>2.6 Load-Pull System Based on Pxie Modules .....</b>	<b>33</b>
<b>2.7 Chapter Summary .....</b>	<b>35</b>
<b>References.....</b>	<b>37</b>
<b>3 Direct Extraction of Complementary RF Design Information from Active Load-Pull Measurements.....</b>	<b>40</b>
<b>3.1 Introduction.....</b>	<b>40</b>
<b>3.2 System-Design Platform .....</b>	<b>41</b>
<b>3.3 Power Contour Measurements under Modulated Signal Excitation .....</b>	<b>48</b>
<b>3.4 Tickle-Tones Measurements in Active Load-Pull system .....</b>	<b>52</b>
<b>3.5 Tickle-Tone Verifications Under Large-Signal Input.....</b>	<b>54</b>

3.6	Stability Analysis.....	57
3.7	Chapter summary .....	65
	<b>References.....</b>	<b>67</b>
<b>4</b>	<b><i>Non-linear Behavioural Modelling.....</i></b>	<b>68</b>
4.1	Introduction.....	68
4.2	Polyharmonic Distortion (PHD) Model .....	69
4.2.1	PHD Model Formulation.....	69
4.3	X-Parameters.....	73
4.3.1	X-Parameters Measurement .....	74
4.3.2	Load-Dependent X-Parameters.....	75
4.4	Cardiff DWLUT Model .....	78
4.4.1	Extraction Cardiff DWLUT Model .....	78
4.5	Cardiff Behavioural Model.....	80
4.5.1	The General Formulation of the Cardiff Model.....	81
4.5.2	From CW to Two-Tone Stimulus .....	84
4.6	Chapter summary .....	93
	<b>References.....</b>	<b>95</b>
<b>5</b>	<b><i>Multi-tone Excitation for Model Extraction in Active Load-Pull .....</i></b>	<b>97</b>
5.1	Introduction.....	97
5.2	Model Identification for Two-Tone Stimulus (Phase Polynomial Only) .....	98
5.2.1	Behavioural Modelling with Magnitude and Phase Variation.....	113
5.3	Behavioural Model Extraction for Multi-Tone Stimulus .....	118
5.4	Model Identification for multi-tone stimulus .....	119
5.5	Mathematical Extraction of Cardiff Behavioural Model .....	125
5.5.1	Model Extraction.....	128
5.6	Experimental Verification.....	133
5.7	Chapter summary .....	139
	<b>References.....</b>	<b>142</b>
<b>6</b>	<b><i>Conclusion and Future Work .....</i></b>	<b>143</b>
6.1	Conclusion .....	143
6.2	Future Work .....	148
	<b>Appendix A.....</b>	<b>150</b>
	<b>Appendix B.....</b>	<b>159</b>

# CHAPTER 1

## INTRODUCTION

### 1.1 BACKGROUND

The power amplifier (PA) is considered the most significant part of wireless communication systems. It should be carefully designed in order to meet the exact requirement for different systems. Two of the most important figures of merits used to evaluate the quality of PAs are efficiency and linearity. Efficiency denotes how well the PA can convert a DC power into a required amount of RF power, which is suitable for transmission in such applications. Wireless communication has witnessed a flourishing revolution in the last few years. Nowadays, people use a mobile phone as a computer; it allows doing multi-tasking activity at the same time, which consumes more battery than a single task activity. Smartphones usually use the battery as the primary power source where poor efficiency performance means more power consumption and heat dissipation. As a result, shorter talk and standby time [1].

Linearity is considered the second figure of merit, which is used to measure how well the power amplifier can amplify the input signal without distortion. Linearity is vital for such a modulation scheme

---

that encodes information within the amplitude variation of the signal (for instance, Amplitude Modulation (AM) and Quadrature Amplitude Modulation (QAM)). On the other hand, modulation schemes depend on the capability of the receiver to discriminate the differences in the signal's amplitude, so "ideally" a PA must maintain the amplitude variation in the signal. This adds more burden to the receiver to recover the encoded information when the PA is compressed while transmitting the signal. In general, RF designers usually find a balance between linearity and efficiency. It is always impossible for both the linearity and efficiency to reach their maximums simultaneously.

## **1.2 DEVICE MODELLING BRANCHES**

In the last five decades, two main terms are used to describe all transistor modelling; small-signal modelling and large-signal modelling. Brief descriptions for both terms are presented in the following sections.

### **1.2.1 SMALL-SIGNAL MODELLING**

Small-signal models refer to the linear perturbation of the device (small-signal excitation) in comparison to the large-signal stimuli. Such models are useful for computation of design parameters, i.e. the gain and the device stability, using measurement data directly integrated into a Computer Aided Design (CAD) environment [2]. S-parameters (Scattering parameters) are typically utilised to quantify the linear operation of networks at radio frequency (RF) and microwave frequencies. Nevertheless, as power level increases, transistor devices start to exhibit nonlinear behaviour. Therefore, S-parameters are considered insufficient for design purpose under the large signal regime.

### **1.2.2 LARGE-SIGNAL MODELLING**

Large signal models are used to predict the performance of the device under non-linear operation. They can be subdivided into two main branches: Physical models, and Behavioural models.

#### **1.2.2.1 PHYSICAL BASED MODELS**

Comprehensive analysis on semiconductor physics is required to provide such a model. In general, there are two approaches to formulating such a model. The first approach is where the major

---

device physics is utilised as a source for the equations, which describe the terminal behaviour of the transistor, for instance, the thickness of the active semiconductor layer, layer doping, gate oxide thickness, etc. Major simplifications are required to the underlying physics of the device operation, to build up a model, which can then run fast enough in simulation to be used in circuit design. As mentioned earlier, this model was formulated based on physical equations. No electrical characterization is required to obtain a model. More discussion of such models is beyond the scope of this thesis, which can be found in [\[5, 6\]](#).

The second approach is to utilize a lumped equivalent electronic circuit, whose parameters are DC bias dependent to represent the physical behaviour of the device. Having an accurate model depends on the selected equivalent circuit topology and the analytical functions used to describe their DC bias dependence. Usually, some parts of the device physical operation are considered while others are neglected to keep the complexity at an acceptable level, with regards to the application of interest. These are often referred to as compact models.

### **1.2.2.2 BEHAVIOURAL MODELS**

The behavioural model is a black-box model, which does not need to be linked directly to the fundamental physics and/or internal circuitry, as a consequence it provides complete protection of Intellectual Property (IP). It is a mathematical description that relates the responses of the device to the input perturbations [7, 8]. It can be generated by linear measurement, non-linear measurement or by circuit simulation. Behavioural models can be commonly understood as a form of multidimensional curve fitting.

The behavioural model requires a minimum time to be generated; this means it can be used to quickly characterise an emerging device technology or process for PA design. Furthermore, model extraction is relatively easy compared to physical or compact models. The main applications of behavioural models being utilised in the industry are the Keysight X-parameters [9] [10], the Cardiff Model [11, 12], Volterra Input Output Map (VIOMAP) [13, 14], and S-parameters [15].

## **1.3 MEASUREMENTS STRATEGIES FOR MODEL EXTRACTION**

There are several measurement techniques that have been utilised to collect the required data for device model extraction. These measurements can be grouped into electrical and thermal measurements (thermal measurements are out of the scope of this

---

thesis). The electrical measurements can be categorized into three main branches: DC; small signal; and large-signal measurements.

DC measurements of the transistor produce the static DC-IV current-voltage relationships and can be done under either pulsed or continuous excitations [16]. S-parameter measurements are then often used to extract the dynamic behaviour of the device under test (DUT).

Small-signal RF measurements, S-parameters, can be achieved using Vector Network Analysers (VNAs), and these measurements are valid when the transistor operates in a linear condition where the superposition principle holds. It provides a linear description of its equivalent circuit behaviour.

Large-signal RF measurements are performed on a device where the superposition theorem is no longer applicable [17]. This allows capturing harmonic components, with their phase relationship. This is essential to define a complete picture of the device non-linear behaviour [18] when it is driven into a compression. Therefore, Nonlinear Vector Network Analyser (NVNA) is used for such kind of measurements [19], as it can provide insight into the time-domain voltage and current waveforms.

---

Large-signal measurements are usually performed in non 50 Ohm impedance area, such measurements are called load-pull measurements. Load-pull measurements are realised with impedances created passively or actively to generate data for the development of nonlinear transistor models such as measurement-based models [20] or polynomial-based models [21].

## **1.4 THESIS OBJECTIVES**

The main objectives of this work are listed as follow:

- To develop a load-pull measurement system operating under a multi-tone stimulus.
  - To utilize this system to provide complementary RF design information during active load-pull measurements using a two-tone, 'tickle-tone,' stimulus.
  - Utilising two-tone injection in the active load-pull system for direct identification of phase polynomial coefficients of the Cardiff model.
  - Exploiting multi-tone injection with Fast Fourier Transform (FFT) for direct extraction of phase and magnitude polynomial coefficients of the Cardiff model in the active load-pull system.
-

## **1.5 THESIS OUTLINE**

This section summarises the thesis's contents chapter-by-chapter as follows.

In chapter 2, a literature review of development the RF-measurement techniques is presented, beginning with using the VNA for small-signal measurements and showing the downside of using such a system to capture the non-linear effects under the large-signal stimulus. Subsequently, improving the functionality of the measurement systems was succeeded to introduce the NVNA for the large signal measurement. Furthermore, presenting the main contribution with some attempts to handle the advancements and evolution of the load-pull system to characterise the transistor under realistic condition, such as multi-tone or modulated signals. Finally, a brief description of the PXIe modules-based measurement system is introduced in this chapter.

Chapter 3 starts with describing the experimental verification to generate and receive multi-tone signals. It shows the significant challenges to achieve a high level of synchronisation between the two chassis and within the same chassis as well. Having said this, new measurements show the discrepancy in maximum load between CW and modulated signal using load-pull contours, which were tackled

---

afterwards. Later, this chapter shows the usefulness of exploiting two tickle-tones to extract useful data for RF designers during active load-pull measurements.

Chapter 4 is an overview of non-linear behavioural model approaches starting with PHD model, which is considered the basis of the modelling and its limitation, followed by X-parameters with PNA-X solution to be utilised in load-dependent X-parameters measurements. This allows the X-parameters to cover a large area of the Smith Chart and not restricted to the area around 50 Ohm. Moreover, the Cardiff Model formulations are revisited, showing the advantages of new techniques that utilise more than one tone with the FFT to move from the phase domain to the frequency domain for model identification and extraction.

Chapter 5 focuses on two approaches to be used for model identification of the Cardiff Behavioural Model; the first approach is implemented based on exploiting two-tone measurements, for the correct determination of Cardiff model phase coefficients, viewing the limitation of identifying both the magnitude and phase mixing terms. Consequently, a second approach is utilized with extra two-tones (AM-modulation) around the phase-modulated tone, which allows the observation of the magnitude and phasing mixing terms separately. Also, presenting the usefulness of exploiting the FFT in the Least Mean

---

Square (LMS) extraction process provides a very robust, direct extraction, solution for model coefficient determination.

Chapter 6 concludes the thesis work before proposing possible directions and interesting suggestions for future work in this domain.

---

## REFERENCES

1. Neuvo, Y. Cellular phones as embedded systems. in 2004 IEEE International Solid-State Circuits Conference (IEEE Cat. No.04CH37519). 2004.
  2. Gasseling, T., et al., Hot small-signal S-parameter measurements of power transistors operating under large-signal conditions in a load-pull environment for the study of nonlinear parametric interactions. IEEE Transactions on Microwave Theory and Techniques, 2004. **52**(3): p. 805-812.
  3. Gasseling, T., Compact transistor models: the roadmap to first-pass amplifier design success. Microwave Journal, 2012. **55**(3): p. 74-86.
  4. Camnitz, L.H., et al. An accurate, large signal, high frequency model for GaAs HBTs. in GaAs IC Symposium IEEE Gallium Arsenide Integrated Circuit Symposium. 18th Annual Technical Digest 1996. 1996.
  5. Tsividis, Y. and C. McAndrew, *Operation and Modeling of the MOS Transistor*. Vol. 2. 1999: Oxford university press Oxford.
  6. Filicori, F., G. Ghione, and C.U. Naldi, *Physics-based electron device modelling and computer-aided MMIC design*. IEEE Transactions on Microwave Theory and Techniques, 1992. **40**(7): p. 1333-1352.
  7. Schreurs, D., et al., *RF power amplifier behavioral modeling*. 2008: Cambridge University Press New York, NY, USA.
  8. Brazil, T.J. An overview of behavioral modeling for microwave power amplifiers. in 2009 IEEE 10th Annual Wireless and Microwave Technology Conference. 2009. IEEE.
  9. Root, D.E., et al., Broad-band poly-harmonic distortion (PHD) behavioral models from fast automated simulations and large-signal vectorial network measurements. IEEE Transactions on Microwave Theory and Techniques, 2005. **53**(11): p. 3656-3664.
  10. Root, D., *Polyharmonic distortion modeling*. IEEE microwave magazine, 2006. **7**(3): p. 44-57.
  11. Tasker, P.J. and J. Benedikt, *Waveform Inspired Models and the Harmonic Balance Emulator*. IEEE Microwave Magazine, 2011. **12**(2): p. 38-54.
  12. Woodington, S., et al. A novel measurement based method enabling rapid extraction of a RF waveform look-up table based behavioral model. in Microwave Symposium Digest, 2008 IEEE MTT-S International. 2008. IEEE.
-

13. Verbeyst, F. and V. Bossche, *VIOMAP, the S-parameter equivalent for weakly nonlinear RF and microwave devices*. IEEE Transactions on Microwave Theory and Techniques, 1994. **42**(12): p. 2531-2535.
14. Verbeyst, F. and M.V. Bossche, *The Volterra input-output map of a high-frequency amplifier as a practical alternative to load-pull measurements*. IEEE transactions on instrumentation and measurement, 1995. **44**(3): p. 662-665.
15. Myslinski, M., et al. S-functions behavioral model order reduction based on narrowband modulated large-signal network analyzer measurements. in 75th ARFTG Microwave Measurement Conference. 2010. IEEE.
16. Aaen, P., J.A. Plá, and J. Wood, *Modeling and Characterization of RF and Microwave Power FETs*. The Cambridge RF and Microwave Engineering Series. 2007, Cambridge: Cambridge University Press.
17. Cripps, S.C., *RF Power Amplifiers for Wireless Communications*. 2006: Artech House.
18. Roblin, P., *Nonlinear RF circuits and nonlinear vector network analyzers: interactive measurement and design techniques*. 2011: Cambridge University Press.
19. Benedikt, J., et al. High power time domain measurement system with active harmonic load-pull for high efficiency base station amplifier design. in 2000 IEEE MTT-S International Microwave Symposium Digest (Cat. No. 00CH37017). 2000. IEEE.
20. Qi, H., J. Benedikt, and P. Tasker. A Novel Approach for Effective Import of Nonlinear Device Characteristics into CAD for Large Signal Power Amplifier Design. in 2006 IEEE MTT-S International Microwave Symposium Digest. 2006.
21. Verspecht, J., et al. Extension of X-parameters to include long-term dynamic memory effects. in 2009 IEEE MTT-S International Microwave Symposium Digest. 2009. IEEE.

## CHAPTER 2

### LITERATURE REVIEW

#### 2.1 BACKGROUND

The continuous wave (CW) signals are often still being used in the majority of characterization systems. However, in modern wireless networks used complex modulated signals, such as WCDMA (Wideband Code Division Multiple Access) and LTE (Long-Term Evolution) together with the evolution of Computer Aided Design (CAD) software such as ADS (Advanced Design System) which can perform under such simulations; reliance on CW measurements is considered insufficient. Measurement systems having more complicated modulation, a more realistic input stimulus is becoming essential. In addition, there is a need for high-speed measurement systems because of the high density data necessary for better accuracy. A potential solution for this point is to also employ multi-tone or modulated signal measurements, which can speed up the process by collecting more data whilst still covering a large area of Smith Chart.

The beginning of this chapter provides the reader with a brief description of the evolution of the measurement technology, starting from linear measurements and transitioning to non-linear

---

measurements to include characterisation of the DUT at different load conditions, which is called load-pull measurement. After that, the advancement of the measurement systems for multi-tone applications will be introduced, ending with a brief description about the current measurement system based on PXI (PCI extensions for Instrumentation) modules, which will ultimately be used in all experiments in this thesis.

## 2.2 LINEAR MEASUREMENT ARCHITECTURE

To describe the behaviour of electrical networks under small signal stimuli, S-parameters are utilised to measure the relationship between the incident and reflected travelling waves at the input and output of a device. Travelling waves are introduced as follows:

$$a_i = \frac{V_i + Z_i I_i}{2 \sqrt{\text{Re}(Z_i)}} \quad b_i = \frac{V_i - Z_i^* I_i}{2 \sqrt{\text{Re}(Z_i)}} \quad (2-1)$$

Where 'i' indicates the port index, (\*) indicates the conjugate, and  $\text{Re}(Z_i)$  indicates the real component of the complex impedance  $Z_i$ . S-parameters were revived in the 1960s by Kurokawa's paper [1] that provided a comprehensive description of the circuit network and considered one of the most significant approaches used for transistor characterisation [2]. S-parameters are primarily used when the wavelength of the signal is proportional or much smaller than the dimension of the circuit components [3].

The Vector Network Analyser (VNA) is a form of Network Analyser broadly utilised in RF design applications. It is used to measure the S-parameters, the resultant magnitude and phase of these S-parameters can be displayed in different formats according to the user's application. This information allows the RF designers to have such complementary information about the design parameters such as gain, stability, and reflection coefficient. S-parameters are used for describing the behaviour of a Device Under Test (DUT) under linear (small-signal) conditions.

The generic configuration of the VNA (see Figure 2-1) is comprised of three main parts: RF generators to be used for generating the signal to the DUT, receivers to measure the incident and reflected waves, and a test set to separate the incident and reflected waves.

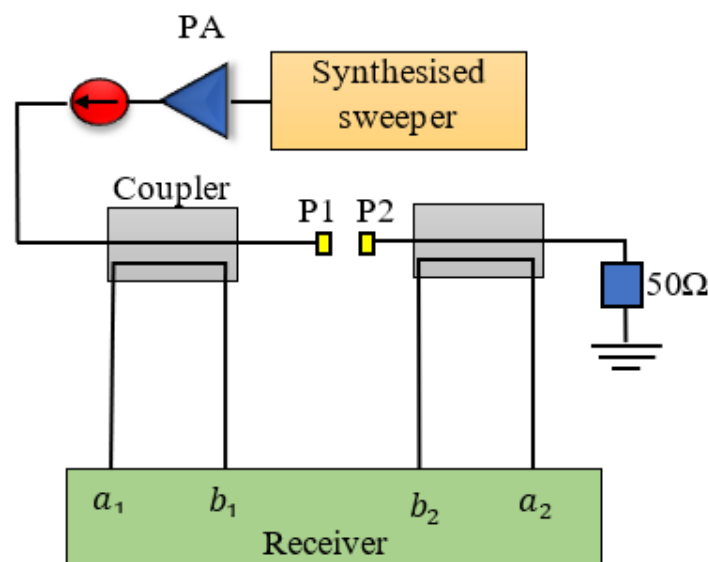


Figure 2-1: Forward measurements for 2-port VNA measurement

Figure 2-1 shows the forward measurement to measure  $S_{11}$  and  $S_{21}$ . This is done by terminating port 2 with 50 Ohm to avoid any reflection ( $a_2 = 0$ ) back to port 1. The same scenario is repeated for reverse measurements to measure  $S_{22}$  and  $S_{12}$ . This time port 1 is terminated with 50 Ohm ( $a_1 = 0$ ) using the following formulas:

$$S_{11} = \left. \frac{b_1}{a_1} \right|_{a_2=0} \quad S_{21} = \left. \frac{b_2}{a_1} \right|_{a_2=0} \quad (2-2)$$

$$S_{22} = \left. \frac{b_2}{a_2} \right|_{a_1=0} \quad S_{12} = \left. \frac{b_1}{a_2} \right|_{a_1=0} \quad (2-3)$$

However, the downside of using such a VNA architecture is that it is inadequate to analyse large-signal phenomena, such analysis imposes a dilemma because it does not account for the non-linear distortion effects such as compression, Amplitude Modulation–Phase Modulation (AM-PM), harmonic generation, and intermodulation distortion (IMD). In particular, it is incapable of measuring the phase relationship between the signal's harmonics; hence, it is limited to linear measurements where no harmonics are presented at both ports of the DUT.

### **2.3 NON-LINEAR MEASUREMENT ARCHITECTURE**

In measurements when the DUT is driven with the large signal input, the objective is that the measurement system provides appropriate information to analyse the non-linear behaviour of the DUT.

Traditionally, researchers devoted their efforts to develop large-signal measurement systems to locate the optimum matching impedance (usually away from 50 Ohm) to provide the maximum output power and/or high efficiency. This type of measurement is called Load-pull [4]. Such information is very useful for RF designers, supports the development of device models necessary for Computer Aided Design (CAD) software, and finally, for model validation by comparing between the simulated and the fabricated device performance. For the reasons above, the next section will focus on the new generation of measurement systems to measure and characterise the DUT under the large signal stimulus.

### **2.3.1 DEVELOPMENT OF NON-LINEAR MEASUREMENT SYSTEMS**

The evolution of large signal measurement started in 1988 when Sipila et al. [5] introduced their paper on the first system that had the capability to measure in the time domain and convert the data to the frequency domain, using the Fast Fourier Transform (FFT), for error correction and then convert the data back into the time domain. Figure 2-2 shows the two-channel 14 GHz oscilloscope that was used to measure only two travelling waves (the reflected input wave  $b_1$ , and transmitted output waveform  $b_2$ ) from the overall four waves.

---

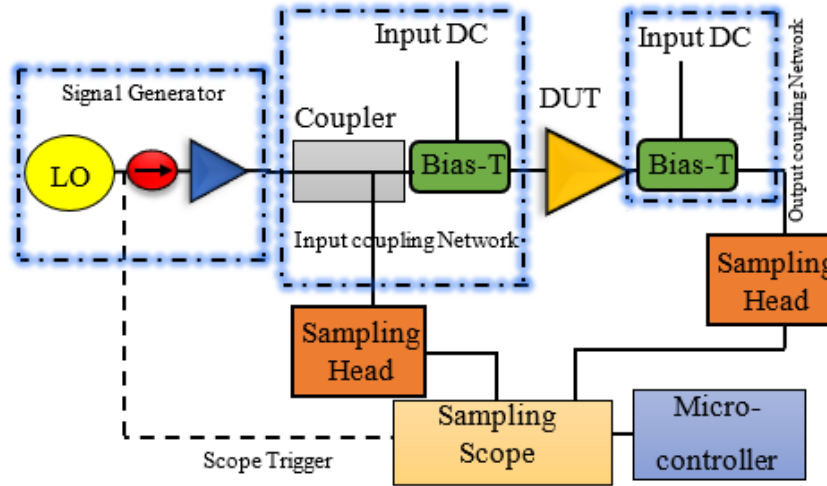


Figure 2-2: Block diagram of the presented work by Sipila [5].

The main downside of the above work is the capability of only measuring two travelling waves at the same time. This increases the possibility of having an error during S-parameters measurements of the input and output port of the coupler. In addition, the dynamic range was reduced as the noise presented by the trigger jitter in comparison with the mixer-based approach utilised in VNAs.

An alternative method was made by Lott in 1989 [6] to capture the waveform information based on VNA architecture. A signal generator was used to stimulate the DUT; the architecture is realized by a tunable filter to separate the measurement of the main-tone and the harmonics. A phase reference approach was utilised to align the harmonics by a millimetre-wave Schottky diode or so-called a golden diode technique. Nevertheless, the limitation of this technique was the inaccurate phase reference measurement because of uncertainty in the phase between measured harmonics.

Kompa and Van Raay described an analogous system in 1990 that combines a two-channel microwave oscilloscope with a VNA [7]. The receiver and the oscilloscope were used to measure the fundamental data, and the harmonics respectively. This combines frequency domain analysis with a high dynamic range of the VNA with the ability to detect time domain waveforms from a sampling oscilloscope. It is worth noting that, the measurement system was limited to characterise the DUT under single tone stimulus.

A revolution started in 1992 with the Microwave Transition Analyser (MTA) from Hewlett-Packard. It had a dual channel receiver and could directly measure the phase and the amplitude of fundamental and harmonic spectral components over a 40 GHz bandwidth. It was first presented by Kompa and Van Raay [8], the measurement setup was less complicated because no trigger circuitry was presented in comparison with the sampling oscilloscope.

The MTA can be used as a VNA to measure magnitudes and phases of the fundamental and harmonic signals; hence, it allows for the measurement of waveforms. Further improvement to the system ability was made in Cardiff University [9] by adding switching and multiplexing network to the architecture, efficiently turning the two channels into four channels MTA receiver as shown in Figure 2-3. This allows collecting the four travelling wave measurements

---

synchronously by using three measurement cycles; the first measurement was used to measure the incident and reflect waves of port 1 ( $a_1$  and  $b_1$ ), the next measurement was employed to calculate the phase difference between  $a_1$  and  $b_2$ , and the final measurement was utilised to measure output incident and reflected wave ( $a_2$  and  $b_2$ ) at port 2.

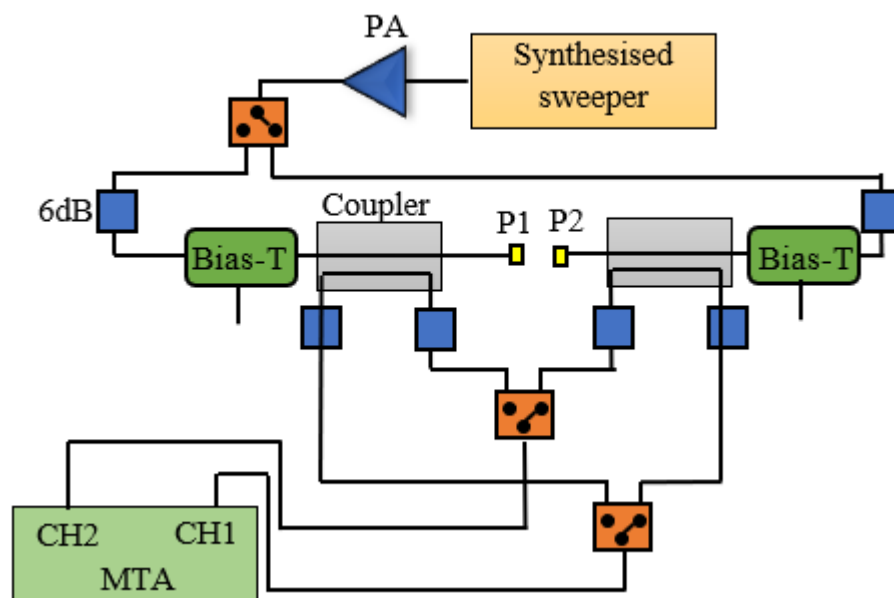


Figure 2-3: Generic block diagram of the measurement system based on the MTA.

An alternative approach was taken by Verspecht et al. [10] which used two synchronised MTAs to form a new four-channel measurement instrument. This modified MTA was used as the foundation of a large signal measurement architecture known as the Non-Linear Vector Network Analyser (NVNA). Such a waveform measurement system is considered a useful tool for accurate non-linear CAD models [11].

---

Gharaibeh et al. in [12] noted that the traditional CW or a simple two-tone measurement is insufficient for the accurate estimation of in-band distortion. Hence, it is required to uncover the effect of distortion when the DUT is driven by a multi-tone stimulus.

## 2.4 CW LOAD-PULL MEASUREMENT

Nowadays, the significant challenge in the design of mobile communication base stations is to understand the high-efficiency power amplifiers (PAs). Designing these PAs needs the realisation of the effect of output load impedance variations on PA parameters, such as output power  $P_{out}$ , efficiency, and intermodulation distortion (IMD).

Load-pull measurements are commonly used in PA design as the potential for direct measurement of the DUT under realistic operating conditions. Source-pull and load-pull for a given biasing condition, allow the performance of the DUT to be optimized to meet the desired performances such as linearity, and Power-Added Efficiency (PAE) of the DUT [13]. Such techniques are employed in RF applications under large-signal input to locate the optimum complex load impedance of the device (far from 50 Ohm) to identify the required well-known parameters; such as output power, gain and efficiency as a function of load impedance. However, the use of CW large signal measurements; in the design of PA's for communication systems using advanced

modulation schemes is limited. Hence, the success of mobile communications has been increasingly encouraging measurement instrumentation companies to develop systems to accommodate more complex user requirements. Such a system needs to be fast, accurate and adequate for multi-tone or modulate signal measurements. For example, new load-pull systems were introduced in [14-18] that are capable to locate the desired complex load and to characterise the device for specific applications more robustly.

## **2.5 ADVANCEMENT IN LOAD-PULL SYSTEMS**

As previously stated, the researchers developing measurement systems have tried to address the significant challenge of coping with the advances and complexity in mobile networks. Therefore, in literature, many load-pull measurement systems have been introduced to provide the requirement to the end users. It has been very common to examine the nonlinearity under two-tone signals because it is theoretically straightforward to realise. Undoubtedly, numerous essential concepts about nonlinear circuit response, for instance, intermodulation distortion, memory effects [19] and gain compression/expansion, were clarified by using a two-tone stimulus. To demonstrate the nonlinear behaviour using multi-tone stimulus, it is imperative to observe the IMD products under a two-tone stimulus,

---

as demonstrated in [20]. Nevertheless, the work on the multi-tone stimulus is still an active area of research.

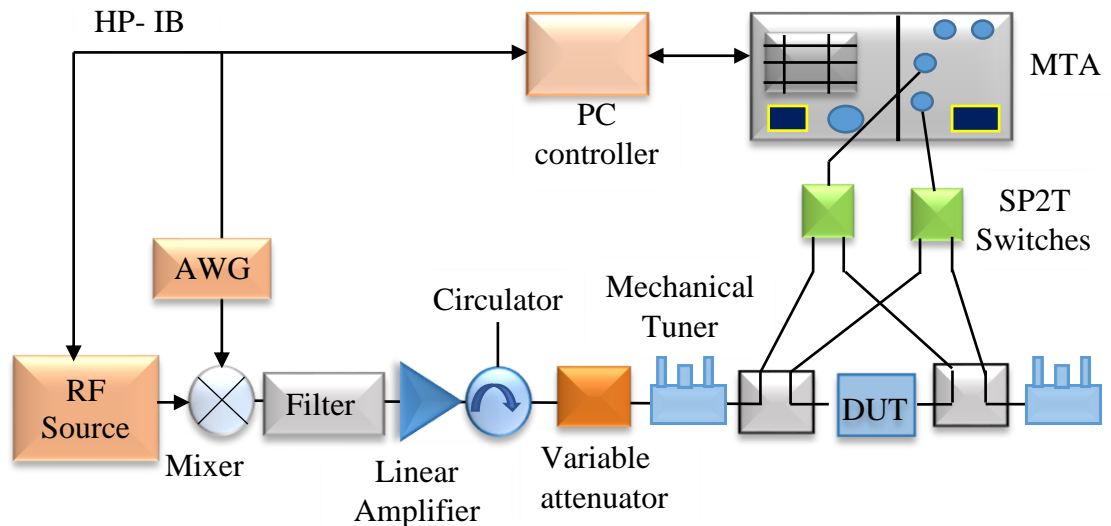


Figure 2-4: Block diagram of the multi-tone load-pull measurement system.

Ghannouchi et al. in [14, 21] have introduced their work on developing a multi-tone signal set up to examine the linearity of the power amplifier (PA) through the IMD products. Figure 2-4 shows the setup for the characterisation of the IMD products with multi-tone phase distribution.

The system presented above uses Arbitrary Waveform Generator (AWG (HP8770A)) to generate a multi-tone with the arbitrary frequency spacing, power level and phase. This helps by reducing the complexity of the system and achieves a better synchronisation between the generated tones. In addition, the microwave transition analyser (MTA (HP70820)) acts as a network analyser to read the incident and

reflected waves via switches. A mixer was used to up-convert the generated signal from the baseband to the RF operating while the variable attenuator achieves the power sweep from the generated signal. The filter attenuates the output of intermodulation rejection (IMR) at 55 dBc. To guarantee a high power level, a linear PA was installed after the selected tones from a narrowband filter. The mechanical tuner adjusts the input reflection coefficient to the transistor while the output tuner is used to passively tune the load. It is worth mentioning that this system can be adequate for both packaged and on-wafer devices.

The setup above was useful to characterise the linearity of the DUT based upon two parameters, the phase distribution and biasing condition. It was shown that the IMR is heavily dependent on the above two parameters, specifically with an increasing number of tones. However, the downside of this system is that passive load-pull still cannot fully cover the whole impedance range of the Smith Chart, due to the inherent losses within the tuners.

### **2.5.1 LOAD-PULL TECHNIQUE FOR MODULATED SIGNAL**

To optimise third-order intermodulation products (IMD3), the load-pull measurements have been commonly used for two-tone stimulus. With the advancement of complex digital modulation techniques, the prediction of the performance of the device under these simple stimuli is questionable. The work in [22, 23] has found that the performance of the DUT is undoubtedly dependent on the type of injected signal applied throughout the measurement. In order to examine the performance of the device under digitally modulated signals, Ghanipour et al. have developed a load-pull setup as shown in Figure 2-5 [15].

The results were obtained on the automated load-pull system and compared with gain and IMD3 under the two-tone stimulus. In the following setup, an Automatic Tuner System (ATS) from Maury Microwave was utilised. A Rohde and Schwarz (SMIQ03B) were deployed to upload and generate the desired modulated signal whereas the Adjacent Channel Power Ratio (ACPR) and IMD3 of the signals were measured using an FSQ8 Vector signal analyser. A Travelling Wave Tube Amplifier (TWTA) amplifies the injected signal, and the power meter (HP437B) measured the output and reflected the power of the device.

---

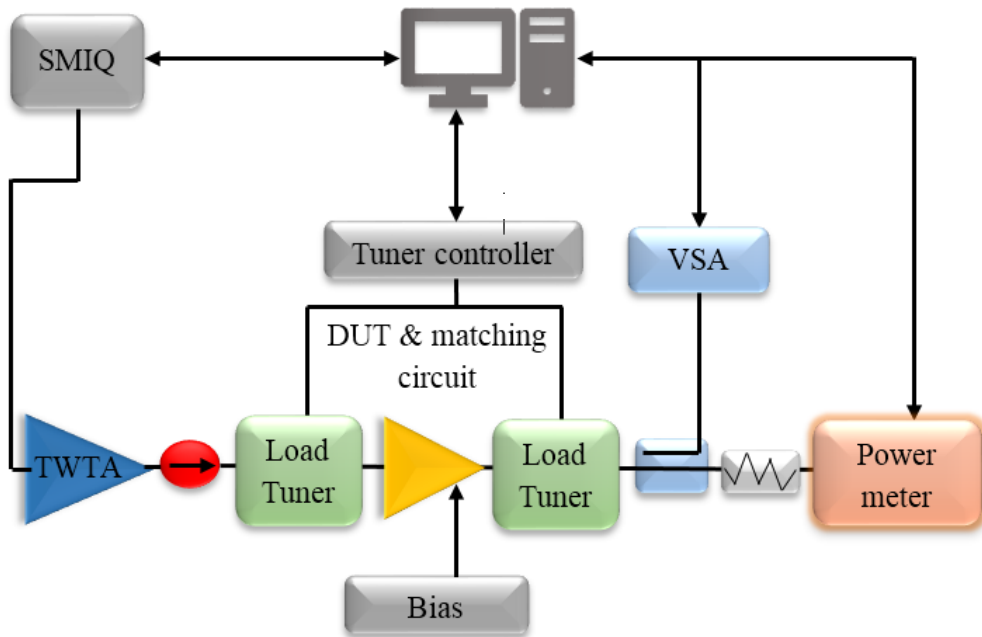


Figure 2-5: Load-pull setup for the modulated input signal.

Results showed that the device behaviour depends on the input stimuli's power and the bandwidth whilst being independent of the type of injected signal such as a wideband code division multiple access (WCDMA) or Orthogonal Frequency Division Multiplexing (OFDM). Furthermore, the size and shape of the contours are quite dependent on the type of the injected signal throughout the measurement.

## 2.5.2 MULTITONE ENVELOPE LOAD-PULL TECHNIQUE

The appropriate approach to characterise the behaviour of the PA is to utilise a large-signal measurement system to accommodate these

complex modulation schemes. This allows for compatibility with modern mobile communication techniques. A load-pull system was developed by Hashmi et al. termed envelope load-pull (ELP) was proposed for multi-tone stimulus [24]. Such a load-pull system is able to synthesize a constant impedance over a modulation bandwidth, the gamma load was controlled by a feedback loop at baseband (modulation) frequency as shown in Figure 2-6.

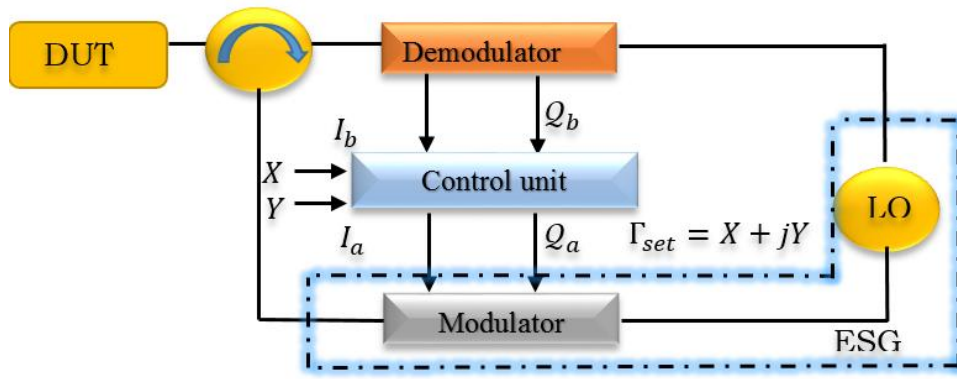


Figure 2-6: Envelope load-pull setup.

Equation (2-4) represents the emulated reflection coefficient:

$$\Gamma_{Load}(\omega) = \frac{a_2(\omega)}{b_2(\omega)} = X + jY \quad (2-4)$$

$$\Gamma_{Load}(\omega_c - n\omega_m) = \frac{a_2(\omega)}{b_2(\omega)} = (X + jY)e^{jn\omega_m\tau} \quad (2-5)$$

A new form of the equation in (2-5) is shown where  $\omega_m$ , a modulated signal with  $n$ , represents the number of tones. A problem was identified in eq.(2-5) related with the group delay where the emulated reflection coefficient is dependent on the phase operator,  $e^{jn\omega_m\tau}$ , of the

modulation frequency. This causes a phase spread between the synthesized reflection coefficients.

It should be mentioned that the above setup uses analogue control electronics in the baseband feedback, which imposes a dilemma as it only works for a narrow bandwidth usually less than 1 kHz. Later, this limitation was solved when Hashmi et al. in [25] integrated a digital control loop on a reconfigurable field-programmable gate array (FPGA). Such a system is capable of tracking the time-varying amplitude and phase envelope of modulated signals in the feedback loop. Hence, the capability of synchronising the incident and reflected waves over a bandwidth of more than 5 MHz.

The same group of researchers Hashmi et al. [18, 26] were able to propose a technique to tackle the group delay issue. Total delay was increased so that it was equal to the envelope repetition rate. The delay compensation is thus depending upon variously applied tone spacing as depicted in Figure 2-7.

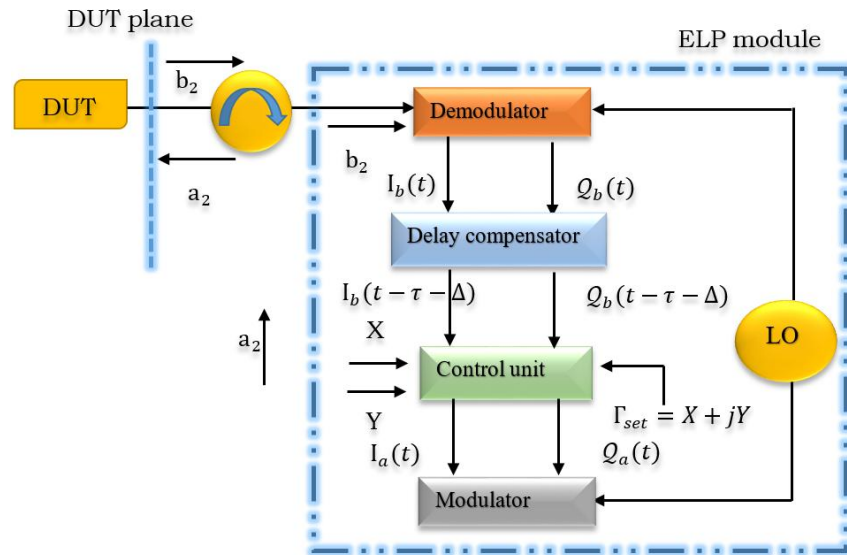


Figure 2-7: Envelope load-pull setup with a delay compensator.

### 2.5.3 WIDEBAND OPEN-LOOP LOAD-PULL SETUP

The commercial passive load-pull systems are unable to cover the complete Smith Chart as they are constrained by losses and electrical delay in the tuners. Conversely, most of the active load-pull systems can cover the whole Smith Chart, but are unsuitable for linearity characterisation with wideband signals, because of the inherent electrical delay related with these systems that cause a spread in the phase of synthesized reflection coefficients. Minimising electrical delay in the active loads guarantees a constant load condition against frequency to all frequency components. Therefore, Spirito et al. [27] developed an active load-pull setup which was then further enhanced by Marchetti et al. in [28].

---

When stimulating the DUT by a modulated signal, non-linear behaviour produces an output waveform that contains the fundamental frequency, BB, harmonics and IMD products as shown in Figure 2-8. To control the impedance across the applied modulated bandwidth to the DUT, a linear relationship between the incident and reflected waves generated by the device should be established against frequency as clarified in(2-6) [28].

$$a_{x,n}(f_n) = b_{x,n}(f_n) \cdot \Gamma_{x,n}(f_n) \quad (2-6)$$

Figure 2-8 is a basic description of the wideband approach. The signal  $a_{p,h}$  is the injected modulated signal, the output signals at  $b_{1,h}$  and  $b_{2,h}$  are generated by the device. The subscripts p and h are the port number and the harmonic index respectively. By monitoring the incident and reflected waves, the desired input signal  $a_{2,h}$ , targeting a designed load impedance can be determined by consecutive iterations.

The injected wave can be optimized by observing the variation of the measured reflection coefficient with the target one at each frequency. Another point worthy of mentioning is that this technique needs the wideband, high dynamic range to measure the reflection coefficients at each spectral component of the modulated signals. Additionally, the dynamic range should be high when an a-wave is injected, and the system should be phase coherent for all the waves and at each port in both RF and baseband frequencies.

---

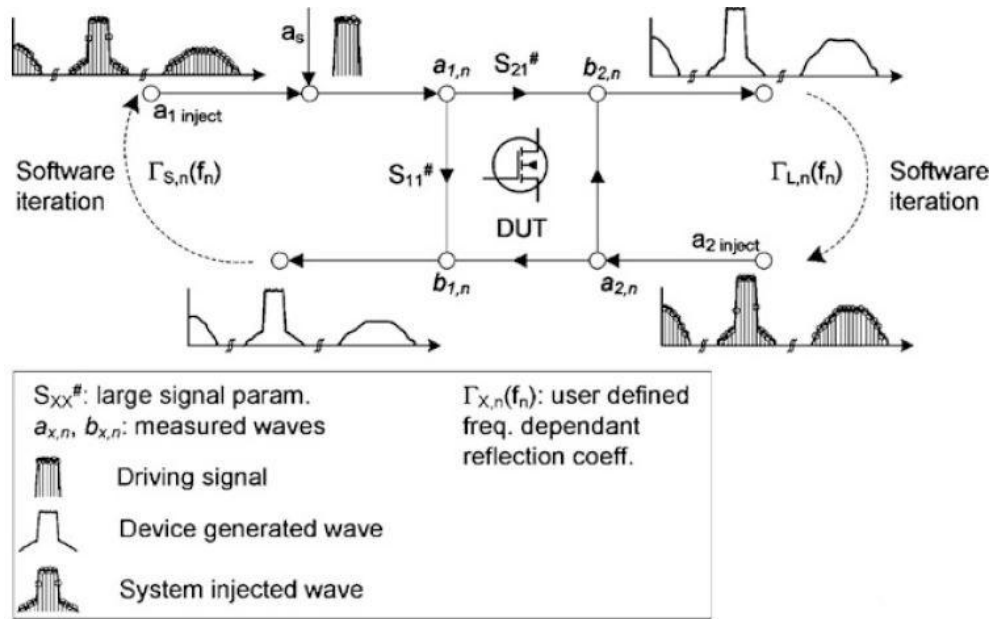


Figure 2-8: Proposed wideband, open-loop active load-pull method by Marchetti [28].

Figure 2-9 shows a complete setup from Antevta where the measurements are performed. Arbitrary waveform generators (400 MS/s) are used to generate the desired waveform at both ports after being up-converted using in-phase/quadrature (IQ) modulators. From the receiver side, the Incident and reflected waves from the device are down-converted to an intermediate frequency (IF) by the high linear mixer to be ready for digitising by the 100MS/s sampling frequency analogue to digital converter (ADC) with an analogue bandwidth of about 40 MHz. The AWGs and ADC are placed in the same PXI chassis so that they are synchronised and share the same time base.

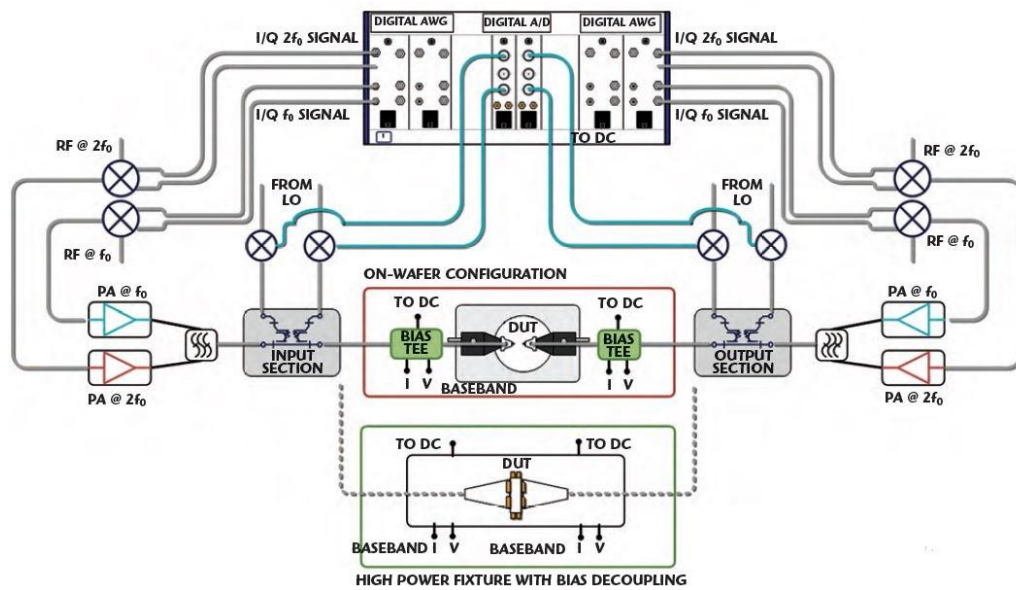


Figure 2-9: Block diagram of the mixed-signal active open-loop load-pull setup [28].

Furthermore, the generating and acquiring the data are done through PXI-based A/D and D/A instrumentation, hence, removing the need for mechanical tuners or VNA; ultimately reduce the cost. Bias-Tees are placed directly at the device reference planes, yielding electrical delay reduction of the baseband impedance. Please note that in the extended version, an additional AWG can be added to control the active baseband impedance.

## 2.6 LOAD-PULL SYSTEM BASED ON PXIE MODULES

PXI is a PC-based platform [29]. PXI systems consist of three basic components; chassis, controller, and peripheral modules. There is a growing demand to increase the measurement speed and to develop the performance of RF instruments. For these reasons, PXI and PXIe are considered a solution for the next RF generation and microwave test systems.

Al-Husseini in his doctoral thesis [30] developed a measurement system based on PXIe modules, similar to previously published non-linear measurement systems that are based on a Vector Network Analyser (VNA) [31, 32]. It is important to explain in brief this measurement system as it is the hardware used in this research thesis.

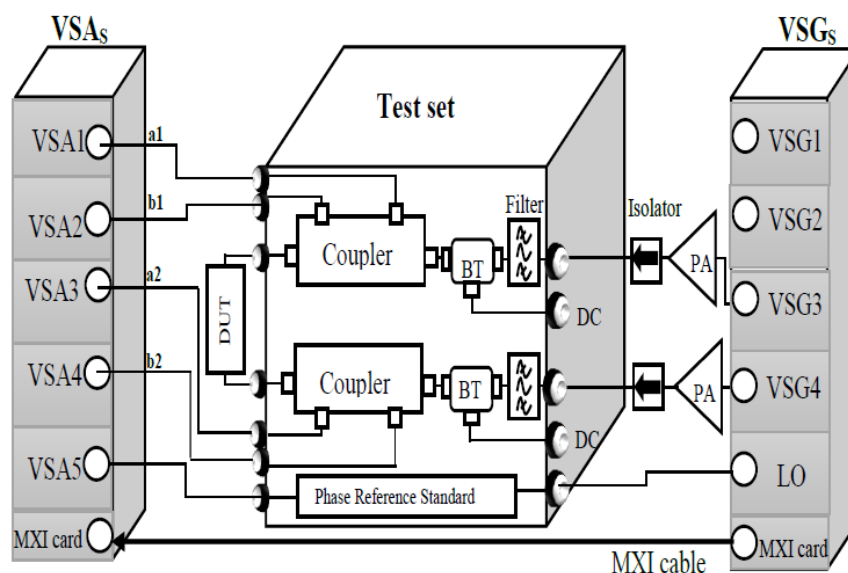


Figure 2-10: Block diagram of the measurement system.

---

Figure 2-10 depicts the block diagram showing the composition of the active load-pull measurement system that was used for the measurement and analysis described in this thesis. Two chassis were used as shown above. The first chassis consists of five generators by National Instruments (NI) vector signal generators (VSGs) NI PXIe-5673E, four VSGs with one to provide the fundamental input signal while the other three are for the fundamental and harmonic signals at the output of the DUT. Another PXI chassis contains five receivers. Vector signal analysers (VSAs) “NI PXIe-5663E” are used with the first four receivers to acquire the four incident and reflected waves at the DUT terminals. The fifth receiver monitors the harmonic spectrum of the phase reference standard. It is worth noting that both generators VSG1 and VSG2 in Figure 2-10 are utilised for second and third harmonics, which are out of the scope of this thesis as the main contribution focuses on the fundamental frequency only.

Driver PAs can be inserted to amplify the VSG signals to appropriate levels for our measurements. A test-set consisting of directional couplers and multiplexing filters [33] is used for the detection of the incident and reflected waveforms and separate the output harmonics, respectively. All VSAs and VSGs in this system have an instantaneous bandwidth of 50 MHz. I/Q generation and signal acquisition within the 50 MHz bandwidth can be performed without frequency switching or changing the frequency of the Local Oscillator (LO). The PXIs have

---

synchronised over 10 MHz clock signals. Software and hardware ensure triggering and sample-level alignment.

It is important to note that there is no physical device named “NI PXIe-5663E.” for VSAs, in fact, it consists of three main modules NI PXIe-5601RF downconverter module, NI PXIe-5622 IF digitizer module where the sampling rate of the analogue-to-digital converters (ADCs) is software controlled with a maximum of 150MS/s, and NI PXIe-5652 RF signal generator module (used as a LO source). Furthermore, three specific modules comprise the VSG: arbitrary waveform generator (AWG) module (NI PXIe 5450), I/Q modulator module (NI PXIe-5611), and local oscillator (LO) (NI-PXIe 5652).

The work presented in [\[30\]](#), demonstrated the capability in terms of speed, accuracy and dynamic range in such an active load-pull system. In this work, the hardware parts were used for applications focusing on CW measurements only. This work will extend its use to applications requiring multi-tone stimuli.

## **2.7 CHAPTER SUMMARY**

This chapter points out the development of the RF-measurement techniques, beginning with the small-signal measurement using the

---

---

VNA showing the limitation of using such a system to describe the non-linear effects under the large-signal stimulus. Later, the advancement and evolution of improving the functionality of the measurement system to introduce the NVNA for the large signal measurement, which was considered a breakthrough in terms of the calibration and the measurement techniques. The main restriction of the above systems was their limited ability to characterise the device under the realistic condition, such as wideband multi-tone modulated signals. Load-pull measurement techniques are considered an ideal solution for nonlinear measurements. It was highlighted that a vital contribution for further improvements would be to advance the execution speed, accuracy, and load-pull techniques. Later, this chapter introduced the new emerging multi-tone and modulated load-pull systems. Showing in literature the recent contribution to the evolution of such complex modulation systems. Ultimately, a brief description of the PXIe modules-based measurement system was presented, demonstrating its capability of performing high-speed and accurate CW RF measurements. A key observation is that such a system can enable multi-tone load-pull measurements. This thesis will focus on achieving this objective. This was done by developing LabVIEW software to enable accurate measurements and achieve a high level of synchronisation between the two chassis as detailed in the next chapter.

---

---

## REFERENCES

1. Kurokawa, K., *Power Waves and the Scattering Matrix*. IEEE Transactions on Microwave Theory and Techniques, 1965. **13**(2): p. 194-202.
2. Test, H.-P., Measurement Application Note 95-1, S-parameter techniques for faster, more accurate network design. 1997.
3. Matthews, E.W., *The Use of Scattering Matrices in Microwave Circuits*. IRE Transactions on Microwave Theory and Techniques, 1955. **3**(3): p. 21-26.
4. Aaen, P., J.A. Plá, and J. Wood, *Modeling and characterization of RF and microwave power FETs*. 2007: Cambridge University Press.
5. Sipila, M., K. Lehtinen, and V. Porra, *High-frequency periodic time-domain waveform measurement system*. IEEE Transactions on Microwave Theory and techniques, 1988. **36**(10): p. 1397-1405.
6. Lott, U., *Measurement of magnitude and phase of harmonics generated in nonlinear microwave two-ports*. IEEE Transactions on Microwave Theory and Techniques, 1989. **37**(10): p. 1506-1511.
7. Kompa, G. and F. Van Raay, Error-corrected large-signal waveform measurement system combining network analyzer and sampling oscilloscope capabilities. IEEE Transactions on Microwave Theory and techniques, 1990. **38**(4): p. 358-365.
8. van Raay, F. and G. Kompa. A new on-wafer large-signal waveform measurement system with 40 GHz harmonic bandwidth. in 1992 IEEE MTT-S Microwave Symposium Digest. 1992. IEEE.
9. Benedikt, J., Novel high frequency power amplifier design system. 2002.
10. Verspecht, J., et al. Accurate on wafer measurement of phase and amplitude of the spectral components of incident and scattered voltage waves at the signal ports of a nonlinear microwave device. in Proceedings of 1995 IEEE MTT-S International Microwave Symposium. 1995. IEEE.
11. Qi, H., J. Benedikt, and P.J. Tasker. Novel nonlinear model for rapid waveform-based extraction enabling accurate high power PA design. in 2007 IEEE/MTT-S International Microwave Symposium. 2007. IEEE.
12. Gharaibeh, K.M., K. Gard, and M.B. Steer. Characterization of in-band distortion in RF front-ends using multi-sine excitation. in 2006 IEEE Radio and Wireless Symposium. 2006. IEEE.

- 
13. Deshours, F., et al., *Experimental comparison of load-pull measurement systems for nonlinear power transistor characterization*. IEEE transactions on instrumentation and measurement, 1997. **46**(6): p. 1251-1255.
  14. Hajji, R., F. Beanregard, and F.M. Ghannouchi, *Multi-tone power and intermodulation load-pull characterization of microwave transistors suitable for linear SSPA's design*. IEEE Transactions on Microwave Theory and Techniques, 1997. **45**(7): p. 1093-1099.
  15. Ghanipour, P., S. Stapleton, and J. Kim, *Load&ndash;Pull Characterization Using Different Digitally Modulated Stimuli*. IEEE Microwave and Wireless Components Letters, 2007. **17**(5): p. 400-402.
  16. Di-Luan, L. and F.M. Ghannouchi, *Multi-tone characterization and design of FET resistive mixers based on combined active source-pull/load-pull techniques*. IEEE Transactions on Microwave Theory and Techniques, 1998. **46**(9): p. 1201-1208.
  17. Noori, B., et al., *Load-Pull Measurements Using Modulated Signals*. 2006. 1594-1597.
  18. Hashmi, M.S., et al. *Active envelope load pull system suitable for high modulation rate multi-tone applications*. in 2008 Workshop on Integrated Nonlinear Microwave and Millimetre-Wave Circuits. 2008.
  19. Carvalho, N.B., et al., *Multisine signals for wireless system test and design [Application Notes]*. IEEE Microwave Magazine, 2008. **9**(3): p. 122-138.
  20. H. Jacobi, J., *IMD: STILL UNCLEAR AFTER 20 YEARS*. Vol. 25. 1986. 119-120, 122.
  21. Hajji, R., F. Beauregard, and F.M. Ghannouchi. *Multi-tone transistor characterization for intermodulation and distortion analysis*. in 1996 IEEE MTT-S International Microwave Symposium Digest. 1996.
  22. Sevic, J.F., et al. *Automated Large-Signal Load-Pull Characterization of Adjacent-Channel Power Ratio for Digital Wireless Communication Systems*. in 46th ARFTG Conference Digest. 1995.
  23. Clark, C.J., et al., *Time-domain envelope measurement technique with application to wideband power amplifier modeling*. IEEE Transactions on Microwave Theory and Techniques, 1998. **46**(12): p. 2531-2540.
  24. Williams, T., J. Benedikt, and P.J. Tasker. *Experimental evaluation of an active envelope load pull architecture for high speed device*
-

- 
- characterization. in IEEE MTT-S International Microwave Symposium Digest, 2005. 2005.
25. Hashim, S.J., et al. Active Envelope Load-Pull for Wideband Multi-tone Stimulus Incorporating Delay Compensation. in 2008 38th European Microwave Conference. 2008.
  26. Arthaber, H., M.L. Mayer, and G. Magerl, *An active load-pull setup for broadband signals using digital baseband processing for the active loop*. International Journal of RF and Microwave Computer-Aided Engineering, 2008. **18**(6): p. 574-581.
  27. Spirito, M., et al., *Active Harmonic Load&ndash;Pull for On-Wafer Out-of-Band Device Linearity Optimization*. IEEE Transactions on Microwave Theory and Techniques, 2006. **54**(12): p. 4225-4236.
  28. Marchetti, M., Mixed-signal active load Pull: the Fast track to 3g and 4g aMPLiFiers. Microwave Journal, 2010. **53**(9): p. 108-+.
  29. *PXI Systems*. Available from: <http://www.ni.com/en-gb/shop/pxi.html>.
  30. Hussein, T., On the development and automation of a high-speed load-pull system based on Pxie modules, in School of Engineering. 2018, Cardiff University.
  31. Kapetanic, P., J. Martens, and D. Rangel, *Vector network measurement system*. 2003, Google Patents.
  32. Roblin, P., *Nonlinear RF circuits and nonlinear vector network analyzers: interactive measurement and design techniques*. 2011: Cambridge University Press.
  33. Alghanim, A., J. Benedikt, and P. Tasker. A measurement test-set for characterisation of high power LDMOS transistors including memory effects. in High Frequency Postgraduate Student Colloquium, 2005. 2005. IEEE.
-

## **CHAPTER 3**

### **DIRECT EXTRACTION OF COMPLEMENTARY**

### **RF DESIGN INFORMATION FROM ACTIVE**

### **LOAD-PULL MEASUREMENTS**

#### **3.1 INTRODUCTION**

**I**t is important to have a flexible and accurate high-speed RF measurement system with software-designed, modular instruments that can be potentially developed for user-defined RF measurements. Such a system would ensure that a large amount of data could be collected from a transistor within a significantly reduced time-frame. For instance, the capability of quickly extracting a reliable global behavioural model of a DUT helps to reduce the effort and time required for the users. This can be realized by utilising a new generation of software-designed and modular PXIe modules, which can be used to develop a customisable and reconfigurable system with precise measurements and importantly reduced space, to cope with the fast evolution of the wireless industry.

The previous work in [1] presents a novel high-speed RF measurement system (see Figure 2-10) that is based on commercially available PXIe modules for CW measurements. This chapter first demonstrates the software developments necessary to extend the work to include both the CW and multi-tone measurements. The remaining part of the chapter will be dedicated to utilizing the developed system to do novel measurements aimed at examining the stability condition under large signal operation. The multi-tone capability of the system will be used to measure S-parameters with small tickle tones while the device under test is operated under large signal conditions using a large main tone. These S-parameters are then used to calculate typical design parameters, such as stability k-factor, stability circles and gain figures of merit.

### **3.2 SYSTEM-DESIGN PLATFORM**

LabVIEW (Laboratory Virtual Instrument Engineering Workbench) is a development environment for a visual programming language from National Instruments (NI). It is used to define the architecture, modules, interfaces, and data for a system to fulfil the end-user requirements. This allows not only for software-controlled measurements, but the facility to analyse data, generate results, and also design custom engineering user interfaces while the hardware has fixed functionality. Meanwhile, it can easily configure the same

---

---

measurements used in hardware to achieve multiple purposes, consecutively, and it reduces the cost of testing.

Nevertheless, building up the software to control the system's hardware of two chassis is not a straightforward task. It is required to have an in-depth understanding of the hardware. Indeed, knowing the functionality of each module in the chassis is essential to precisely control the system and achieve accurate measurements.

To demonstrate the functionality of the software, an Arbitrary Waveform Generator (AWG) was used to generate two-tones ( $T_1$  and  $T_2$ ). The first tone was generated at 1 GHz while the other tone spaced 100 kHz from the main-tone. The centre frequency of the receiver was set at 1 GHz to down-convert the RF signal to an intermediate frequency (IF). SMA (SubMiniature version A) cable is used to connect between the generator and the receiver as shown below.

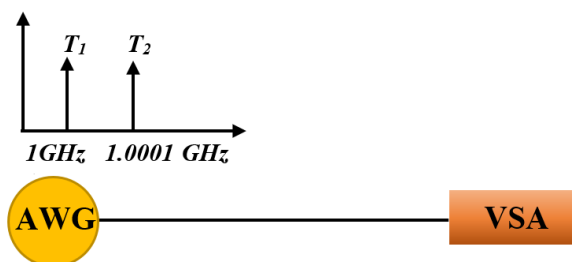


Figure 3-1: Experiment for a two-tone generation.

Each tone was swept in phase from  $0^\circ$  to  $360^\circ$  with a  $15^\circ$  step while the magnitude was kept constant for both tones. Figure 3-2 shows the

---

comparison of the resultant circles between the setting and the measured data of the second tone. It highlights that the phase of the second tone is in error, which causes a random phase to be observed in the received data.

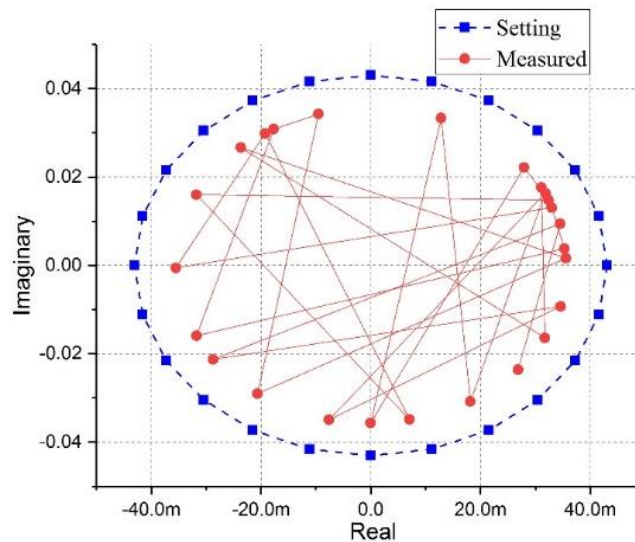


Figure 3-2: 24 phase step measurements of the second tone.

To achieve accurate stimulus control and receiver measurement, an investigation was made to tackle the phase issue. Three main points were observed, which affect the accuracy of phase measurement as follow:

- The way of multi-tone generation was based on the configuration of the RFSA and RFSG, initiates signal generation (causing the NI-RFSG device to leave the configuration state and enter the generation state) and abort the measurement while this method was repeated at each phase step. This resulted in the Local Oscillator (LO) having a different phase for each measurement

step. Therefore, a new approach was developed. In this case, all the complex I and Q waveform for each required phase step were downloaded at the same time using a script mode to be generated and acquired by the VSGs and VSAs, respectively thus all phases are measured in one measurement cycle. Thus, yielding constant LO phase at each phase step.

- The trigger is implemented using programmable function inputs and outputs (PFIs) for synchronising the two chassis. NI-RFSA and NI-RFSG both have multiple triggering and options to synchronize these devices with other devices in the PXI system and devices external to the PXI chassis. This flexibility allows the NI RF platform to be used for many different applications that require complex synchronization schemes. Therefore, for more precise alignment to the generated waveform, and fast trigger response times the “marker event” was used. This method of triggering utilises a NI-RFSG (VSG) generated trigger signal at the time that a specific location or sample  $n$  in the waveform generates on the AWG analogue output connector and sent via a PFI cable to the analysers”. If the waveform loops multiple times in a segment, the marker is generated each time the waveform loops [2].

- Finally, to synchronise triggering of all channels' acquisitions (or generations), NI-RFSA & NI-RFSG chassis can share a standard 10 MHz reference clock between channels where the NI-TClk technique is automatically aligning the synthesised sample clock edges with resulting skews less than 500 ps [3]. The system now exhibits excellent performance; this improvement can be seen in Figure 3-3 and with different frequency spacing ( $\Delta f$ ).

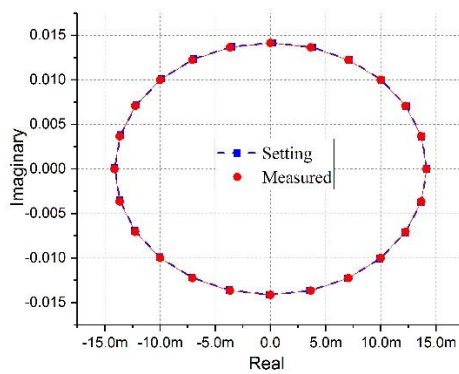
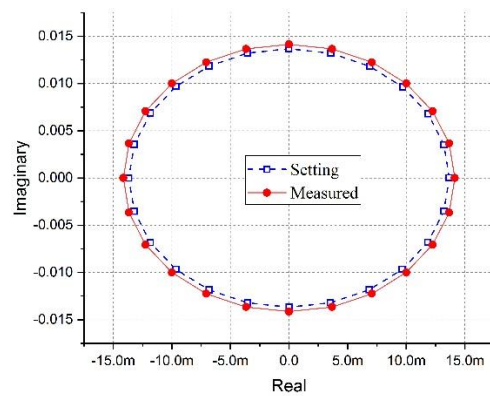
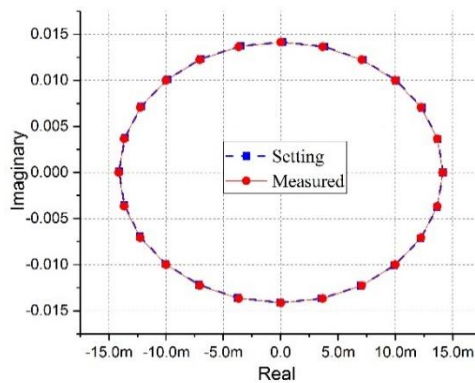
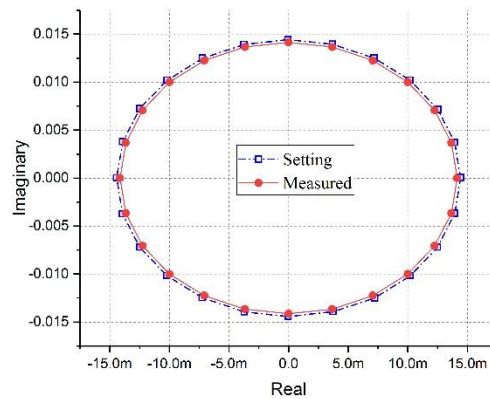
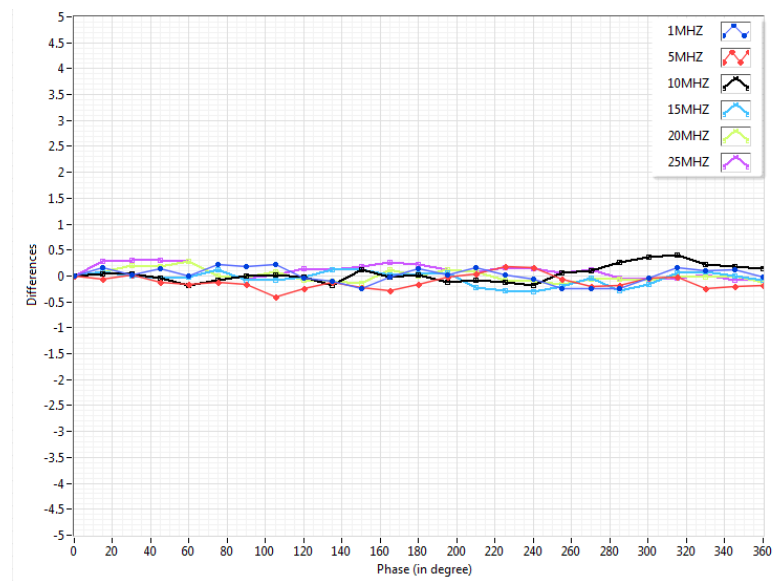
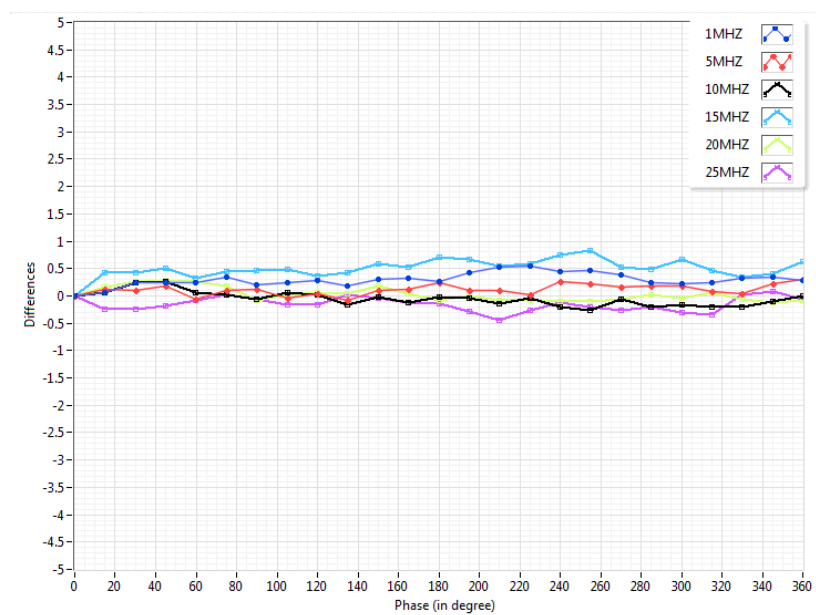
(a)  $\Delta f = 100 \text{ kHz}$ (b)  $\Delta f = 20 \text{ MHz}$ (c)  $\Delta f = 25 \text{ MHz}$ (d)  $\Delta f = 30 \text{ MHz}$ 

Figure 3-3: Setting and measured data comparison for different frequency spacing.

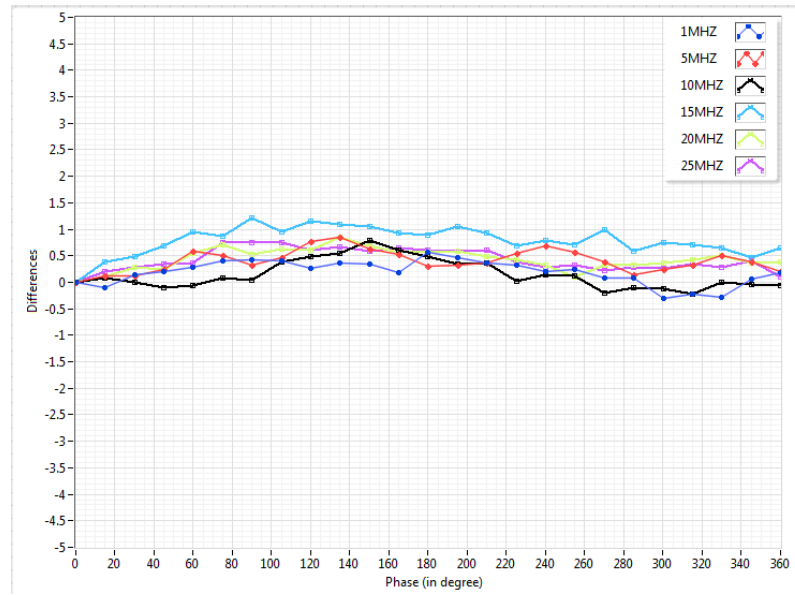
The same measurement was repeated with the different receivers (R2, R3 and R4) used in the system. Figure 3-4 reveals that slight differences in phase with maximum  $\pm 1.5^\circ$  for all receivers were observed. This gives an insight into the capability of the measurement system to achieve accurate phase measurements independent of receiver bandwidth.



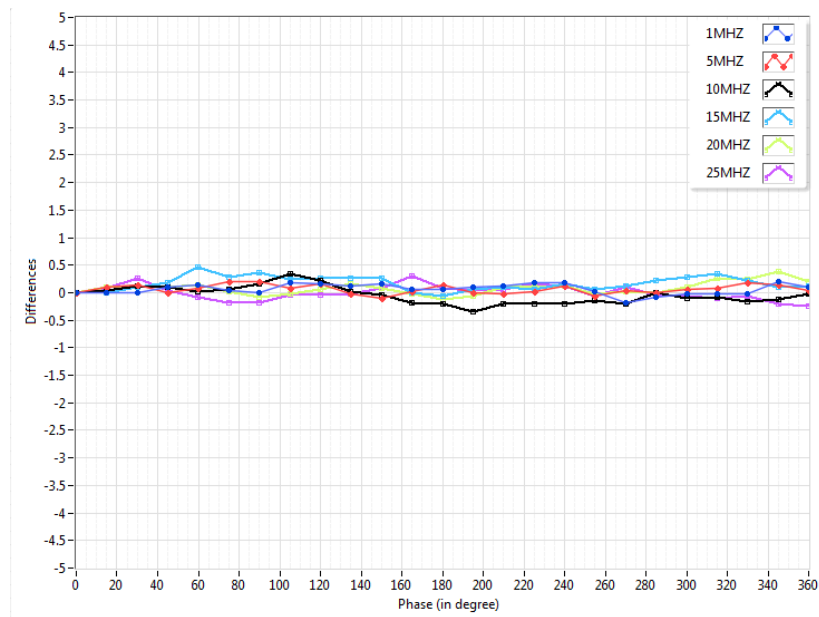
(a) Receiver 1 (R1)



(b) Receiver 2 (R2)



(c) Receiver 3 (R3)



(d) Receiver 4 (R4)

Figure 3-4: Differences between setting and measured data vs different phase steps.

These results show that necessary steps have been taken to ensure the objective to build up a LabVIEW code to control the hardware in a precise way in order to achieve accurate measurement and characterise the DUT under controlled multi-tone stimulus. First, in this chapter, the multi-tone stimuli measurement capability will be utilised to demonstrate the use of the system to measure load-pull contours. Then a solution is presented that allows additional parameters, such as stability circles to be computed while performing large signal stepped load measurements. In the following chapters, the multi-tone stimuli and measurement capability will be utilised to advance the extraction of transistor behavioural models.

### **3.3 POWER CONTOUR MEASUREMENTS UNDER MODULATED SIGNAL EXCITATION**

The measurement of load-pull power contours is vital for RF designers. Knowing the optimum impedance point (max  $P_{out}$  or efficiency) is insufficient for matching network, design contour information is also necessary. It allows setting the adequate impedance environment for the DUT to optimise the device performance by examining all the features of interest simultaneously. This is typically done by performing a number of CW measurements for a sequence of load impedances. Alternatively, this can be done in a one multi-tone

---

measurement. If the single tone active load-pull stimulus (CW) is replaced by a multi-tone stimulus the load is effectively time-varying.

Such a single measurement can be used to compute the power contours. However, the resulting contours first achieved were clearly in error. The centre point of the contours, the optimum load impedance point, disagrees with the optimum 10W GaN (from Wolfspeed (CGH40010F)) device performance (maximum output power) determined from the traditional, step load CW measurements as can be seen in Figure 3-5.

Optimum load of CW measurements

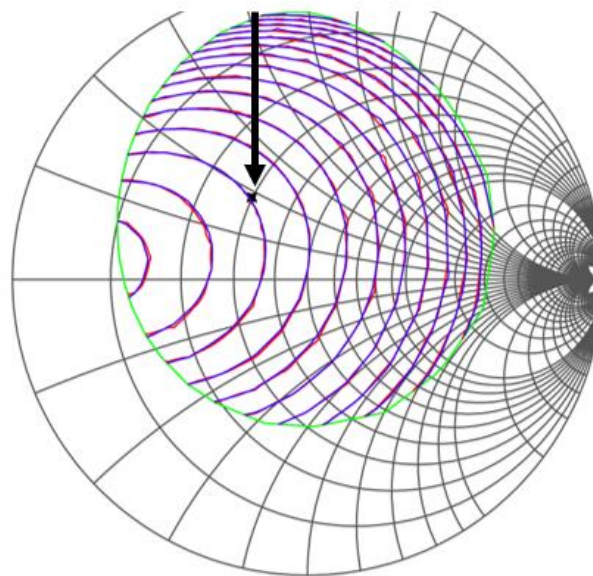


Figure 3-5: Modelled vs measured power contours for modulated signal excitation.

In this example, the spectral components of the resultant mixing terms above the noise floor all used the same error coefficients, i.e. that of the main-tone ( $f = 1$  GHz). In this case, the system was

calibrated using the traditional CW calibration approach. Over this modulation bandwidth, this clearly provided inaccurate error corrected measurements. The software was thus modified to allow for full calibration across the modulated bandwidth. Using this approach, the measurements were repeated, and the obtained results are plotted again as shown in Figure 3-6. In this case, the computed powers contours are consistent with those obtained from the stepped load CW measurements.

In Figure 3-7 a set of time sampled load impedances resulting from performing load-pull using active multi-tone load-pull stimulus is shown. A subset of loads was selected giving very different output power levels (in red circles) to be compared directly with CW load-pull measurements.

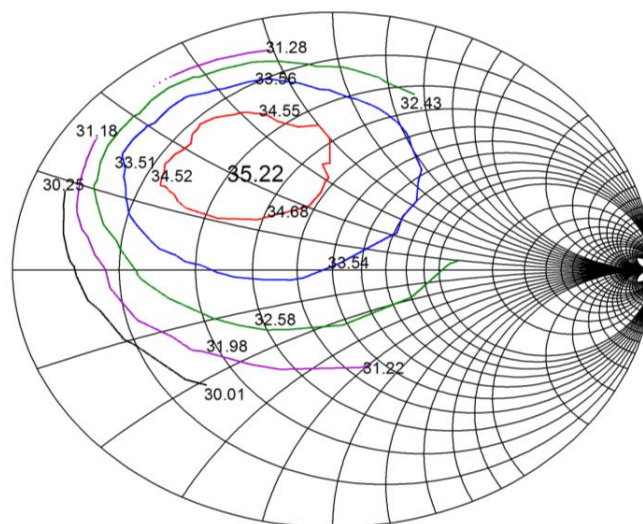


Figure 3-6: Power contour plots for the multi-tone stimulus.

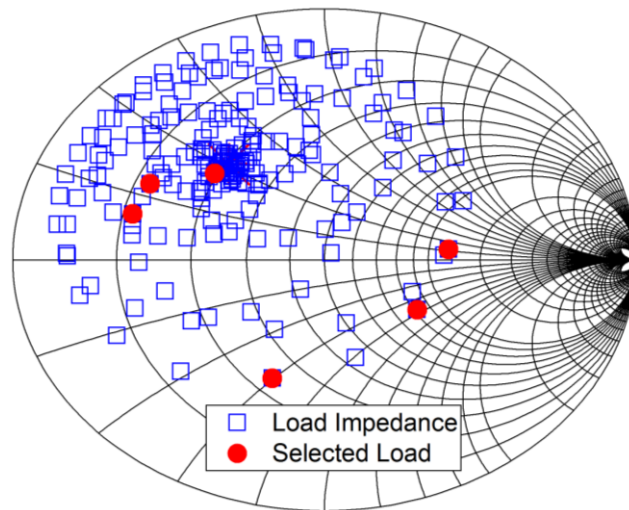


Figure 3-7: Impedance loads for modulated tone.

In Table 3-1 the measured output powers at these selected load impedances are presented. It shows that the maximum difference between the modulated measurements load-pull approach and traditional stepped load CW measurements approach is less than 1dB. It indicates the obtained modulated measurements load-pull contours can be considered equivalent to the CW measurement load-pull contours. It demonstrates that a single modulated measurement is an effective way of saving time while covering a substantial area on the Smith Chart since a single measurement can replace many CW stepped load-pull measurements. The developed software with accurate synchronisation between the two chassis has provided a framework to develop new measurement concepts.

Table 3-1: Comparison of  $P_{out}$  for the selected load impedances in active load-pull measurements.

Selected impedances	Pout (dBm) for modulated signal	Pout (dBm) for CW signal
$-0.351089 + 0.343549 i$	35.17	35.07
$-0.558582 + 0.302904 i$	34.48	34.2
$-0.614492 + 0.182831 i$	33.55	33.77
$0.398767 + 0.0417905 i$	32.44	32.00
$0.298212 - 0.198977 i$	31.77	32.12
$-0.166506 - 0.471614 i$	30.64	31.59

### 3.4 TICKLE-TONES MEASUREMENTS IN ACTIVE LOAD-PULL SYSTEM

In recent years, many studies were presented about the load-pull techniques and their use is characterising the device under test (DUT) in large signal regime [4-6]. These techniques assist in determining the appropriate matching impedance values in the non 50 Ohm region. Measuring power performance as a function of load impedance allows for the extraction of useful figures of merit that help to meet the design target, for instance, output power, efficiency, gain, and power-added efficiency, from the DUT. Information such as gain is challenging to be identified in real time during active load-pull measurements as the measured  $S_{12}$  and  $S_{22}$  are inaccurate since the  $b_2$  signal is affected

directly by the input signals  $a_1$  and  $a_2$ . Accurate S-parameters can be extracted from a set of load-pull data after a complete load-pull measurement has been performed. Only then would accurate gain figures be calculable.

This section presents a new approach of providing complementary information for RF designers by the inclusion of two additional tickle-tones with different frequency spacing during load-pull measurements. These tickle tones allow for the computation of the transistor S-parameters about a large signal operating point simultaneously in real time that is now defined not just in terms of the DC bias point, but also in the level of the large signal input stimulus and the respective load impedance. In addition, various system impedances can also be measured. This additional information allows for parameters, such as stability circles, to be computed while performing large signal load-pull measurements. Thus, enabling the monitoring of the stability of the DUT at each load point under large signal excitation. In addition, measuring small-signal S-parameters allows the calculation of the source impedance (gamma source ( $\Gamma_S$ )) at the input. This can be helpful in the calculation of different gain figures which account for the source mismatch such as available gain  $G_A$  and transducer gain  $G_T$ .

---

### 3.5 TICKLE-TONE VERIFICATIONS UNDER LARGE-SIGNAL INPUT

To simultaneously determine all four S-parameters of the DUT as well as the source and load reflection coefficients two tickle-tones  $T_1$  and  $T_2$  at different frequencies are injected into the device's two ports as shown in Figure 3-8, as well as the fundamental signals  $a_{1F}$  and  $a_{2F}$ .

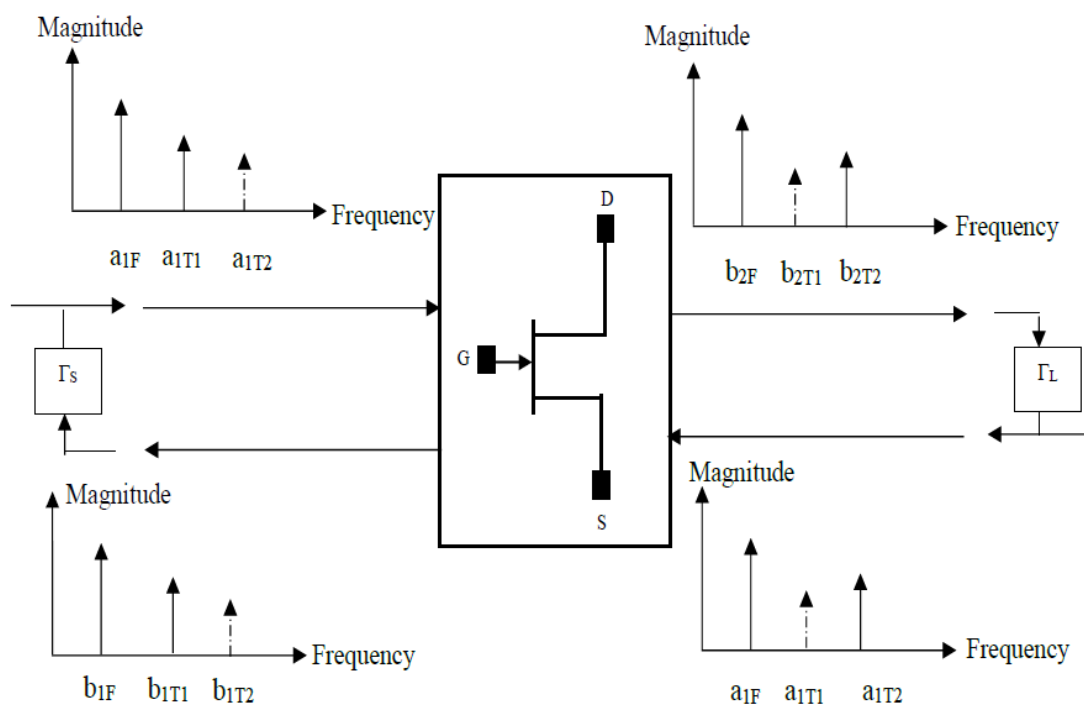


Figure 3-8: A simplified conceptual view of input-output tones for the device measurements.

The frequency offsets between the fundamental and tickle tone frequencies are chosen in such a way that no mixing terms will interfere with the injected three frequencies. The tones are placed sufficiently close to ensure that the S-parameter measurements reflect the DUT performance at the fundamental frequency. Due to the non-ideal source and load impedances, the incident and reflected traveling

waveforms will be reflected back represented by dash lines in Figure 3-8, allowing for the simultaneous measurement of all four S-parameters using the following relationships.

$$S_{11} = \left. \frac{b_{1T1}}{a_{1T1}} \right|_{a_2T_2=0} \quad S_{21} = \left. \frac{b_{2T1}}{a_{1T1}} \right|_{a_2T_2=0} \quad (3-1)$$

$$S_{22} = \left. \frac{b_{2T2}}{a_{2T2}} \right|_{a_1T_1=0} \quad S_{12} = \left. \frac{b_{1T2}}{a_{2T2}} \right|_{a_1T_1=0} \quad (3-2)$$

An additional experiment was performed using a thru calibration standard to verify the tickle-tone measurements in the presence of the main-tone. During the first investigation, the injected power of the  $a_1$  and  $a_2$  signals at the main-tone frequency was kept constant at 24.6dBm and the power of the tickle-tone swept from 0dBc to -80dBc while the frequency of the  $T_1$  and  $T_2$  was set to 100 kHz and 250 kHz respectively.

Figure 3-9 shows the resulting deviation in phase and magnitude starting at -70dBc offset. These measurements indicate a dynamic range of up to -70dBc for the measurement system. To determine the available power range for characterization of active devices, it is also important to identify the maximum power offset that avoids significant impact on the large-signal performance. Ideally, the tickle tone should not be affecting main-tone measurements while still providing sufficiently accurate readings for S-parameter and impedance determination.

In a second investigation, tickle tone measurements were carried out using a deep class-AB bias point at  $IDQ = 11\text{mA}$  and  $VDS = 28\text{V}$  with the main tone impedance set for optimum power at  $\Gamma_L = -0.166415 + j0.102536$ , which was determined separately from CW measurements.

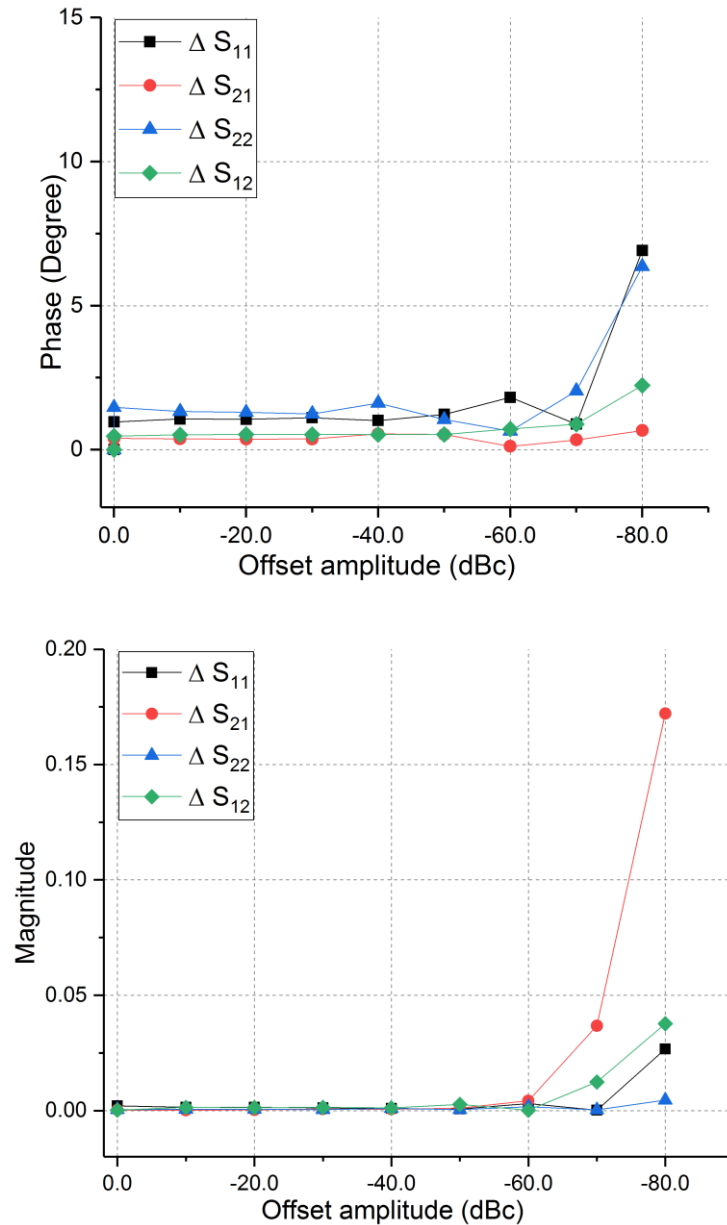


Figure 3-9: Magnitude and phase difference for S-parameters in the main and the tickle tones versus offset Amplitude.

The output impedance of the tickle-tones and harmonics was kept at 50 Ohm. Figure 3-10 shows three different power-offset levels on a CW stepped input power measurements to identify the impact of tickle-tones on the power added efficiency (PAE) of the device. The PAE of each power-offset level was calculated, and then the differences with the PAE of the CW tone were computed individually. It is apparent that offset levels  $\leq -20$  dBc are required to limit the impact on device efficiency to less than 5%.

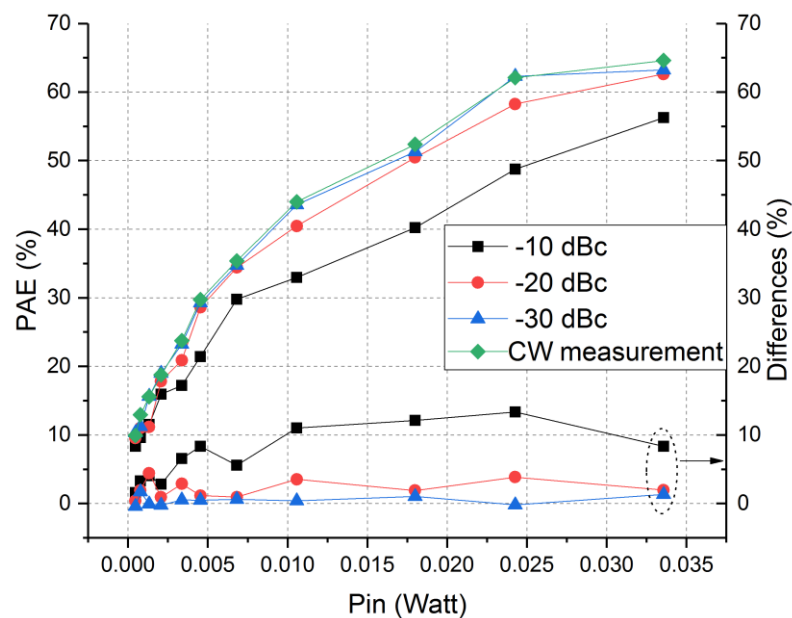


Figure 3-10: PAE for different power-offset levels.

### 3.6 STABILITY ANALYSIS

Oscillation takes place in active circuit elements such as a transistor, where reflection coefficient magnitudes might exceed unity. This means the reflected signal is larger than the incident signal. Note, resistance circles with negative values are always outside of the unit-

radius on the Smith Chart. This may only be happening for some applied bias conditions, frequency range, load impedance and increased signal levels.

Stability analysis is normally carried out using Rollets stability criteria parameters, computed from the DUT S-parameters, [7, 8], unconditional stability happens under the condition when the  $K > 1$  and  $|\Delta| < 1$  (see Eq. (3-3)). If this condition was not satisfied, it is called potentially unstable, traditional stability circles should be used to further investigate the problem [9]. A stability circle is a border between the stable and unstable terminations where a stability circle for the load terminations is plotted. This analysis can also be performed on the S-parameters determined by the tickle-tones, both as a function of drive level and load impedance.

The frequency of the main tone was generated at 1GHz while  $T_1$  and  $T_2$  were set to 100 kHz and 250 kHz respectively. In addition, the large-signal input was set to 18.95dBm, and the tickle-tones were set to -20dBc from the stimulus.

$$K = \frac{1 - |S_{11}|^2 - |S_{22}|^2 + |\Delta|^2}{2 |S_{12}S_{21}|} \quad (3-3)$$

$$\Delta = S_{11}S_{22} - S_{12}S_{21} \quad (3-4)$$

K-factor shows values less than one, as shown in Figure 3-11. Therefore, conditional stability is found in this measurement. It is worth noting that when  $|\Gamma_{in}| > 1.0$ , oscillation may take place at the input port. If  $|\Gamma_{in}| < 1.0$ , the input port is stable while  $|\Gamma_{in}| = 1.0$  lies on the borderline. To define whether the region inside the stability circle represents stable or unstable termination, the 50 Ohm point is considered. Since,  $|S_{11}|$  for all points are  $< 1$  (See Figure 3-12), the regions outside the stability circles are stable.

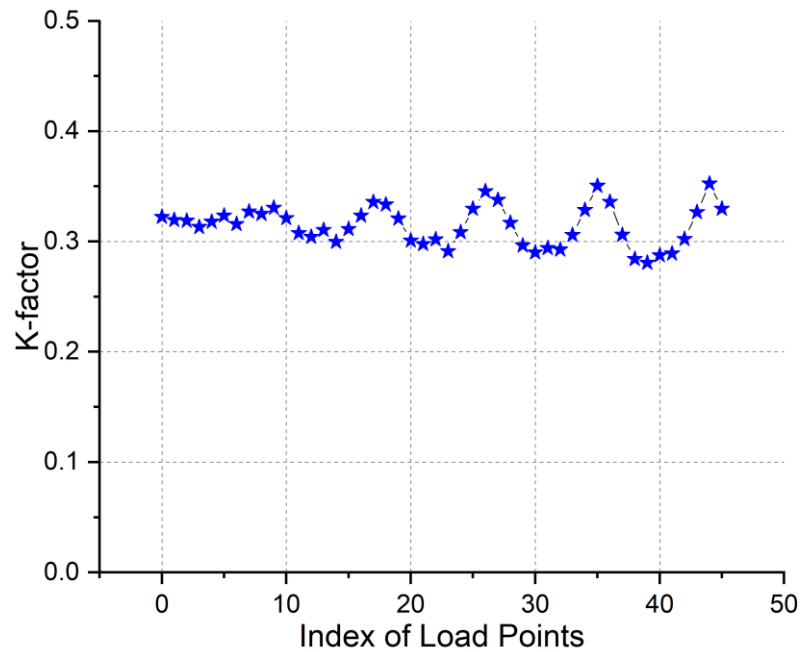


Figure 3-11: K-factor for different load points.

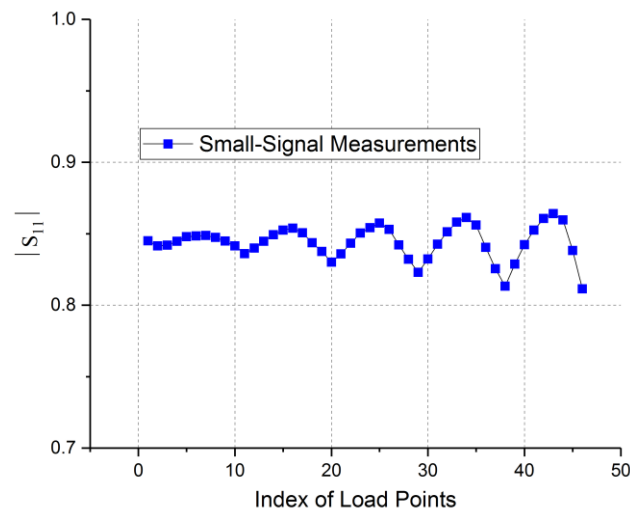


Figure 3-12:  $|S_{11}|$  for small-signal S-parameters.

Figure 3-13 illustrates the beneficial extracted knowledge of stable (in blue), and unstable loads (in red) during load-pull measurements. Such information is required to avoid designing a PA that would be operating in an unstable region or performing measurements under conditions that can damage the DUT or measurement system. It is worth noting that in this case the stability analysis can be performed at each measured load impedance, hence the high number of stability circles being plotted on the Smith Chart.

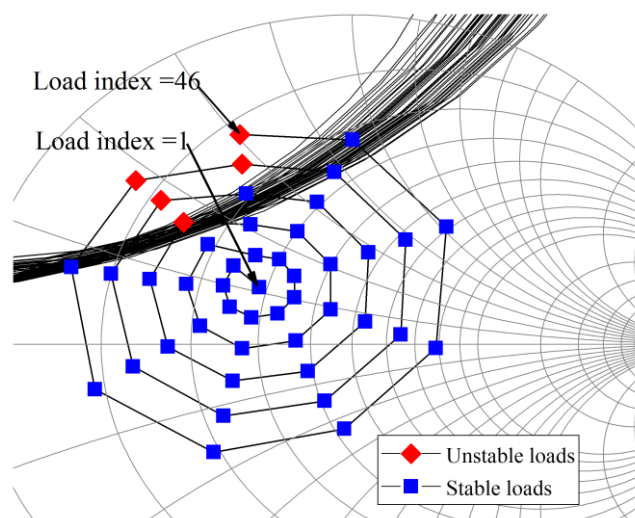


Figure 3-13: Stability analysis in active load-pull system.

Having unstable loads means that the  $|\Gamma_{in}| > 1$  (Gamma in represents the true input reflection coefficients of the two-port, with an arbitrary load termination,  $\Gamma_L$ ) in small-signal measurements. To validate the results, the input reflection coefficient is calculated using the small-signal S-parameters (Tickle tone) and then compared with the large-signal measurements (Main-tone) as shown in Figure 3-14. The results show good agreement between them which indicates that this approach is robust enough for useful data extraction during load-pull measurements. It is worth noting that the red colour indicates when  $|\Gamma_{in}| > 1$ ; which corresponds to the load being potentially unstable in Figure 3-13. Also, the discrepancy between the two measurements is identified where the unstable load for the large-signal measurements is seven while for small-signal measurements is only five. This discrepancy would increase as the density of load points is increased. This is due to the small-signal S-parameter measurements always giving an input reflection coefficient less than the large-signal S-parameter measurements when the loads are close to the threshold of stability (given by an input reflection coefficient  $\Gamma \geq 1$ ). This demonstrates the importance of having small-signal measurements with the presence of the large-signal input for monitoring the stability of the loads in real-time.

---

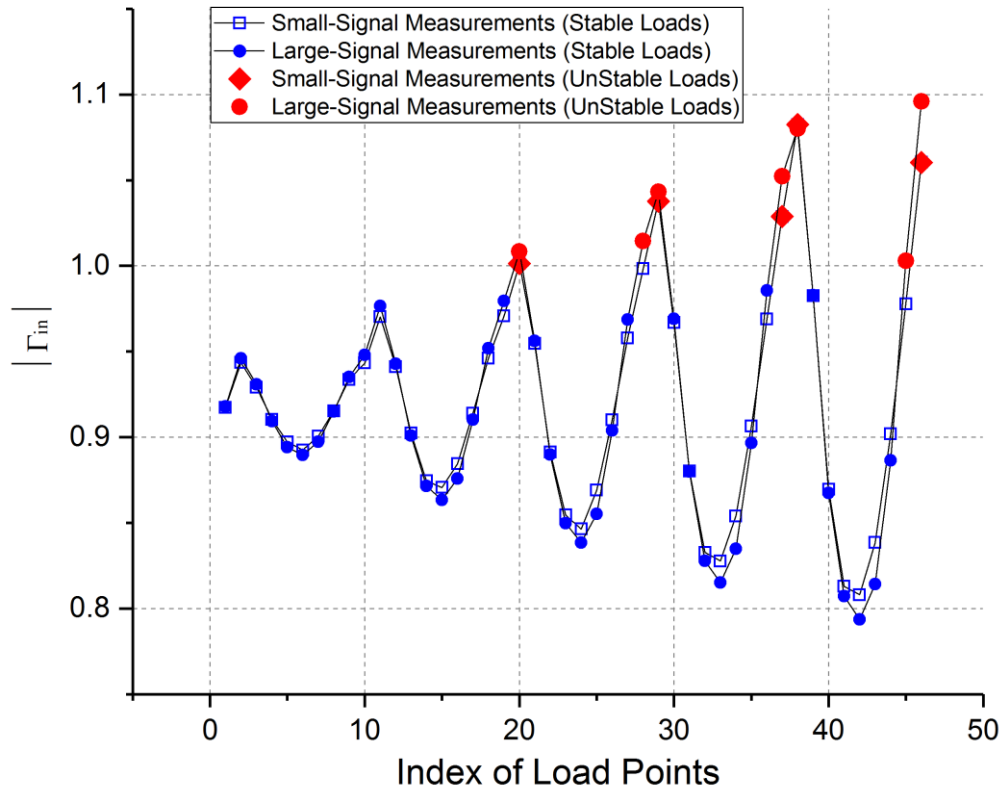


Figure 3-14:  $|\Gamma_{in}| > 1$  for large-signal and small-signal analysis versus the index of load points.

On analysing the results, as shown in Figure 3-15, the power gain (see eq.(3-6)) [10] calculated using the small-signal ‘tickle-tone’ measured S-parameters and large-signal measurements have good agreement. Note, at some points, the gain cannot be identified under the conditions that  $|\Gamma_{in}| > 1$ . Meanwhile, extracting small-signal S-parameters allows for other gain figures to be calculated, such as available gain ( $G_A$ ) and transducer gain ( $G_T$ ) with no extra cost as in (3-7) and (3-8) [10] as they account for the mismatch at the source port. Thus, due to the imperfection of the isolator, the  $\Gamma_s$  was calculated by measuring the incident and reflected waves of  $T_2$  at port1.

$$\Gamma_s = \frac{a_{1T2}}{b_{1T2}} \quad \Gamma_L = \frac{a_{2F}}{b_{2F}} \quad (3-5)$$

$$G_p = \frac{P_L}{P_{in}} = \frac{|S_{21}|^2 (1 - |\Gamma_L|^2)}{(1 - |\Gamma_{in}|^2) |1 - S_{22}\Gamma_L|^2} \quad (3-6)$$

$$G_A = \frac{P_{avn}}{P_{avs}} = \frac{|S_{21}|^2 (1 - |\Gamma_s|^2)}{(1 - S_{11}|\Gamma_s|^2) (1 - |\Gamma_{out}|^2)} \quad (3-7)$$

$$G_T = \frac{P_L}{P_{avs}} = \frac{|S_{21}|^2 (1 - |\Gamma_s|^2) (1 - |\Gamma_L|^2)}{|1 - \Gamma_s \Gamma_{in}|^2 |1 - S_{22}\Gamma_L|^2} \quad (3-8)$$

$$\Gamma_{OUT} = S_{22} + \frac{S_{12} S_{21} \Gamma_s}{1 - S_{11} \Gamma_s} \quad (3-9)$$

$$\Gamma_{IN} = S_{11} + \frac{S_{12} S_{21} \Gamma_L}{1 - S_{11} \Gamma_L} \quad (3-10)$$

The subscript  $T_2$  and F in (3-5) refer to the second tone at the load-side and the fundamental-tone/the stimulus of the device respectively. The  $(\Gamma_s)$  values are shown to be close to 50 Ohm impedance load as shown in Figure 3-16.

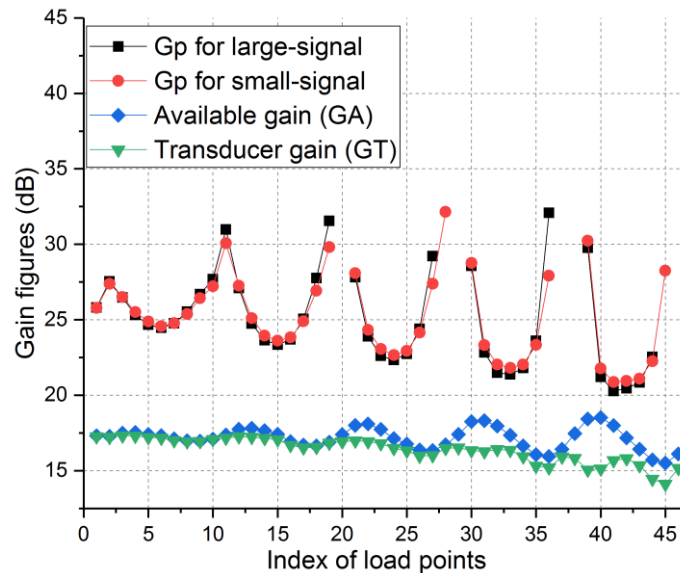


Figure 3-15: Power gain figures for large and small signal S-parameters.

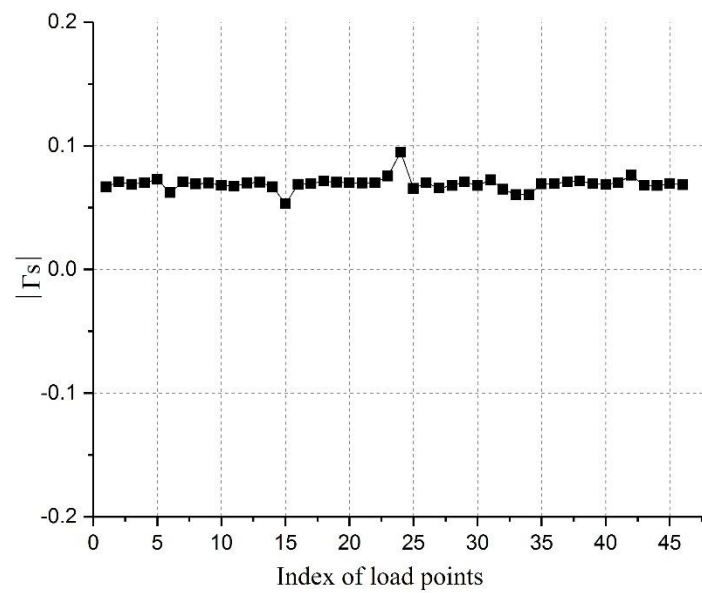


Figure 3-16:  $|\Gamma_s|$  for different load impedance points.

A new experiment was done to examine the stability of the device at a 50 Ohm load with five different power inputs ( $a_1$ ) starting at 22.7dBm to 4.8dBm while keeping the tickle-tone at fixed power level = 2.64dBm as shown in Figure 3-17.

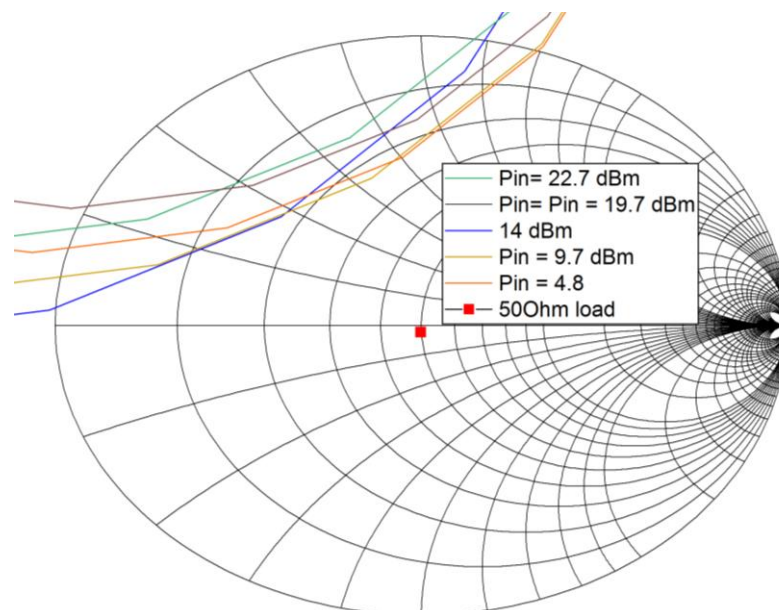


Figure 3-17: Stability circles at 50 Ohm with different power inputs.

The final measurement was repeated with the same power input levels but at the optimum load for maximum output power (see Figure 3-18). On analysing the result, both measurements have shown the unstable region is located at the upper left side on the Smith Chart, which gives an indication to avoid designing a PA inside this region which might end up designing an oscillator.

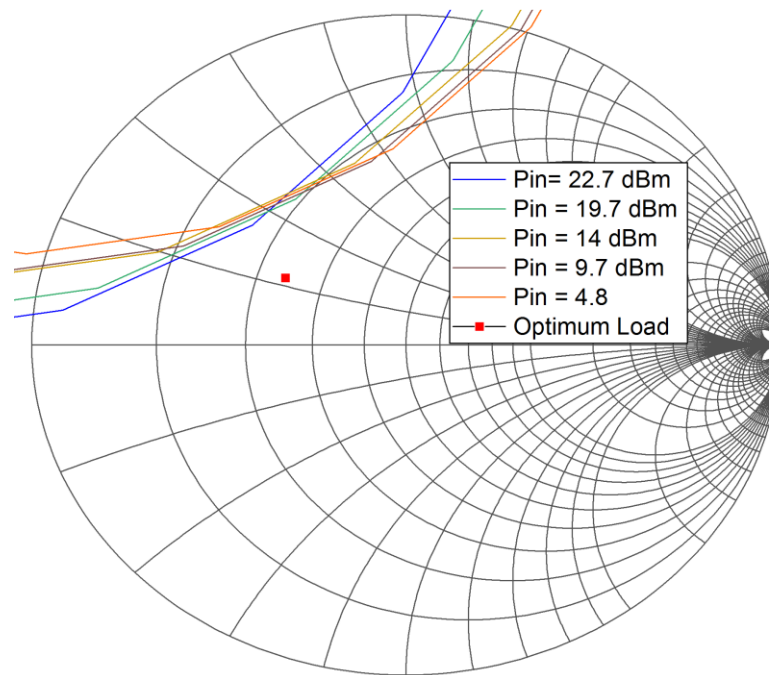


Figure 3-18: Stability circles at the optimum load impedance with different power inputs.

### 3.7 CHAPTER SUMMARY

This chapter set out with the aim of assessing the importance of having an accurate high-speed measurement system based on PXIe modules. Experimental verification of generating multi-tone signal was described and documented. Results showed an inaccurate phase

measurement when the second tone spaced more than 100 kHz from the main tone and how the problem was tackled.

The second part of this chapter was dedicated to utilising the developed LabVIEW code, allow for accurate measurements under multi-tone excitation, to extract, using a new approach, relevant design data during load-pull measurements in an active load-pull system. The approach developed uses the injection of tickle tones, hence a multi-tone stimulus, in addition, the main tone needed for classical fundamental load-pull, to determine S-parameters as function of both input drive level and output load impedance. It was determined that setting the tickle-tones to -20dBc was sufficient to collect the required data for stability and gain calculation without distorting the main tone measurements. Two experiments were presented showing the variation of the stability region for different loads and different power inputs. Finally, an example of new measurements that can be performed using such a system was presented. The system was used to measure device S-parameters with the presence a large-signal input. The advantage of this is that it allows for the capability to compute stability circles and other gain figures in real time whilst active load-pull measurements is running.

---

## REFERENCES

1. Husseini, T., et al. Automating the Accurate Extraction and Verification of the Cardiff Model via the Direct Measurement of Load-Pull Power Contours. in 2018 IEEE/MTT-S International Microwave Symposium-IMS. 2018. IEEE.
2. National Instruments. *Marker Events*. Available from: [http://zone.ni.com/reference/en-XX/help/370524V-01/siggenhelp/ni\\_5421\\_markers/](http://zone.ni.com/reference/en-XX/help/370524V-01/siggenhelp/ni_5421_markers/).
3. Hall, D., A. Hinde, and Y. Jia. Multi-channel phase-coherent RF measurement system architectures and performance considerations. in 2014 IEEE Military Communications Conference. 2014. IEEE.
4. Ghannouchi, F.M. and M.S. Hashmi, *Load-Pull Techniques with Applications to Power Amplifier Design*. 2012: Springer Netherlands.
5. Hashmi, M.S., et al., *Highly reflective load-pull*. IEEE Microwave Magazine, 2011. **12**(4): p. 96-107.
6. Hashmi, M.S. and F.M. Ghannouchi, *Introduction to load-pull systems and their applications*. IEEE Instrumentation & Measurement Magazine, 2013. **16**(1): p. 30-36.
7. Rollett, J., *Stability and power-gain invariants of linear twoports*. IRE Transactions on Circuit Theory, 1962. **9**(1): p. 29-32.
8. Platzker, A., W. Struble, and K.T. Hetzler. Instabilities diagnosis and the role of K in microwave circuits. in 1993 IEEE MTT-S International Microwave Symposium Digest. 1993. IEEE.
9. Gilmore, R. and L. Besser, *Practical RF Circuit Design for Modern Wireless Systems: Active Circuits and Systems, Volume 2*. Vol. 1. 2003: Artech House.
10. Pozar, D.M., *Microwave engineering*. Wiley, 2012.

# CHAPTER 4

## NON-LINEAR BEHAVIOURAL MODELLING

### 4.1 INTRODUCTION

**B**ehavioural models are a necessary tool to transport device data, from developing technology, into CAD for further design related analysis. The behavioural model is a black-box framework that reduces the prototyping cost and development time by allowing for the utilization of CAD tools much earlier in the design cycle. Accurate performance is very dependent on the interpolation and extrapolation capabilities of the modelling approach. As a consequence, approaches to push the boundary of the behavioural modelling to be more accurate and robust in the non-linear domain, as well as seamless integration with several CAD packages, form an important research topic.

This chapter reviews the development of nonlinear behavioural modelling approaches starting from Poly-Harmonic Distortion (PHD) modelling, through the X-Parameters to the Cardiff Model. The problem of model parameter extraction is reviewed. Subsequently, the usefulness of utilising two-tone stimulus for Cardiff behavioural model identification.

## 4.2 POLYHARMONIC DISTORTION (PHD) MODEL

It is a black-box frequency modelling technique, which was first described by J. Verschpect and D.E Root [1, 2]. The author supposed that only one large signal is dominant while the other tones are small and harmonically related to each other. Also, the PolyHarmonic Distortion (PHD) model is simplified to S-parameters when a small signal drives the DUT.

### 4.2.1 PHD MODEL FORMULATION

Figure 4-1 shows a non-linear 2-port device network. It illustrates the concept of fundamental and harmonic travelling waves and capturing their behaviour in the system, and it is assumed that the fundamental tone is constant. The PHD model is based on a presumption that the small signals introduce a small perturbation in a system and can be treated as a linear perturbation to any spectral line within a network, this is called the superposition theorem [3].

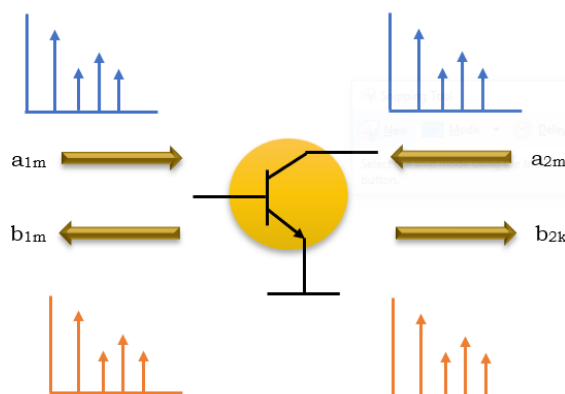


Figure 4-1: 2-port device network for travelling waves.

A simple equation can be started as shown below:

$$B_{pm} = F_{pm}(A_{11}, A_{12}, \dots, A_{21}, A_{22}, \dots) \quad (4-1)$$

$F_{pm}(\cdot)$  is called a described function which is used to correlate the input a-waves with the output b-waves in the frequency domain, whereas  $p$  is the port number and  $m$  is the harmonic index. This model aims to know the behaviour of the system for all harmonic products rather than the fundamental frequency alone. The distinct attributes of the described function  $F_{pm}(\cdot)$  are the time-invariance and the non-analyticity [4].

The time-invariant system means that when the a-waves are delayed in time we will have the same amount of the delay in all the resulting b-waves. In the frequency domain, this delay is expressed as a linear phase shift as clarified below.

$$B_{pm}e^{jm\theta} = F_{pm}(A_{11}e^{j\theta}, A_{12}e^{j2\theta}, \dots, A_{21}e^{j\theta}, A_{22}e^{j2\theta}) \quad (4-2)$$

To simplify the equation, phase normalisation was introduced whereas  $P$  is the phase of  $A_{11}$ . This leads to  $A_{11}$  being the dominant signal hence other signals are phase normalised to  $A_{11}$ .

$$P = e^{j\theta(A_{11})} \quad (4-3)$$

Substituting  $e^{j\theta}$  by  $P^{-1}$  in (4-2) resulted in

$$B_{pm} = F_{pm}(|A_{11}|, A_{12}P^{-2}, A_{13}P^{-3}, \dots, A_{21}P^{-1}, A_{22}P^{-2}, \dots)P^{+m} \quad (4-4)$$

The above equation is beneficial for simplifying the upcoming process, as the first input will always have a positive real number rather than having a complex number. Furthermore, the second harmonic term would be shifted in phase twice as much as the fundamental frequency and three times for the third harmonic. The spectral map in eq. (4-5) can be linearized around the large-signal operating point (LSOP) while other small spectral components are treated as small perturbations. The non-analytical nature is the second postulate to describe a function  $F_{pm}(\cdot)$ . It produces a conjugate term in the below equation and can be treated separately while S-parameters are free of this term because a linear function is analytic.

$$B_{pm} = \sum_{qn} S_{pq,mn}(|A_{11}|)P^{m-n}A_{qn} + \sum_{qn} T_{pq,mn}(|A_{11}|)P^{m+n}A_{qn}^* \quad (4-5)$$

The above equation defines  $p$  and  $m$  as a port number and harmonic of b-wave, while  $q$  and  $n$  are the port number and the harmonic of a-waves. It should be noted that  $S_{pq,mn}$  and  $T_{pq,mn}$  are known as model parameters while “S” is different from the linear S-parameters. As it can be seen, these parameters are non-linearity functions of  $A_{11}$  while the output waves have a linear relationship with other input waves. It

---

can be concluded that these parameters account for the effects of a non-linear effect of the fundamental input on the other harmonic output waves. For instance, “ $S_{21,13}$ ” and “ $T_{21,13}$ ” clarify the 3<sup>rd</sup> harmonic of the input signal affects the fundamental output. To sum up, “T” parameters are applied in PHD model to account for the non-linearity in DUT under large-signal input. These conjugate terms appear when the mixing of output and the input signal starts to influence the DUT response, resulting in an output that cannot be described by S-parameters alone.

The main limitation of the poly-harmonic distortion model is the assumption that  $A_{11}$  is the only large-signal a-wave that dominates the network behaviour, while other a-waves should be relatively small. This is considered a serious limitation under many realistic conditions. Load-pull measurements are required to find the optimum load under large-signal stimulus; optimum load can be far away from the reference impedance of 50 Ohms. This can lead to  $A_{21}$  having values that are not small compared to the input signal  $A_{11}$ . Hence,  $A_{21}$  cannot be treated as a small signal perturbation, and the harmonic superposition theorem cannot be applied.

### 4.3 X-PARAMETERS

X-parameters are considered a black-box modelling technique with a formulation based upon the Poly-harmonic Distortion (PHD) model [5]. X-parameters are a trademark of Keysight Technologies. They are a superset of S-parameters, and it is valid in linear and non-linear measurements where the harmonics and the intermodulation (IMD) products exist [6].

Equation (4-6) is just an updated PHD model equation to be applied in a large-signal input of the DUT and it is assumed all ports are perfectly matched. Similarly, this equation needs the DC biasing to be controlled for the two ports while independently changing the injected power at the input port, the incident power and the relative phase at the output port.

$$\begin{aligned}
 B_{pm} = & X_{Fpm}(|A_{11}|, V_{1,0}, V_{2,0}) + \\
 & \sum_{q,n} X_{pq,mn}^{(S)}(|A_{11}|, V_{1,0}, V_{2,0}) P^{+m-n} A_{qn} + \\
 & \sum_{q,n} X_{pq,mn}^{(T)}(|A_{11}|, V_{1,0}, V_{2,0}) P^{+m+n} (A_{qn})^*
 \end{aligned} \tag{4-6}$$

$X_S$  and  $X_T$  terms in the above equation are used to model the DUT mismatch at harmonic frequencies based on LSOP level power. These terms are accurately working if the harmonics signals are not large.

### 4.3.1 X-PARAMETERS MEASUREMENT

Three model coefficients  $X_F$ ,  $X_S$  and  $X_T$  terms are needed for X-parameters model extraction. The on-frequency technique sets the small-signal perturbations at frequencies exactly located with fundamental and harmonics of the large-signal stimulus. It needs more than one measurement as the output wave resulting from  $a_{ph}$  is unrecognisable from the part of the output resulting from  $a_{ph}^*$ . As it can be seen from Figure 4-2, a minimum of three measurements need to be performed. The first measurement is to extract  $X_F$  coefficient (symbolised by a red rectangle) whereas that large signal  $A_{11}$  is injected and should be kept constant throughout the measurements. To extract the rest of the coefficients, two independent measurements are applied by injecting an  $A_{21}$  signal with  $\theta = 0^\circ$  and  $90^\circ$  phase.

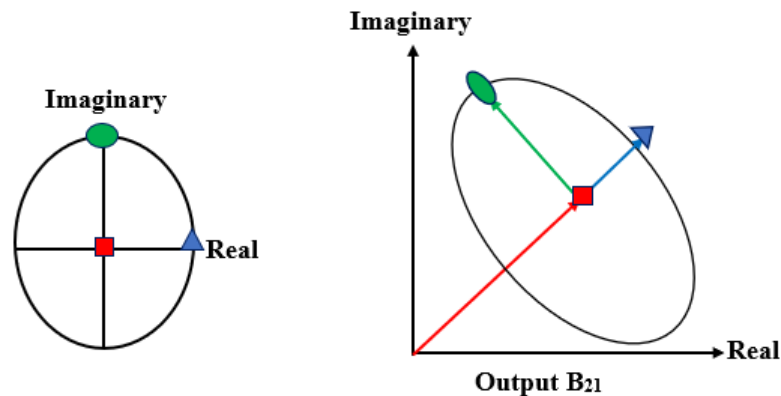


Figure 4-2: X-parameters extraction coefficients.

Figure 4-3, LSNA is used to measure the incident and reflected waves, and two generators are installed, the first one to generator a large-signal  $A_{11}$  while the second one is used with a switch to generate a small-signal named a “tickler signal” [1].

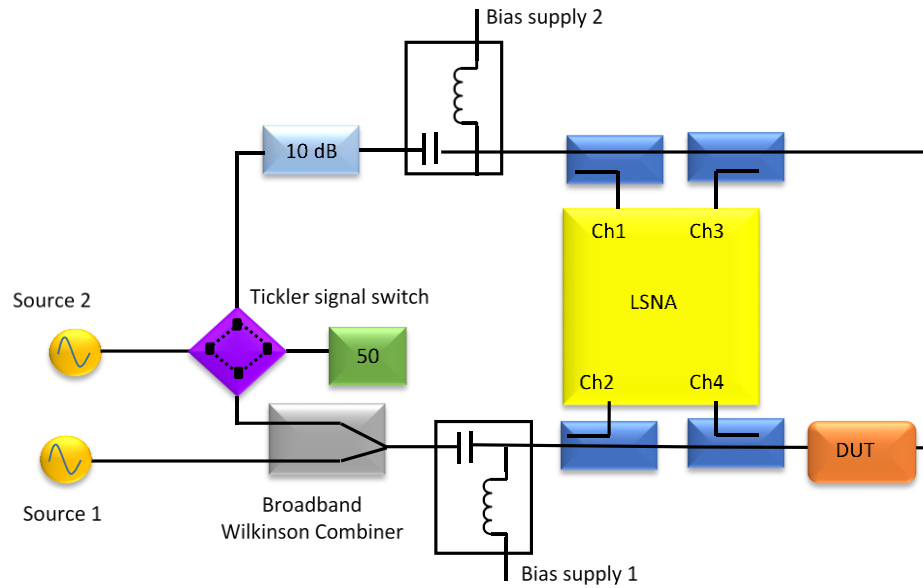


Figure 4-3: Block diagram of X-parameters measurement setup.

The main limitation of this approach is when measuring impedances far away from 50 Ohm, where the mismatch at the output becomes challenging to ignore. The variation of  $A_{21}$  is getting larger and harmonic superposition theorem no longer holds.

### 4.3.2 LOAD-DEPENDENT X-PARAMETERS

As stated in [1, 2, 8], in power transistors, the optimal load is located far from 50 Ohm. Therefore, the new measurement system or approach that enables the X-parameters to cover a larger area of the Smith Chart, not restricted to the area close to 50 Ohm, is required. Figure 4-4 depicts how the measurement system for load dependent X-parameters is configured to perform the measurements by using

PNA-X integrated with the load-pull system to extract X-parameters coefficients with the capability to cover the whole Smith Chart [7].

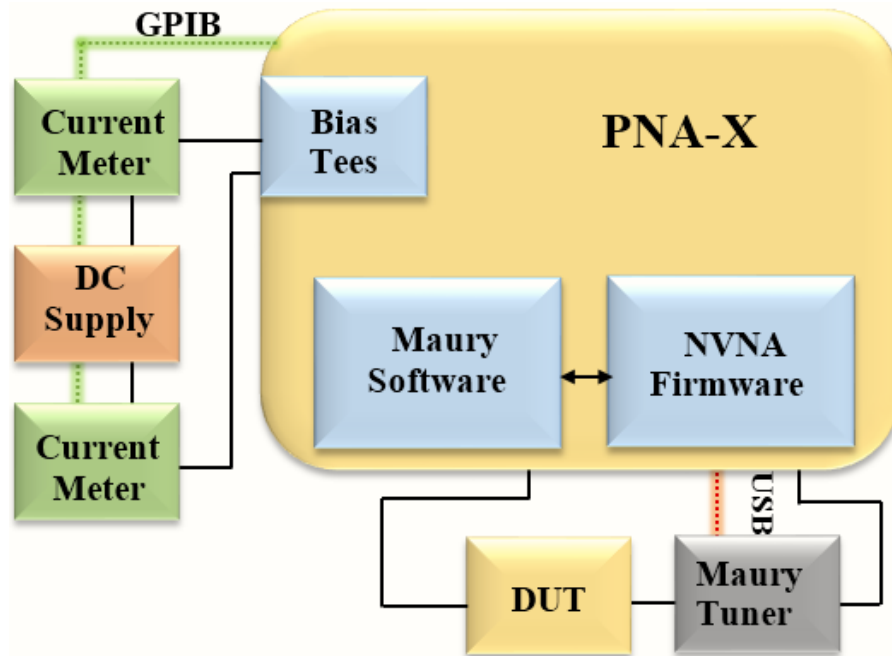


Figure 4-4: Load dependant X-parameters measurement system.

In this case, the load-pull is achieved using a tuner to sweep the impedance over the whole Smith Chart. The user interface is performed using the Maury software, which is loaded on PNA-X, and the GPIB is used to control the DC instruments. The tuners are used for Load-pull at each load where the X-parameters can be extracted and stored in a file, which then can be imported into the Advanced Design System (ADS) for simulation purposes.

To sum up, X-Parameter modelling was developed by Agilent and has become a powerful tool to be used in the non-linear design. Measurement of X-Parameters has been significantly advanced via the

introduction of the PNA-X system. Further model extensions to include long-term memory effects have also been proposed [9]. However, it is important to note that the analytical X-parameters approach is limited to three parameters XF, XS, and XT; which limits the model accuracy when the degree of non-linearity is increased. This leads to a model that is valid only over a limited area on the Smith Chart, hence the need for a load-dependent X-parameters look up table to address the whole Smith Chart. Unfortunately, the file size increases when the area of the Smith Chart is increased; i.e. the number of measurements is increased.

Nowadays, there is an increased requirement for not only fundamental load-pull but also harmonic load-pull. This must be done over a range of drive power level, DC bias, operating frequency, etc. As a consequence, the file size of load-dependent X-parameters is increasing significantly, even if simulator speed in Agilent ADS is not affected, problems are produced in data transfer and file storage. Thus, the Cardiff Model is considered a unique approach to cope with the data storage issue; especially it can extend the polynomial order which depends on the non-linearity of the system and covering a bigger area on the Smith Chart. The detailed discussion of the Cardiff Model will be found in the following section.

## 4.4 CARDIFF DWLUT MODEL

Direct wave look-up table (DWLUT) model was introduced in [10], this model allowed large-signal data to be used directly in CAD simulators for power amplifier (PA) design. Subsequently, the model was developed based on the PHD model to form a new equation with its coefficients extracted from the measurement data [11-19].

### 4.4.1 EXTRACTION CARDIFF DWLUT MODEL

DWLUT employs the admittance domain to link the extrinsic measured voltage and current waveforms [12, 20]. Figure 4-5 depicted this method, which was verified with a 100 W LDMOS device.



Figure 4-5: Generic block diagram of DWLUT.

In the above figure, the  $V_{IN}(\omega)$  and  $V_{OUT}(\omega)$  are the voltage applied to the system and responses by the  $I_1(\omega)$  and  $I_2(\omega)$ .

$$I_1(\omega) = A_0 \cdot \delta(\omega) + \sum_{n=1}^m A_n \cdot V_{IN}^n \cdot \delta(\omega - 2\pi \cdot n \cdot f_0) \quad (4-7)$$

$$I_2(\omega) = B_0 \cdot \delta(\omega) + \sum_{n=1}^m B_n \cdot V_{IN}^n \cdot \delta(\omega - 2\pi \cdot n \cdot f_0) \quad (4-8)$$

Equations (4-7) and (4-8) define the current response voltage input,  $n$  is the number of harmonics, and  $f_0$  is the fundamental frequency while  $A_N$  and  $B_N$  in (4-9) and (4-10) are the DC components, they are functions of the DC biasing, gamma load, and a stimulus voltage at the input port [10].

$$A_N = \frac{I_1(nf_0)}{V_{IN}^n(nf_0)} = F_1(|V_{IN}|, \Gamma_{Load}, V_{DC IN}, V_{DC OUT}) \quad (4-9)$$

$$B_N = \frac{I_2(nf_0)}{V_{IN}^n(nf_0)} = F_2(|V_{IN}|, \Gamma_{Load}, V_{DC IN}, V_{DC OUT}) \quad (4-10)$$

The above coefficients are calculated based on the measured data and saved in a data table. Hence, it enables the CAD simulator to look up the table based on a specific voltage input, output and bias condition to calculate the output current. It is worth mentioning that resultant data are formulated as a voltage, and current waves rather than a & b waves, wherein the implementation in CAD was based on a frequency domain device (FDD) because it is the Fourier coefficients of the voltage and currents that are operated upon, not the time domain waveforms directly [10].

Despite this approach succeeding in importing the measured data into the CAD simulator, it imposes a dilemma in a modelling solution, because it gives inaccurate results when extrapolating outside the measurement space. Also, having a large set of measured data is crucial for obtaining an accurate model which consumes time, and the

measurement speed gets slow. Therefore, the action was needed to overcome the above limitations and improve the way the Cardiff model coefficients are extracted from measurement data. Ideally, an approach that would provide for the direct extraction of model coefficients from measured data is desired. The next section details the required equations for model extraction.

#### **4.5 CARDIFF BEHAVIOURAL MODEL**

As stated earlier, the behavioural model-based data lookup table has shown limitations where the model prediction works fine, but it fails to cover the design measurement space. From the design point of view, it is difficult to restrict the applied settings such as bias, input voltage, frequency and load-impedance, to specific values as located on the measurement grid. Undoubtedly, having interpolation and extrapolation off the measurement grid in CAD simulator is required. As a result, an alternative solution was originated by utilising the behavioural model-based polynomial in RF V-I measurement data that is called Cardiff behavioural model. It is based on the measured time domain waveforms and was first presented by Qi [\[12\]](#) and Woodington [\[21\]](#). The next section will detail the general formulation of Cardiff behavioural model; then the required steps needed to move from phase domain to the frequency domain for model identification and extraction.

---

### 4.5.1 THE GENERAL FORMULATION OF THE CARDIFF MODEL

The purpose of this section is to revisit the general formulation of the Cardiff behavioural model which is based on phase polynomials only. It starts with explaining the definition of the Cardiff Model equations for one tone (phase domain), then guides the reader to exploit these equations for two-tone measurements for model identification in the frequency domain.

#### 4.5.1.1 BACKGROUND

The Cardiff Model is usually defined in terms of a travelling wave, where the resultant b-waves are a function of the stimuli a-waves  $a_{p,h}$ .

$$b_{p,h} = f(a_{1,h}, a_{2,h}) \quad (4-11)$$

The subscripts 'p' and 'h' in (4-11) refers to the port number, and harmonic index, respectively. This can be re-written to highlight that the output b-waves are a function of the magnitude and phase of the input a-waves:

$$b_{p,h} = f(|a_{1,h}|, p_h, |a_{2,h}|, Q_h) \quad (4-12)$$

Where  $p_h = \frac{a_{1h}}{|a_{1h}|}$  and  $Q_h = \frac{a_{2h}}{|a_{2h}|}$

Equation (4-12) is considered a general formulation for multiple harmonics. For a fundamental load-pull only, the harmonic can be specified to harmonic index =1.

$$b_{p,1} = f (|a_{1,1}|, P_1, |a_{2,1}|, Q_1 ) \quad (4-13)$$

The Cardiff behavioural model based on the relative phase where the phase should be normalised to the  $a_{11}$ .

$$\frac{b_{p,1}}{p_1} = f \left( |a_{1,1}|, |a_{2,1}|, \frac{Q_1}{P_1} \right) \quad (4-14)$$

Equation (4-14) represents the phase transformation from absolute phase to a relative phase where the fundamental input phase  $p_1$  was used as a reference. After normalising the phase to  $a_{11}$ , the equation (4-14) can be rewritten as follow;

$$b_{n,h} = P_1^h \cdot k_{n,h} \left( |a_{11}|, |a_{21}|, \left( \frac{Q}{P} \right) \right) \quad (4-15)$$

Equation (4-15) shows that the phase can be measured independently of magnitudes. Analysing a non-linear system in terms of signal mixing show that the phase terms can be expanded as powers of relative phase. A set of coefficients can be utilised for different N orders of phase non-linearity to be described as shown in equation (4-16) [21].

$$b_{p,h} = P_1^h \sum_{n=-(N-1)/2}^{n=+(N-1)/2} \left\{ k_{p,h,n} |a_{11}|, |a_{21}| \left( \frac{Q_1}{P_1} \right)^n \right\}. \quad (4-16)$$

$$P_1 = \angle \frac{a_{11}}{|a_{11}|} \text{ and } Q_1 = \angle \frac{a_{21}}{|a_{21}|}$$

The 'p' and 'h' subscripts denote the respective port and harmonic, and the 'n' denotes to the phase exponent. The above equation is similar to the X-parameters if the coefficients are limited to three, such as  $K_{2,1,0}$ ,  $K_{2,1,1}$  and  $K_{2,1,-1}$ . For fundamental CW load-pull measurements in eq. (4-16), determination of the coefficients  $K(n, h, m)$  requires measurements at constant  $|a_{11}|$  and  $|a_{21}|$  while sweeping the relative phase components  $\left( \frac{Q}{P} \right)$ .

In the meantime, it has been shown that to model non-linear fundamental load-pull contours needs higher order, possibly up to 9<sup>th</sup> order to correctly predict the measured behaviour, resulting in more a complex model that is more time consuming to measure.

The resultant mixing term from the above equation imposes a dilemma, as there is difficulty in identifying the correct number of coefficients and the model order. Hence, the model might be under or overdetermined.

### 4.5.2 FROM CW TO TWO-TONE STIMULUS

Recall the definition of Cardiff behavioral model for CW measurements is given below:

$$b_{p,h} = P_1^h \sum_{n=-(N-1)/2}^{n=+(N-1)/2} \left\{ k_{p,h,n} |a_{11}|, |a_{21}| \left( \frac{Q_1}{P_1} \right)^n \right\} \quad (4-17)$$

In (4-17),  $N$  defines the model complexity. To limit the polynomial to 5<sup>th</sup> order,  $N$  was set to 5, thus extracted model coefficients are shown below:

$$b_{21} = P \left( K_{21,-2} |a_{21}|^1 \left( \frac{Q}{P} \right)^{-2} + K_{21,2} |a_{21}|^1 \left( \frac{Q}{P} \right)^2 + \right. \quad (4-18)$$

$$\left. K_{21,-1} |a_{21}|^1 \left( \frac{Q}{P} \right)^{-1} + K_{21,0} |a_{21}|^0 \left( \frac{Q}{P} \right)^0 + K_{21,1} |a_{21}|^1 \left( \frac{Q}{P} \right)^1 \right)$$

Substitute into eq. (4-18) the stimulus signals allows the interaction between the injected signals and the IMD products in term of magnitude and phase to be identified:

$$b_{21} = K_{21,-2} (a_{21}^*)^2 \frac{a_{11}^3}{|a_{11}|^3} + K_{21,2} (a_{21})^2 \frac{a_{11}^*}{|a_{11}|} + K_{21,-1} a_{21}^* \frac{a_{11}^2}{|a_{11}|^2} + \quad (4-19)$$

$$K_{21,0} \frac{a_{11}}{|a_{11}|} + K_{21,1} a_{21}$$

$$b_{21} = \frac{K_{21,-2}}{|a_{11}|^3} (a_{21}^*)^2 a_{11}^3 + \frac{K_{21,2}}{|a_{11}|} (a_{21})^2 a_{11}^* + \frac{K_{21,-1}}{|a_{11}|^2} a_{21}^* a_{11}^2 + \quad (4-20)$$

$$\frac{K_{21,0}}{|a_{11}|} a_{11} + K_{21,1} a_{21}$$

Where:

$$\begin{aligned}
 a_{11} &= \rho_{11} \left\{ \frac{e^{j\omega t} + e^{-j\omega t}}{2} \right\} \\
 a_{21} &= \rho_{21} \left\{ \frac{e^{j\omega t + \varphi_{21}} + e^{-j\omega t - \varphi_{21}}}{2} \right\}
 \end{aligned} \tag{4-21}$$

Signal  $a_{11}$  was injected into Port 1 while Signal  $a_{21}$  was injected into Port 2. For fundamental CW Load-Pull,  $\omega_1 = \omega_2 = \omega$ . Hence, the  $b_2$  response of the system is a function of the magnitude  $\rho_{21}$  and phase  $\varphi_{21}$  where these values are typically set on a user defined fixed grid. In this case, traditional load-pull measurement sequence, the model complexity is difficult to identify.

To enable model coefficient identification the  $a_{21}$  variation as a function of time needs to be carefully chosen. Consider, now a time varying load-pull signal  $a_{21}(t)$  using two-tone stimulus is produced here.

$$a_{21}(t) = \frac{a_{21}^E(t)e^{j\omega t} + a_{21}^{E*}(t)e^{-j\omega t}}{2} \tag{4-22}$$

The envelop excitation signal consists of  $a_{21}^0$  which defines the reference impedance about which the load-pull is performed and a variable component  $\Delta a_{21}$  that performs the load-pull. Here, the two-tone stimulus is defined as follow:

$$a_{21}^E = a_{21}^0 + \Delta a_{21} \tag{4-23}$$

To implement a time varying signal, the amplitude and the phase of  $\Delta a_{21}$  was varied as a function of time.

$$\Delta a_{21}(t) = \rho_{21}(t) e^{j\phi_{21}(t)} \quad (4-24)$$

Where the phase component is defined as follow:

$$e^{j\phi_{21}(t)} = \cos(\omega_p t) + j \sin(\omega_p t) \quad (4-25)$$

And the magnitude component equals to:

$$\rho_{21}(t) = \rho_{21}^0 (1 + \cos(\omega_a t)) \quad (4-26)$$

Recall eq. (4-20) for CW excitation signal, consider now applying the two-tone stimulus, which results a new equation in complex form as follow:

$$\begin{aligned} b_{21} = & \frac{K_{21,-2}}{|a_{11}|^3} \frac{1}{2} a_{21}^E * 2 \frac{1}{4} a_{11}^E 3 \left\{ \frac{e^{-j2\omega_2 t} + e^{j2\omega_2 t} + 2}{2} \right\} \left\{ \frac{e^{j3\omega_1 t} + e^{-j3\omega_1 t}}{4} - \right. \quad (4-27) \\ & \left. 3 \frac{e^{j\omega_1 t} + e^{-j\omega_1 t}}{4} \right\} + \\ & \frac{K_{21,2}}{|a_{11}|} \frac{1}{2} a_{21}^E 2 a_{11}^E * \left\{ \frac{e^{j2\omega_2 t} + e^{-j2\omega_2 t} + 2}{2} \right\} \left\{ \frac{e^{-j\omega_1 t} + e^{j\omega_1 t}}{2} \right\} + \\ & \frac{K_{21,-1}}{|a_{11}|^2} a_{21}^E * \frac{1}{2} a_{11}^E 2 \left\{ \frac{e^{-j\omega_2 t} + e^{j\omega_2 t}}{2} \right\} \left\{ \frac{e^{j2\omega_1 t} + e^{-j2\omega_1 t} + 2}{2} \right\} + \\ & \frac{K_{21,0}}{|a_{11}|} a_{11} \left\{ \frac{e^{j\omega_1 t} + e^{-j\omega_1 t}}{2} \right\} + K_{21,1} a_{21} \left\{ \frac{e^{j\omega_2 t} + e^{-j\omega_2 t}}{2} \right\} \end{aligned}$$

To understand the above equation, a mixing term  $a_{21}^{E,2} a_{11}^{E,*}$  was selected as an example;

$$= a_{21}^{E,2} a_{11}^{E,*} \left( \frac{e^{j\omega_2 t} + e^{-j\omega_2 t}}{2} \right)^2 \left( \frac{e^{j\omega_1 t} + e^{-j\omega_1 t}}{2} \right)^{-1} \quad (4-28)$$

$$= \frac{1}{2} a_{21}^{E,2} a_{11}^{E,*} \left( \frac{e^{j2\omega_2 t} + e^{-j2\omega_2 t} + 2}{2} \right) \left( \frac{e^{-j\omega_1 t} + e^{j\omega_1 t}}{2} \right) \quad (4-29)$$

$a_{11}^{E}$  was kept at fixed drive power level, which is not being considered in modelling the device. This allows to be removed from the equation for further simplification. Consider the new equation with trigonometric form:

$$= \frac{1}{2} a_{21}^{E,2} \left( \frac{e^{j2\omega_2 t} + e^{-j2\omega_2 t} + 2}{2} \right) = \left[ \frac{1}{2} \cos(2\omega_2) + \frac{1}{2} \right] \quad (4-30)$$

Equation (4-30) shows the mixing term is being found at Dc and second harmonic phase grid ( $2\omega_p$ ) as shown in Figure 4-7.

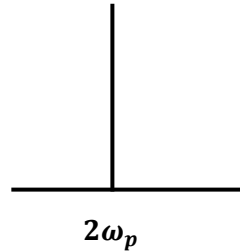


Figure 4-7: Phase spectral component of mixing term  $K_{21,2}$ .

This way, all the mixing terms above the noise floor can be observed using a spectral domain.

The idea of varying the phase has been looked at by Woodington et al. in [21]. In this work, the load-pull measurements are done by stepping the phase of  $a_{21}$  ( $\angle a_{21}$ ) from  $0^\circ$  to  $360^\circ$  while keeping the  $|a_{21}|$  fixed. Figure 4-8 shows a passive tuner was used to normalise the measurement to the optimum load. Consequently, the hybrid system generated a set of  $a_{21}$  in the form of concentric circles in the Smith Chart about this optimum.

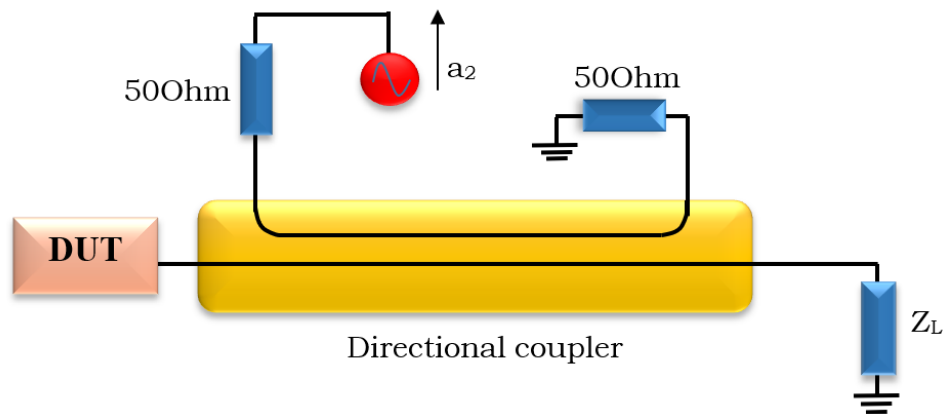


Figure 4-8 : An integrating active source to the passive load-pull system to generate a required load-pull annulus.

However, due to hardware limitations, at the time, it was difficult to implement modulated measurements, the author replicated this measurement sequence by doing time step amplitude and time step phase that needs a lot of time trying to get the best measurements. It was required to implement around hundreds of load-pull measurements and put them together to basically mimic what would happen if the modulated measurement system exists, which is considered very complicated measurements because this data must be

perfect phase grid to Fourier Transform it. It was, thus, considered at the time, not to be a practically viable measurement approach to be used for robust model extraction. However, it did successfully demonstrate the feasibility and usefulness of the concept.

Since the difficulty to get the data on a perfect grid, the author has switched to using Least Square algorithm to extract model elements, removing the need to any structure of the data.

These limitations can now be addressed using high-speed measurement systems based on PXIe modules [22] which can allow for load-pull measurements using multi-tone stimuli with a dynamic range more than 80dB [23]. So, with an appropriate stimulus, these systems can be used to aid in the model identification process.

As mentioned earlier, the previous approach was useful for identifying the phase mixing terms. For identifying the magnitude and phase mixing terms together, the amplitude phase modulation novel approach was utilised to differentiate these terms as the magnitude mixing terms are superimposed on phase mixing terms. Consider combining equations (4-24) to (4-26) to produce:

$$\Delta A_{2,1}^E(t) = \frac{A_{2,1}^A}{2} [(1 + \text{COS}(s_a \omega t)) (\text{COS}(s_p \omega t) + j \text{SIN}(s_p \omega t))] \quad (4-31)$$

$$\Delta A_{2,1}^E(t) = \frac{A_{2,1}^A}{2} (\cos(s_p \omega t) + j \sin(s_p \omega t) + \cos(s_a \omega t) \cos(s_p \omega t) + \cos(s_a \omega t) j \sin(s_p \omega t)) \quad (4-32)$$

Please note:

$$\cos(s_a \omega t) \cos(s_p \omega t) = \frac{1}{2} \cos(s_p \omega t - s_a \omega t) + \frac{1}{2} \cos(s_p \omega t + s_a \omega t) \quad (4-33)$$

$$\cos(s_a \omega t) \sin(s_p \omega t) = \frac{1}{2} \sin(s_p \omega t + s_a \omega t) + \frac{1}{2} \sin(s_p \omega t - s_a \omega t)$$

This leads to:

$$\Delta A_{2,1}^E(t) = \frac{A_{2,1}^A}{2} \left( (\cos(s_p \omega t) + j \sin(s_p \omega t) + \frac{1}{2} \cos(s_p \omega t - s_a \omega t) + \frac{1}{2} \cos(s_p \omega t + s_a \omega t) + \frac{1}{2} \sin(s_p \omega t + s_a \omega t) + \frac{1}{2} \sin(s_p \omega t - s_a \omega t)) \right) \quad (4-34)$$

$$\Delta A_{2,1}^E(t) = \frac{A_{2,1}^A}{2} (\cos(s_p \omega t) + j \sin(s_p \omega t) + \frac{1}{2} [\cos(s_p \omega t - s_a \omega t) + \sin(s_p \omega t - s_a \omega t)] + \frac{1}{2} [\cos(s_p \omega t + s_a \omega t) + \sin(s_p \omega t + s_a \omega t)]) \quad (4-35)$$

The spectral domain of eq. (4-35) is shown below

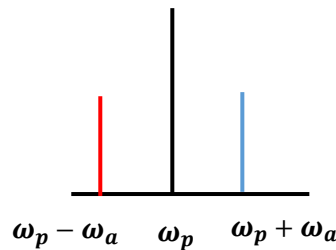


Figure 4-10: Magnitude and phase spectral components of  $\Delta A_{2,1}^E$

After developing a modulated measurement system, the capability to regenerate this data in time domain and utilise Least Mean Squares (LMS) algorithm for model extraction becomes an easy approach to implement. Eq. (4-36)-(4-38) show that once the desired model complexity is chosen, the model formulation can be re-written in a matrix form. The matrix  $[A]$  elements are quantified by the chosen model complexity. The main condition to be applied in the LMS algorithm is to have a smaller number of coefficients than the measured data. Otherwise, the algorithm would not converge as more unknown quantities would exist than the known quantities.

$$[B] = [X][A] \quad (4-36)$$

$$[A]^H \cdot [B] = [X] \cdot [A][A]^H \quad (4-37)$$

$$[X] = ([A][A]^H)^{-1} \cdot [A]^H \cdot [B] \quad (4-38)$$

Alternatively, as  $\Delta a_{21}(t)$  is a function of time, FFT can then be used to observe the spectrum, which gives a chance to look at the model terms and where the model terms are built from? As an example, to build up the  $\Delta a_{21}(t)^*$  (so called mixing term  $M_{1,-1}$ ), take eq. (4-24) and conjugate it. Now how it looks like in frequency domain and how the model coefficient transforms themselves into different spectral lines. Similarly, if we want to obtain  $|\Delta a_{21}(t)|^2$  (called  $M_{2,0}$ ); the mixing term  $\Delta a_{21}(t)$  should be multiplied by  $\Delta a_{21}(t)^*$  (see Figure 4-11). In the same way, looking at each model term individually and be transformed to form the  $b_2$  wave.

The realised Fourier Transform of b-signal can now identify the model complexity and directly extract the model terms which can then lead to alternative matrix structure in frequency domain that obviously becomes a diagonal matrix. This is considered a first time to be able directly extract the Cardiff model from load-pull measurements without using curve fitting algorithm.

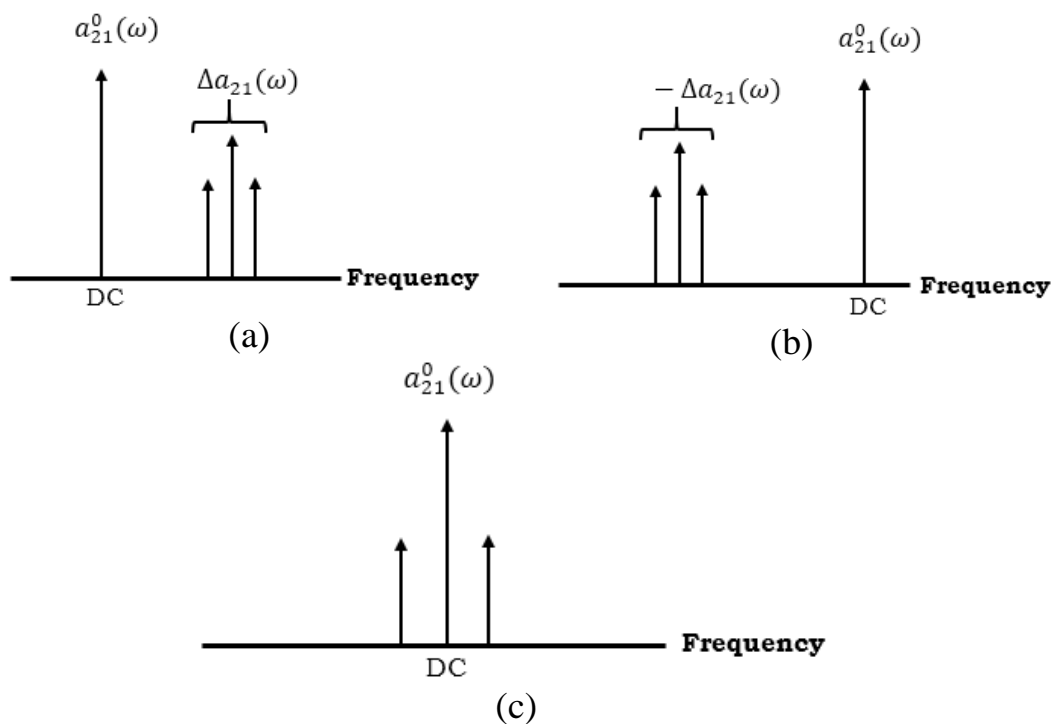


Figure 4-11: Spectral lines of  $a_{21}^E$  stimulus

(a) Before the conjugate ( $M_{1,1}$ )      (b) After the conjugate ( $M_{1,-1}$ )

(c)  $M_{2,0}$  mixing term

The next chapter will be concentrating on the model the complexity identification concept to include both magnitude and phase related mixing terms. This is done through engineering a multi-tone stimulus, involving a carrier phase and amplitude modulation components.

## 4.6 CHAPTER SUMMARY

This chapter provides an overview of several non-linear behavioural model approaches that currently exist. Starting from PHD model which is considered the basis of the modelling and its limitation of assuming the  $a_{11}$  is the only large-signal dominant in the measurements while other waves are relatively small. Having said that, most modern behavioural modelling approaches are based upon this theory for instance, X-parameters with PNA-X solution to be utilised in load-dependent X-parameters measurements. This allows the X-parameters to cover a large area of the Smith Chart and not restricted to the area close to 50 Ohm.

The DWLUT model is a table based behavioural model; such a model was only useful for importing the non-linear data into the CAD simulation. The main downside was that it was only useful for predicting the measurements on which the model was based. Thus, it requires measurement data to be placed on a regular grid. It relies on CAD capability for a mathematical calculation of interpolation and extrapolation of data points. Results indicated that assuming a reasonably dense measurement grid is selected the CAD can be trusted to interpolation robustly between measured points while the extrapolation is limited.

---

---

The development of this approach led to the development of the Cardiff Model, which is a polynomial based modelling approach. The Cardiff behavioural model utilises a formulation based on summing mixing terms to provide a global load-pull model. Therefore, it can be used to cover a substantial area in the Smith Chart during the load-pull measurement. Also, this solution was useful to tackle the limitation of the previous modelling approach (DWLUT), exploiting the LMS algorithm for extracting the required coefficients allows the measurement data to be no longer be placed on a regular grid.

Having an accurate model requires the model order and the number of coefficients to be known, in advance, to avoid overfitting the model. Model complexity is difficult to identify from traditional CW load-pull measurements. Both the  $a_{11}$  and  $a_{21}$  have the same frequency input so the impact of mixing cannot be seen in the raw data. Previously, this was addressed by targeting load-pull measurements points to be on a special phase grid. This is difficult to accurately achieve, however using the multi-tone measurement system developed in this thesis this approach can now be revisited. Hence, a new technique of identifying and extracting Cardiff Model coefficients is detailed in the next chapter.

---

## REFERENCES

1. Root, D., *Polyharmonic distortion modeling*. IEEE microwave magazine, 2006. **7**(3): p. 44-57.
2. Root, D.E., et al., Broad-band poly-harmonic distortion (PHD) behavioral models from fast automated simulations and large-signal vectorial network measurements. IEEE Transactions on Microwave Theory and Techniques, 2005. **53**(11): p. 3656-3664.
3. Verbeyst, J.V.a.M.v.B.a.F., Characterizing Components Under Large Signal Excitation: Defining Sensible "Large Signal S-Parameters". **31**: p. 109-117.
4. Verspecht, J., Describing Functions Can Better Model Hard Nonlinearities In The Frequency Domain Than The Volterra Theory. 1995.
5. Zhang, Q. and S. Liang. Comparative study of X-parameters and nonlinear scattering functions. in IEEE 2011 10th International Conference on Electronic Measurement & Instruments. 2011.
6. Root, D.E., et al. Compact and behavioral modeling of transistors from NVNA measurements: New flows and future trends. in Proceedings of the IEEE 2012 Custom Integrated Circuits Conference. 2012.
7. Simpson, G., et al. Load-pull + NVNA = enhanced X-parameters for PA designs with high mismatch and technology-independent large-signal device models. in 2008 72nd ARFTG Microwave Measurement Symposium. 2008.
8. Verspecht, J., et al. Broad-band, multi-harmonic frequency domain behavioral models from automated large-signal vectorial network measurements. in IEEE MTT-S International Microwave Symposium Digest, 2005. 2005.
9. Verspecht, J., et al. Extension of X-parameters to include long-term dynamic memory effects. in 2009 IEEE MTT-S International Microwave Symposium Digest. 2009.
10. Qi, H., J. Benedikt, and P. Tasker. A Novel Approach for Effective Import of Nonlinear Device Characteristics into CAD for Large Signal Power Amplifier Design. in 2006 IEEE MTT-S International Microwave Symposium Digest. 2006.
11. Qi, H., J. Benedikt, and P.J. Tasker. Novel Nonlinear Model for Rapid Waveform-based Extraction Enabling Accurate High Power PA Design. in 2007 IEEE/MTT-S International Microwave Symposium. 2007.

12. Qi, H., J. Benedikt, and P.J. Tasker, *Nonlinear Data Utilization: From Direct Data Lookup to Behavioral Modeling*. IEEE Transactions on Microwave Theory and Techniques, 2009. **57**(6): p. 1425-1432.
13. Qi, H., *Nonlinear Data Utilization: Direct Data Look-up to Behavioural Modelling*. Ann Arbor, 2008. **1050**: p. 48106-1346.
14. Woodington, S., et al. A novel measurement based method enabling rapid extraction of a RF Waveform Look-Up table based behavioral model. in 2008 IEEE MTT-S International Microwave Symposium Digest. 2008.
15. Woodington, S., et al. Behavioral model analysis of active harmonic load-pull measurements. in 2010 IEEE MTT-S International Microwave Symposium. 2010.
16. Tasker, P.J. and J. Benedikt, *Waveform Inspired Models and the Harmonic Balance Emulator*. IEEE Microwave Magazine, 2011. **12**(2): p. 38-54.
17. Bell, J.J., et al. Behavioral model analysis using simultaneous active fundamental load-pull and harmonic source-pull measurements at X-band. in 2011 IEEE MTT-S International Microwave Symposium. 2011.
18. Bell, J.J.W., et al. X-band behavioral model analysis using an active harmonic source- pull and load-pull measurement system. in Asia-Pacific Microwave Conference 2011. 2011.
19. Bell, J.J., *Input Harmonic and Mixing Behavioural Model Analysis*. 2014, Cardiff University.
20. Qi, H., J. Benedikt, and P. Tasker. Direct extraction of large-signal table-based behavioural models from time-domain voltage and current waveforms. in High Frequency Postgraduate Student Colloquium, 2005. 2005.
21. Woodington, S., et al. A novel measurement based method enabling rapid extraction of a RF waveform look-up table based behavioral model. in Microwave Symposium Digest, 2008 IEEE MTT-S International. 2008. IEEE.
22. Hussein, T., et al. Automating the Accurate Extraction and Verification of the Cardiff Model via the Direct Measurement of Load-Pull Power Contours. in 2018 IEEE/MTT-S International Microwave Symposium-IMS. 2018. IEEE.
23. Al-Rawachy, A., et al. Cardiff Behavioural Model Analysis using a Two-Tone Stimulus. in 2019 IEEE Topical Conference on RF/Microwave Power Amplifiers for Radio and Wireless Applications (PAWR). 2019.

# CHAPTER 5

## MULTI-TONE EXCITATION FOR MODEL

### EXTRACTION IN ACTIVE LOAD-PULL

#### 5.1 INTRODUCTION

The Cardiff Model exploits the property that when multiple stimuli are injected into a multi-port nonlinear system, they interact or 'mix'. The Cardiff Model is defined in the frequency domain and when correctly implemented, should include all the resulting frequency components. Hence, the Cardiff Model differentiates itself from other popular behavioural modelling formulations, S-parameters, PHD modelling [1, 2] and X-parameters [3], by not limiting the number of model coefficients that can be extracted; for instance, two coefficients for S-parameters and three for analytical X-parameters and PHD modelling. This approach allows for a global model fit of data, obtained by executing impedance sweeps over an area of the Smith Chart, rather than a local fit about/at each impedance point of the sweep. Previous work in [4] [5] has verified the Cardiff Model coefficient structure so that global models of harmonic source and load-pull data can be accurately extracted with attempts at avoiding over-fitting the data.

This chapter demonstrates two main aspects; the first part revisits a technique for determining the correct, and present, phase polynomial coefficients of the Cardiff Model using two-tone stimulus. The second part extends this model complexity identification concept to include both magnitude and phase related mixing terms using specifically engineered multi-tone stimuli.

## **5.2 MODEL IDENTIFICATION FOR TWO-TONE STIMULUS (PHASE POLYNOMIAL ONLY)**

The first technique utilises two-tone measurements and the Fast Fourier Transform (FFT) to be able to observe the mixing order and resultant intermodulation (IMD) products above the noise floor. This allows moving from the phase domain to the frequency domain for direct and accurate determination of the maximum number of model phase coefficients used in the Cardiff Model.

To ensure that the data design is relevant, the main-tone impedance was located at the DUTs optimum power point on the Smith Chart using the algorithm in [7] to track the optimum load of the maximum output power for the 10W GaN device (CGH40010F). In principle, tracking the optimum output power in eq. (5-1) is based upon a successive set of load-pull measurements, starting at the 50 Ohm area

and stopping when it reaches the target (finding the maximum output power).

$$P_{out} = \frac{|b_{p,h}|^2 - |a_{p,h}|^2}{2} \quad (5-1)$$

Equation (5-2), which can be found in [7], is a load-based behavioural model that uses the impedance target ( $\Gamma_{21}$ ) instead of the  $a_{21}$ , as previously published in [4] and [5]. As described in this equation, M is used to limit the model complexity while the  $K_{p,q}$  values are the extracted model coefficients. Letters D and C are the magnitude and phase exponents respectively.

$$b_{21} = \sum_{D=0}^{D=1} \sum_{C=-(M-D)}^{C=+(M-D+1)} K_{|C|+2D,C} |\Gamma_{21}|^{|C|+2D} \left( \frac{\Gamma_{21}}{|\Gamma_{21}|} \right)^C \quad (5-2)$$

After finding the optimum load, the load was perturbed by the second output phase modulated tone  $a_{21,2}$  (see Figure 5-1). The magnitude of  $|a_{21,2}|$  was kept constant while sweeping the phase from  $0^\circ$  to  $360^\circ$ . This approach was repeated seven times by varying the  $|a_{21,2}|$  from -6dBc to +6dBc of the main-tone signal magnitude  $|a_{21,1}|$ . Consequently,  $b_{21}$ , the device's response of each of the  $|a_{21,1}|$  magnitudes, can be easily observed. The phase-modulated signal  $|a_{21,2}|$  creates a linear circle perturbation during the load-pull measurements at each level input. However, this will generate growing levels of observable distortion in the b-wave response, and hence identify the growing model complexity and load modulation coverage of the Smith Chart is increased. This

method gives an approach to investigate the presence of the model terms and their relation to the IMD spectra at different power levels of  $|a_{21,2}|$ .

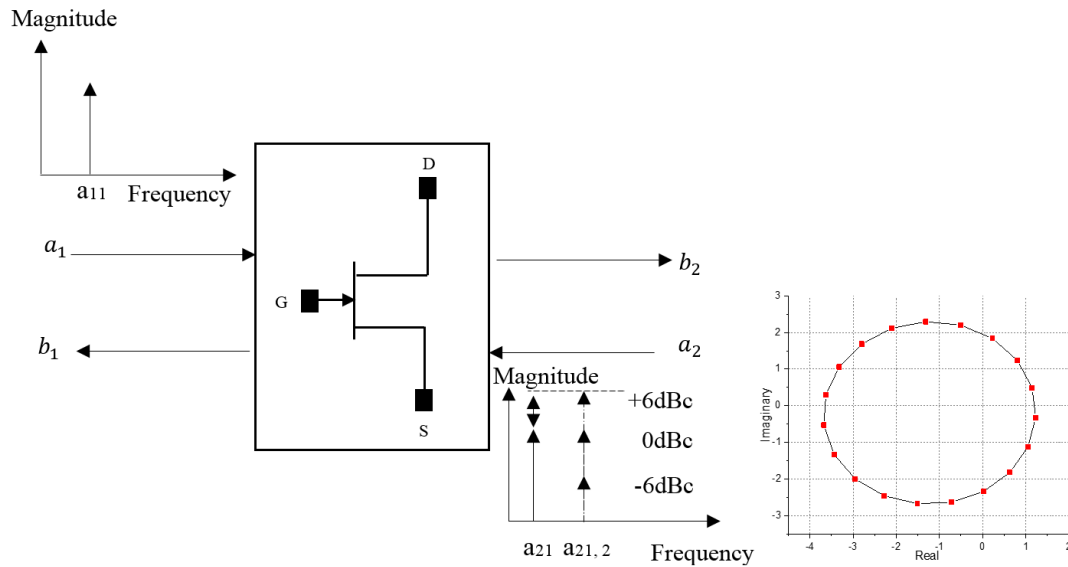


Figure 5-1: Simplified diagram of the stimulus waves.

In order to analyse the received, downconverted spectra, the selected tones in the receiver bandwidth needed to be calibrated and phase-normalized to the input travelling-wave ( $a_{11}$ ) at the main tone frequency (1 GHz). This established a relative phase system, the key for behavioural modelling and analysis [1-5]. The raw, downconverted IMD tones lie on a harmonic grid ( $\pm n \cdot 1$  kHz) and were compared to a proposed noise floor of -85dBm for selection before calibration. Using the IFFT, the time-domain travelling-wave quantities were then constructed from the selected tones. This allowed for b-wave analysis and load modulation coverage to be observed on the Smith Chart. All noise tones were removed in this process.

During extraction and verification of the model, the a-wave based Cardiff behavioural Model is used. This is the a-wave based model format, which is compatible with CAD tools. The formulation is described in the below equation:

$$\frac{b_{21}}{P} = \sum_{D=0}^{D=1} \sum_{C=-(M-D)}^{C=+(M-D+1)} K_{|C|+2D,C} |a_{21}|^{|C|+2D} \left(\frac{Q}{P}\right)^C \quad (5-3)$$

Once more, the user-defined parameter M expresses the model mixing order, C and D are the phase and magnitude exponents respectively while  $K_{pq}$  are the extracted model coefficients.

Figure 5-2 shows the resultant  $b_{21E}$  (the b-envelope about the fundamental tone) DUT response to the injection of a  $|a_{21,2}|$  phase modulated signal = -6dBc. As previously stated, it was difficult, in advance, to predict the model order and mixing terms during model extraction. However, in this case, the model complexity can be identified by looking at the spectral response of the time varying b-wave signals. Therefore, exploiting the FFT allows the observation of spectral tones above the noise floor that are a consequence of the device's nonlinearity.

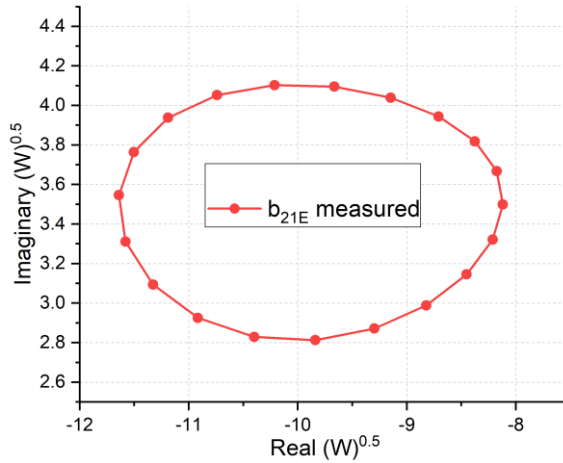


Figure 5-2: Resultant  $b_{21E}$  of the device response for the  $|a_{21,2}| = -6\text{dBc}$ .

Figure 5-3 depicts the downconverted  $|b_{21E}|$  the spectral plot, for  $|a_{21,2}| = -6\text{dBc}$ , and links the observable tones, above the noise floor, to Cardiff Model coefficients ( $K_{\text{ph},m,n}$ ). Overlaid, on the model tones is the associated model term contribution  $\left(K_{21,11} |a_{21E}| \left(\frac{Q}{P}\right)\right)$  after extracting the model for eq. (5-4). The almost exact overlap indicates the accuracy of the model formulation’s ability to fit the data.

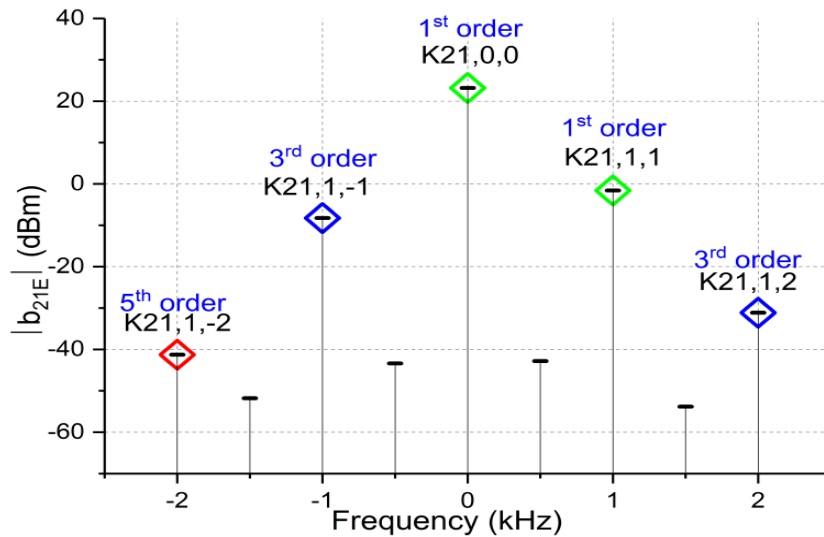


Figure 5-3:  $|b_{21E}|$  spectrum showing 5<sup>th</sup> order coefficients for  $|a_{21,2}| = -6\text{dBc}$ .

Equation (5-4) formulates the required Cardiff Model in this case based on the observations from the spectra in Figure 5-3, this is a relative phase polynomial only, as each annulus is taken at a fixed  $|a_{21}|$  injection and the relative phase is the only variable. Additionally, the first 3 coefficients ( $K_{21,0,0}, K_{21,1,1}, K_{21,1,-1}$ ) in the model are equivalent to the analytical X-parameters ( $X_F, X_S$  and  $X_T$ ).

It can be observed from Figure 5-3, that asymmetry is found between the tones where the offset amplitude between the phase modulated tone and the main tones exists. Therefore, the mixing term  $K_{21,1,3}$  (3<sup>rd</sup> order term) is not considered in (5-4) as it is below the noise floor.

$$\begin{aligned} \frac{b_{21}}{p} = & K_{(21,0,0)} + K_{(21,1,1)}|a_{21E}| \left(\frac{Q}{P}\right) + K_{(21,1,-1)}|a_{21E}| \left(\frac{Q}{P}\right)^{-1} + \\ & + K_{(21,1,2)}|a_{21E}| \left(\frac{Q}{P}\right)^2 + K_{(21,1,-2)}|a_{21E}| \left(\frac{Q}{P}\right)^{-2} \end{aligned} \quad (5-4)$$

In Figure 5-4, the comparison between  $b_{21E}$  model and measured data was performed for a different number of coefficients. As mentioned earlier, to fit the model and get an accurate result, the number of utilised coefficients should match the number of spectral lines above the noise floor in Figure 5-3. For the sake of clarity, different model orders were applied to check the functionality of the model. In (a) the model presents three coefficients only (analytical X-parameters) where the model does not fit well with the measured data while the model in (b) and (c) demonstrates how the model is able to capture the measured data.

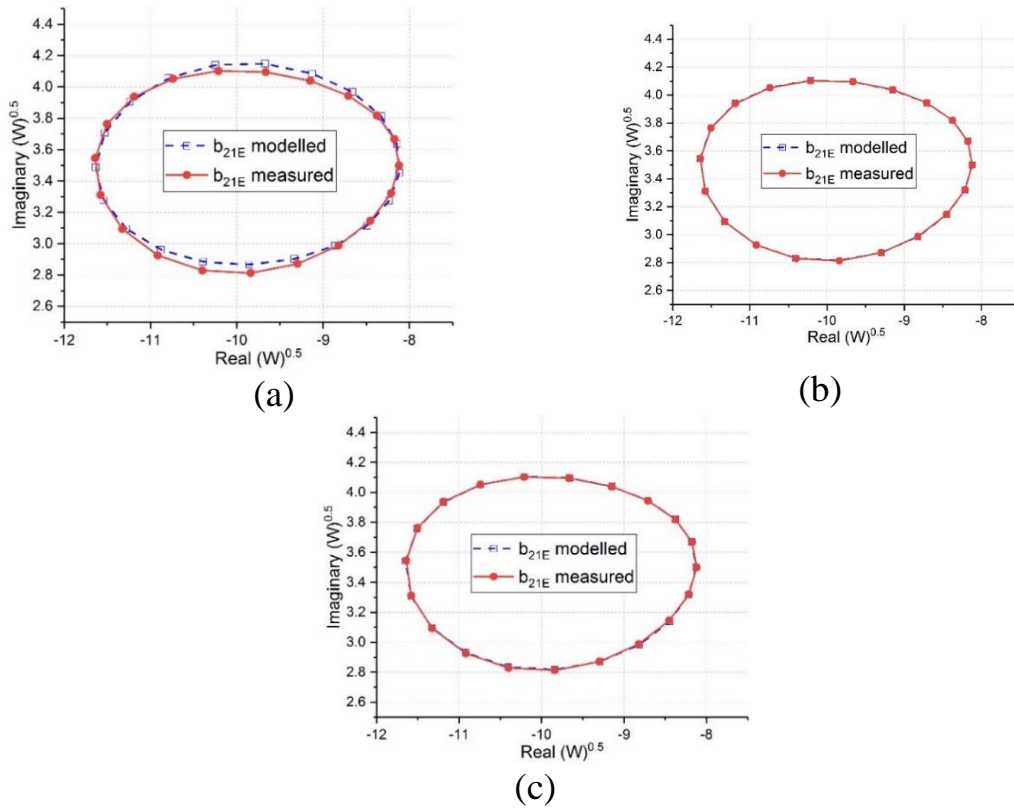


Figure 5-4:  $b_{21E}$  comparison for the selected coefficients for  $|a_{21,1}| = -6\text{dBc}$ .

(a) For 3 coefficients only (X-parameters).

(b) For 3<sup>rd</sup> order only. (c) For 5<sup>th</sup> order only.

It should be noted that although the term  $K_{21,1,-2}$  is not included in (b) but the model still accurate because of the term  $K_{21,1,-2}$  is just above the noise floor and its contribution to the model is negligible compared with other mixing terms. Table 5-1 shows the NMSE for different model orders to be linked with Figure 5-4.

Table 5-1: NMSE for different model orders.

Figure number	Mixing terms	NMSE (dB)
Figure 5-4 (a)	X-parameters	-54.09
Figure 5-4 (b)	3 <sup>rd</sup> order	-57.28
Figure 5-4 (c)	5 <sup>th</sup> order	-60.39

Figure 5-5 shows the resulting spectrum for  $|a_{21,1}| = 0\text{dBc}$  and indicates that a stronger mixing process are present then in Figure 5-3, which requires a commensurate model formulation (9<sup>th</sup> order) for accurate model extraction. Again, the overlaid extracted model term contributions map directly onto the spectral lines.

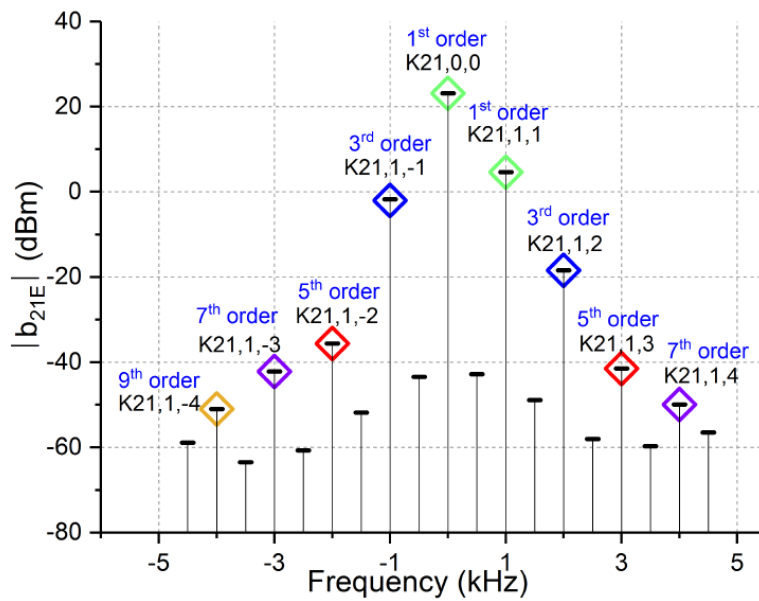


Figure 5-5:  $|b_{21E}|$  spectrum showing 9<sup>th</sup> order coefficients for  $|a_{21,1}| = 0\text{dBc}$ .

Figure 5-6 compares the  $b_{21E}$  a model with measured data as the model complexity is increased. It can be clearly seen that the 5<sup>th</sup> order model gives good accuracy while other model orders give small enhancement to the model fit, as the coefficients are just above the noise floor. Therefore, a trade-off between the model accuracy and model complexity exists, the higher the complexity of the model requires measurement with better accuracy, hence more time.

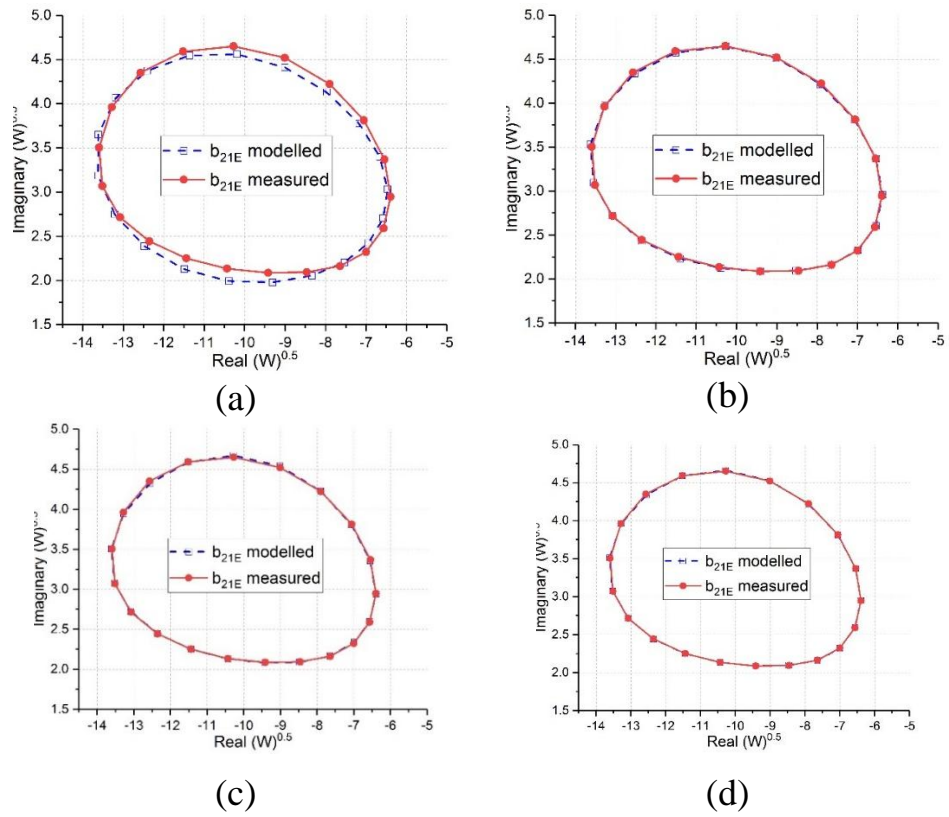


Figure 5-6:  $b_{21E}$  comparison for the selected coefficients for  $|a_{21,1}| = 0\text{dBc}$ .  
 (a) For 3 coefficients only (X-parameters). (b) For 3<sup>rd</sup> order only.  
 (c) For 5<sup>th</sup> order only. (d) For 9<sup>th</sup> order only.

Table 5-2 shows the NMSE for different mixing terms which are linked with Figure 5-6.

Table 5-2: NMSE for different model orders.

Figure number	Mixing terms	NMSE (dB)
Figure 5-6 (a)	X-parameters	-41.58
Figure 5-6 (b)	3 <sup>rd</sup> order	-53.13
Figure 5-6 (c)	5 <sup>th</sup> order	-61.98
Figure 5-6 (d)	9 <sup>th</sup> order	-72.37

The final measurement, where  $|a_{21,2}| = 6\text{dBc}$  of the main tone. This excitation covers a significant area of the Smith Chart. More spectral tones can be observed when the input power is increased. Figure 5-7 shows the resultant  $|b_{21E}|$  spectrum, from which the required Cardiff Model complexity can be identified and its relation to model accuracy clearly identified.

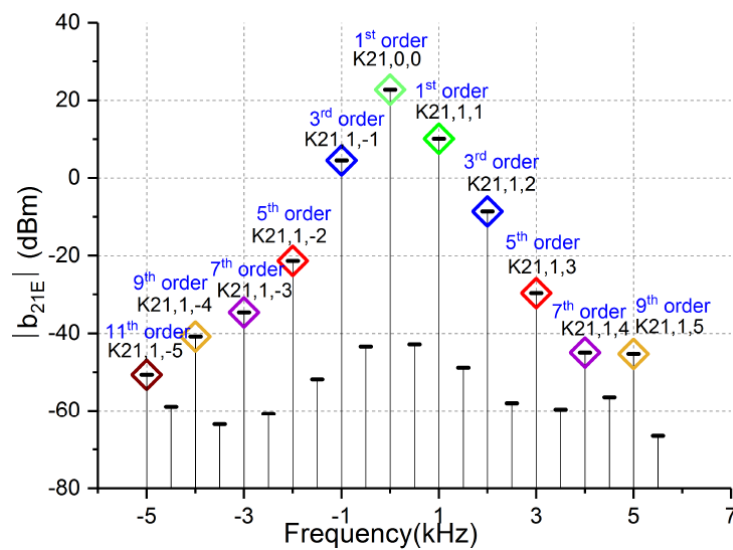


Figure 5-7:  $|b_{21E}|$  spectrum showing 11<sup>th</sup> order coefficients for  $|a_{21,2}| = 6\text{dBc}$ .

Figure 5-8 shows the comparison between model and measurement data for the full and truncated models. To demonstrate the inaccuracy that results from model truncation, the Cardiff Model orders, ranging from 3<sup>rd</sup> order to 11<sup>th</sup> order are plotted, in Figure 5-8, and compared to the measured data. For completeness, the 3-terms analytical X-parameter model is also included, and clearly shows a limitation of the analytical X-parameter model for this  $|a_{21,2}|$ . However, the Cardiff model formulation shows a gradual accuracy improvement when it includes further model coefficients to match the existing terms in the observed spectrum.

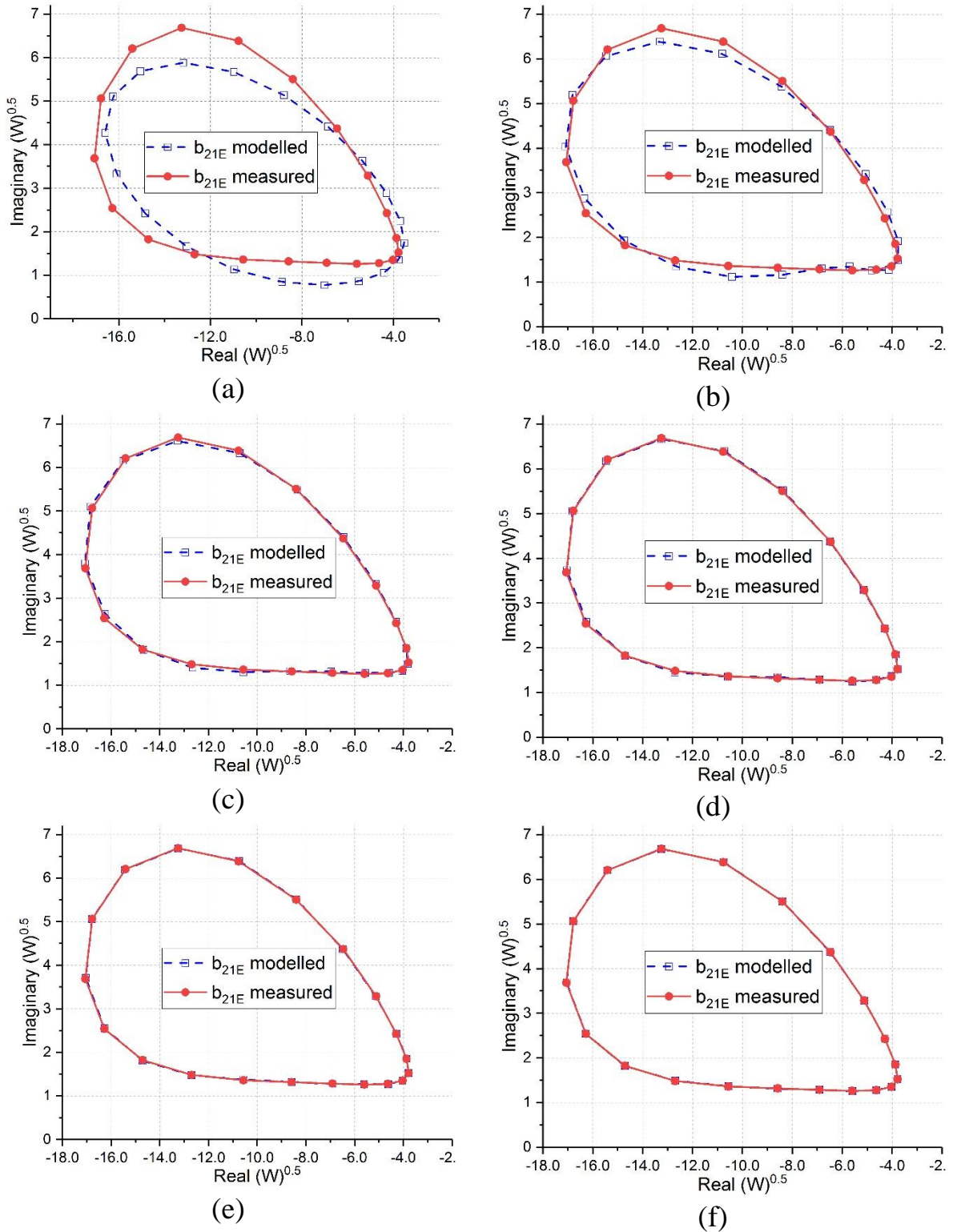


Figure 5-8:  $b_{21E}$  analysis for  $|a_{21,2}| = 6\text{dBc}$ .

- (a) For three coefficients only.
- (b) For 3<sup>rd</sup> order only.
- (c) For 5<sup>th</sup> order only.
- (d) For 7<sup>th</sup> order only.
- (e) For 9<sup>th</sup> order only.
- (f) For 11<sup>th</sup> order only.

Table 5-3: Cardiff Model equations for different model orders.

Figure number	Number of coefficients	Model order	NMSE (dB)	The equation for coefficients extraction
Figure 5-8 (a)	3	X-parameters	-31.48	$\frac{b_{21}}{p} = K_{(21,0,0)} + K_{(21,1,1)} a_{21E}  \left(\frac{Q}{P}\right) + K_{(21,1,-1)} a_{21E}  \left(\frac{Q}{P}\right)^{-1}$
Figure 5-8 (b)	4	3 <sup>rd</sup> order	-39.92	$\frac{b_{21}}{p} = K_{(21,0,0)} + K_{(21,1,1)} a_{21E}  \left(\frac{Q}{P}\right) + K_{(21,1,-1)} a_{21E}  \left(\frac{Q}{P}\right)^{-1} + K_{(21,1,2)} a_{21E}  \left(\frac{Q}{P}\right)^2$
Figure 5-8 (c)	6	5 <sup>th</sup> order	-50.29	$\frac{b_{21}}{p} = K_{(21,0,0)} + K_{(21,1,1)} a_{21E}  \left(\frac{Q}{P}\right) + K_{(21,1,-1)} a_{21E}  \left(\frac{Q}{P}\right)^{-1} + K_{(21,1,2)} a_{21E}  \left(\frac{Q}{P}\right)^2 + K_{(21,1,-2)} a_{21E}  \left(\frac{Q}{P}\right)^{-2} + K_{(21,1,3)} a_{21E}  \left(\frac{Q}{P}\right)^3$
Figure 5-8 (D)	8	7 <sup>th</sup> order	-59.7	$\frac{b_{21}}{p} = K_{(21,0,0)} + K_{(21,1,1)} a_{21E}  \left(\frac{Q}{P}\right) + K_{(21,1,-1)} a_{21E}  \left(\frac{Q}{P}\right)^{-1} + K_{(21,1,2)} a_{21E}  \left(\frac{Q}{P}\right)^2 + K_{(21,1,-2)} a_{21E}  \left(\frac{Q}{P}\right)^{-2} + K_{(21,1,3)} a_{21E}  \left(\frac{Q}{P}\right)^3 + K_{(21,1,3)} a_{21E}  \left(\frac{Q}{P}\right)^3 + K_{(21,1,-3)} a_{21E}  \left(\frac{Q}{P}\right)^{-3} + K_{(21,1,4)} a_{21E}  \left(\frac{Q}{P}\right)^4$
Figure 5-8 (D)	8	7 <sup>th</sup> order	-59.7	$\frac{b_{21}}{p} = K_{(21,0,0)} + K_{(21,1,1)} a_{21E}  \left(\frac{Q}{P}\right) + K_{(21,1,-1)} a_{21E}  \left(\frac{Q}{P}\right)^{-1} + K_{(21,1,2)} a_{21E}  \left(\frac{Q}{P}\right)^2 + K_{(21,1,-2)} a_{21E}  \left(\frac{Q}{P}\right)^{-2} + K_{(21,1,3)} a_{21E}  \left(\frac{Q}{P}\right)^3 + K_{(21,1,3)} a_{21E}  \left(\frac{Q}{P}\right)^3 + K_{(21,1,-3)} a_{21E}  \left(\frac{Q}{P}\right)^{-3} + K_{(21,1,4)} a_{21E}  \left(\frac{Q}{P}\right)^4$

Figure number	Number of coefficients	Model order	NMSE (dB)	The equation for coefficients extraction
Figure 5-8 (E)	11	9 <sup>th</sup> order	-63.98	$\frac{b_{21}}{p} = K_{(21,0,0)} + K_{(21,1,1)} a_{21E}  \left(\frac{Q}{P}\right) +$ $K_{(21,1,-1)} a_{21E}  \left(\frac{Q}{P}\right)^{-1} + K_{(21,1,2)} a_{21E}  \left(\frac{Q}{P}\right)^2 +$ $K_{(21,1,-2)} a_{21E}  \left(\frac{Q}{P}\right)^{-2} + K_{(21,1,3)} a_{21E}  \left(\frac{Q}{P}\right)^3 +$ $K_{(21,1,3)} a_{21E}  \left(\frac{Q}{P}\right)^3 + K_{(21,1,-3)} a_{21E}  \left(\frac{Q}{P}\right)^{-3} +$ $K_{(21,1,4)} a_{21E}  \left(\frac{Q}{P}\right)^4 + K_{(21,1,-4)} a_{21E}  \left(\frac{Q}{P}\right)^{-4} +$ $K_{(21,1,5)} a_{21E}  \left(\frac{Q}{P}\right)^5$
Figure 5-8 (F)	12	11 <sup>th</sup> order	-67.39	$\frac{b_{21}}{p} = K_{(21,0,0)} + K_{(21,1,1)} a_{21E}  \left(\frac{Q}{P}\right) +$ $K_{(21,1,-1)} a_{21E}  \left(\frac{Q}{P}\right)^{-1} + K_{(21,1,2)} a_{21E}  \left(\frac{Q}{P}\right)^2 +$ $K_{(21,1,-2)} a_{21E}  \left(\frac{Q}{P}\right)^{-2} + K_{(21,1,3)} a_{21E}  \left(\frac{Q}{P}\right)^3 +$ $K_{(21,1,3)} a_{21E}  \left(\frac{Q}{P}\right)^3 + K_{(21,1,-3)} a_{21E}  \left(\frac{Q}{P}\right)^{-3} +$ $K_{(21,1,4)} a_{21E}  \left(\frac{Q}{P}\right)^4 + K_{(21,1,-4)} a_{21E}  \left(\frac{Q}{P}\right)^{-4} +$ $K_{(21,1,5)} a_{21E}  \left(\frac{Q}{P}\right)^5 + K_{(21,1,-5)} a_{21E}  \left(\frac{Q}{P}\right)^{-5}$

The above table shows different model orders linked with Figure 5-8.

Figure 5-9 shows all the seven annuli collected in the measurement process with each annulus being modelled with its corresponding, spectrally identified, behavioural model equation.

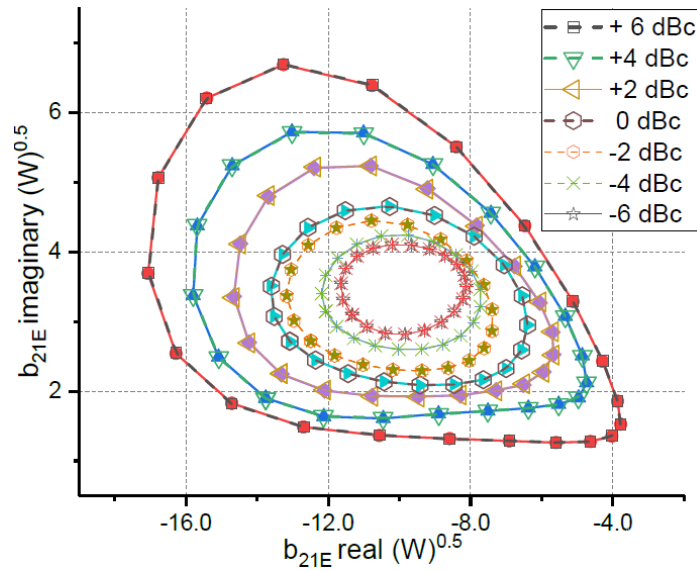


Figure 5-9:  $b_{21E}$  modelled and measured comparisons for different  $|a_{21,2}|$  power levels with phase variation only.

After identifying the maximum model order for the two-tone measurements, selected impedances were used for CW measurement and model analysis was performed to verify whether the identification holds for the CW domain.

Figure 5-10 shows the impedance area covered by the load-modulation that occurs from the two-tone measurements. The -6dBc, 0dBc, and 6dBc annuli are highlighted, and the optimum load is plotted with an asterisk. This shows that, with only seven measurements, a large area of the Smith Chart can be captured, and the maximum model order identified for each area.

To validate the model, the  $a_{21}$  settings of the maximum model order of the two-tone measurements will be used to target the fundamental load-pull space of the continuous wave (data point markers in Figure 5-10 measurements). It shows how the model exhibits magnitude and phase variation for the larger annuli while this part of the analysis was based on model identification of the phase polynomial only.

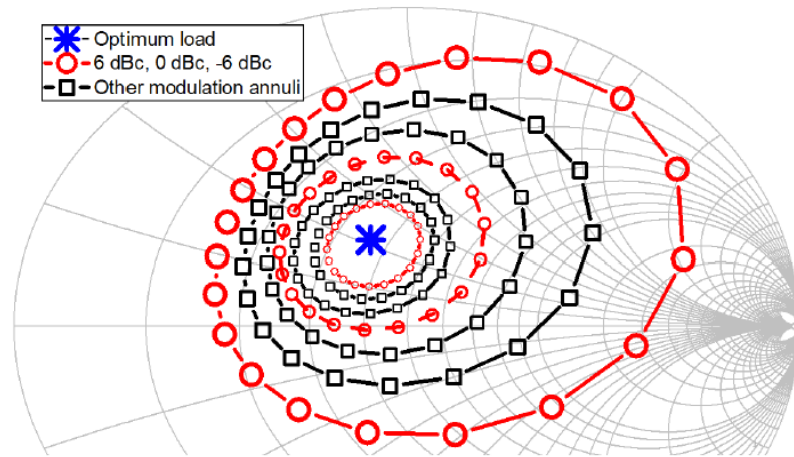


Figure 5-10: Load-modulation annuli for different  $|a_{21,2}|$  power levels. Trace icons indicate impedance targets for CW measurement.

To quantify the results, the Normalised Mean Square Error (NMSE) [6] was calculated for measured and modelled data comparison. Figure 5-11 plots the NMSE, for selected  $|a_{21,2}|$  power levels, against a model order for the two-tone and CW cases. It should be mentioned that the analytical X-parameter formulation is still valid when the  $|a_{21,2}| < 2\text{dBc}$ . However,  $|a_{21,2}| = 2\text{dBc}$  is where the analytical X-parameter begins to produce  $(\text{NMSE}) > -40\text{dB}$ , above 1% error, below 2dBc the error is acceptable but not optimal. It can be seen that the addition of model coefficients increases the accuracy of the model and that the two-tone

and CW results are offset for  $|a_{21,2}| = 0\text{dBc}$  and  $|a_{21,2}| = 6\text{dBc}$ , this is due to an  $a_{21}$  that exhibits magnitude and phase variation for the larger annuli in Figure 5-10. However, the maximum model order, obtained from the two-tone measurements, holds for the CW case ( $\text{NMSE} < -40\text{dB}$ ). In both cases, small gains in accuracy can be achieved after the identified model order. However, the models would be overdetermined.

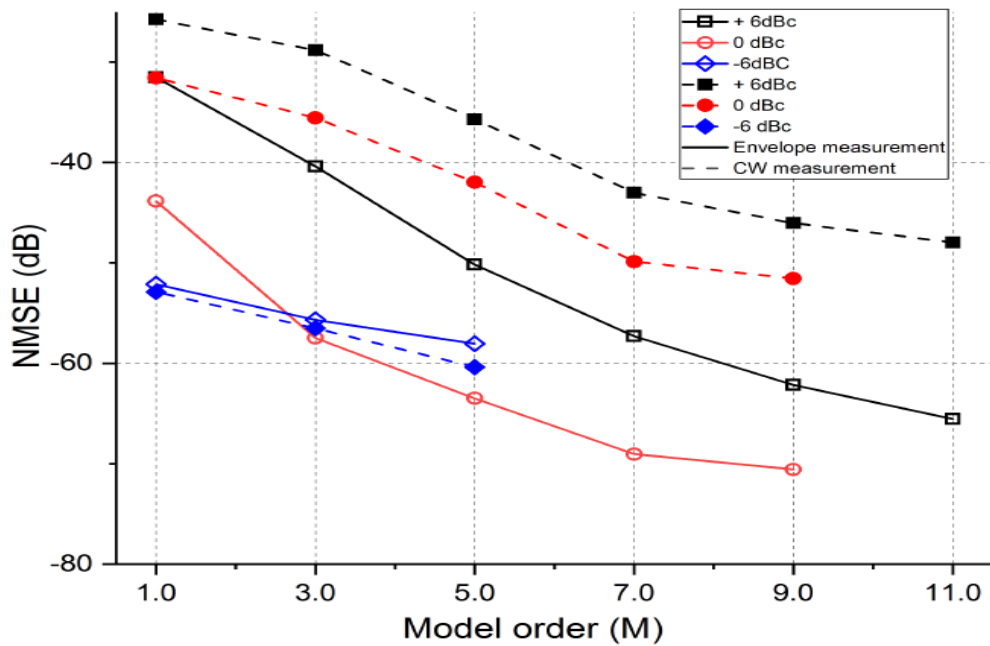


Figure 5-11: NMSE versus a model order for two-tone measurements at selected  $|a_{21,2}|$  and CW measurements with impedances lying on their respective two-tone load-modulation annuli.

### 5.2.1 BEHAVIOURAL MODELLING WITH MAGNITUDE AND PHASE VARIATION

Recalling early work in Figure 5-9, which illustrates all seven annuli collected in the measurement process for different  $|a_{21,2}|$ . To exercise

the area through magnitude and phase changes, these annuli can be modelled with magnitude and phase variation as different  $|a_{21,2}|$  power levels are introduced in the model.

Figure 5-12 depicts how the two annuli for  $|a_{21,2}| = -6\text{dBc}$  and  $-4\text{dBc}$  are combined so a model accounted for both phase and magnitude variation, can then be extracted. The resulting  $b_{21E}$  the model accurately fits the data.

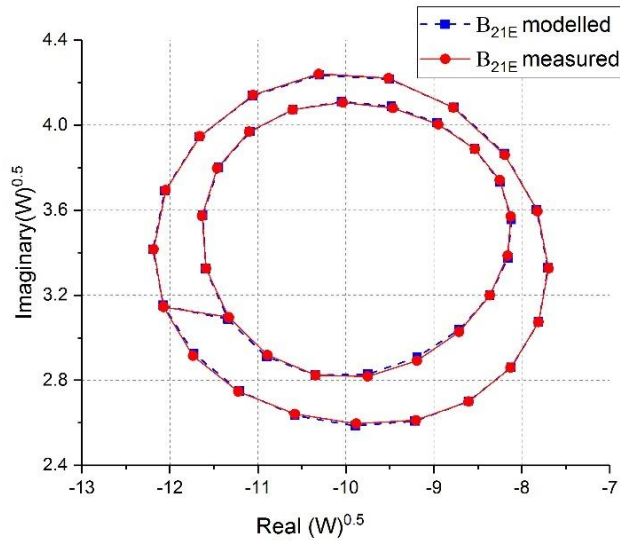


Figure 5-12:  $b_{21E}$  modelled and measured comparisons for  $|a_{21,2}| = -6\text{dBc}$  and  $-4\text{dBc}$ .

Equation (5-5) shows the mixing term that are used to identify the model complexity.

$$\begin{aligned}
 \frac{b_{21}}{p} = & K_{(21,0,0)} + K_{(21,1,1)}|a_{21E}| \left(\frac{Q}{P}\right) + K_{(21,1,-1)}|a_{21E}| \left(\frac{Q}{P}\right)^{-1} + \\
 & K_{(21,2,2)}|a_{21E}|^2 \left(\frac{Q}{P}\right)^2 + K_{(21,2,0)}|a_{21E}|^2 + K_{(21,3,1)}|a_{21E}|^3 \left(\frac{Q}{P}\right)^1 + \\
 & K_{(21,3,-1)}|a_{21E}|^3 \left(\frac{Q}{P}\right)^{-1} + K_{(21,4,2)}|a_{21E}|^4 \left(\frac{Q}{P}\right)^2 + \\
 & K_{(21,3,3)}|a_{21E}|^3 \left(\frac{Q}{P}\right)^3
 \end{aligned} \tag{5-5}$$

In order to define the necessary model complexity, new mixing terms (as shown in eq. (5-5)) are added that include magnitude variation in the model with coefficients such as  $K_{(21,2,0)}$ ,  $K_{(21,3,-1)}$ ,  $K_{(21,3,1)}$  and  $K_{(21,4,2)}$ . These mixing terms have the same phase locations as previous terms but add an additional squared dependency on the magnitude of  $|a_{21}|$  that causes shifting in the centre of the ellipse. In this case, only two annuli are used hence can only have up to two coefficients per phase element.

In Figure 5-13, the model analysis includes all  $|a_{21,2}|$  variation from -6dBc to +6dBc. To show the coefficient contributions at each  $|a_{21,2}|$  power offset, the same mixing terms have been used to identify the model as can be seen in Figure 5-14. This gives an insight that some coefficients have insignificant contribution such as  $K_{(21,3,-1)}$  and  $K_{(21,2,-2)}$  while  $K_{(21,1,-1)}$  has considerable effects when the model complexity gets increased.

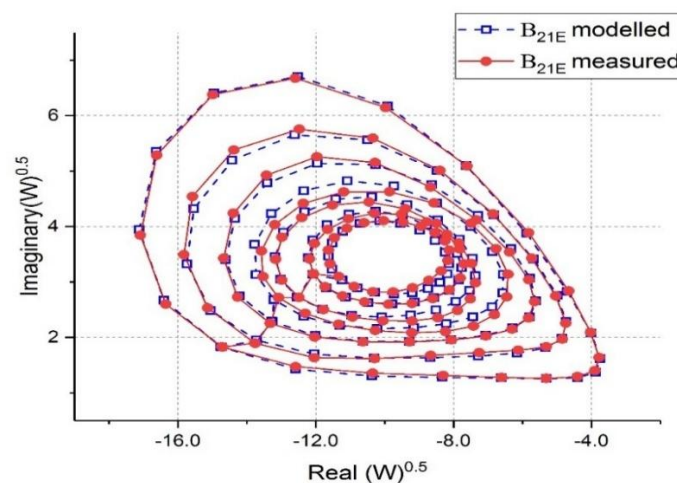


Figure 5-13:  $b_{21E}$  modelled and measured comparisons for different  $|a_{21,2}|$  levels.

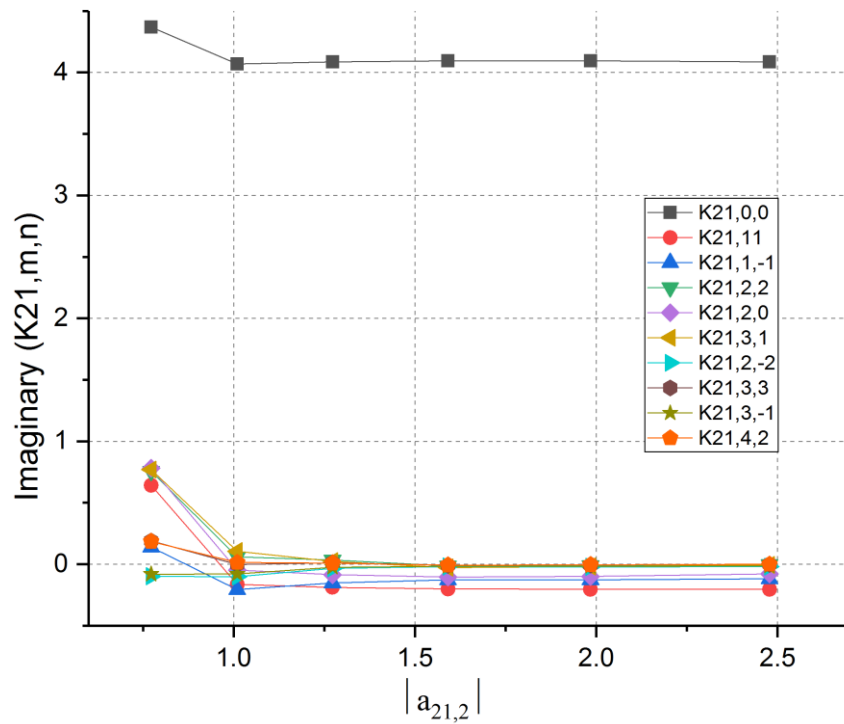
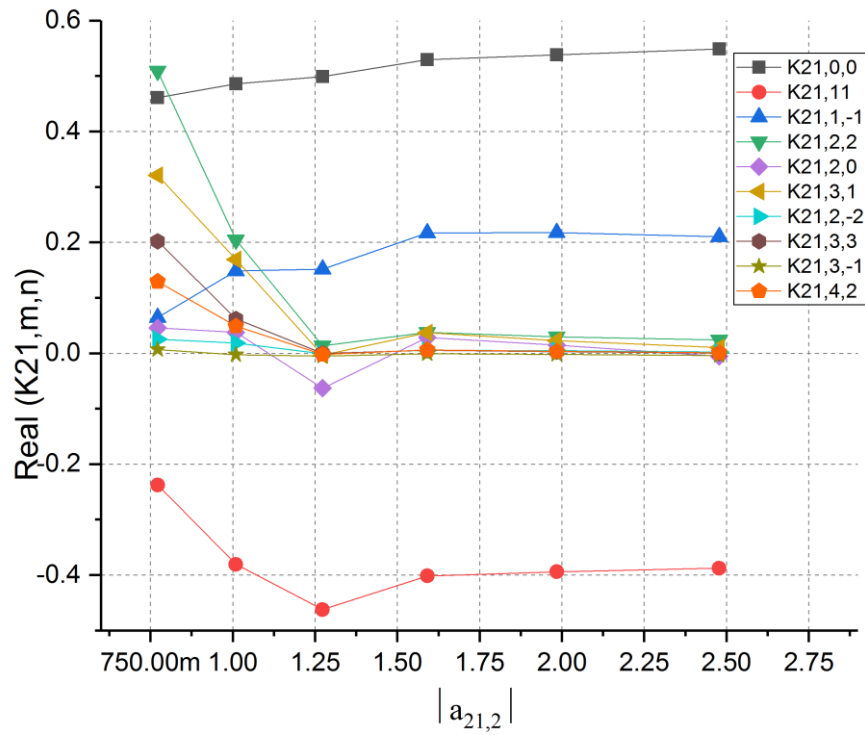


Figure 5-14: Real and imaginary model coefficients for different power level offset.

To have a better understanding of mixing terms and their association with magnitude and phase  $(m,n)$  exponents, Figure 5-15 can conveniently describe the distribution of each term in the spectral domain.

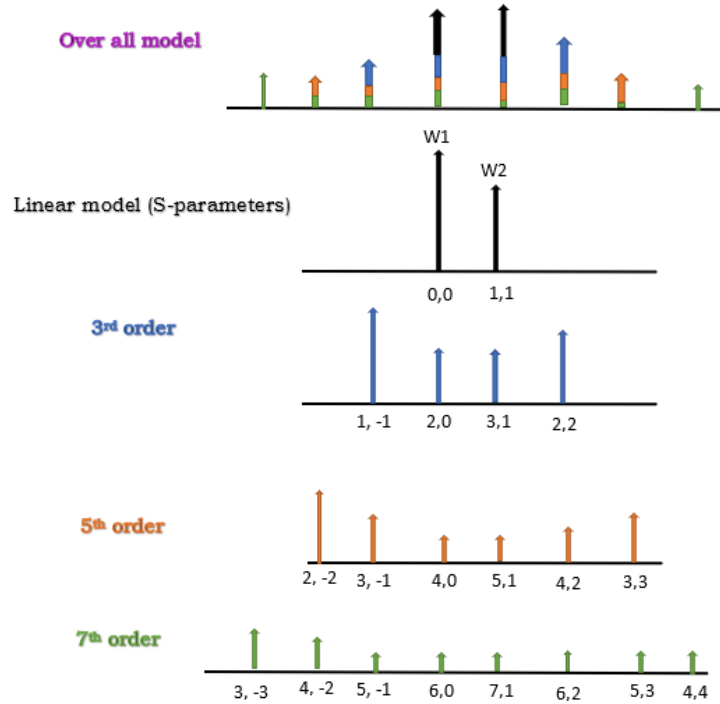


Figure 5-15: spectral domain of mixing terms.

Table 5-4: Magnitude and phase exponents for the 7<sup>th</sup> order model.

Model order	1 <sup>st</sup>	1 <sup>st</sup>	3 <sup>rd</sup>	3 <sup>rd</sup>	3 <sup>rd</sup>	5 <sup>th</sup>	7 <sup>th</sup>												
M (Mag.)	0	1	1	2	2	3	2	3	3	4	4	5	3	4	4	5	5	6	7
$\emptyset$ (Phase)	0	1	-1	2	0	1	-2	3	-1	2	0	1	-3	4	-2	3	-1	0	1

It would imply that the ultimate model has the contribution of each term with different model order. Furthermore, it shows how magnitude mixing terms such as  $(2,0, 3,1$  and/or  $3,-1)$  are superimposed on the same phase components  $(0,0, 1,1$  and/or  $1,-1)$  respectively, this imposes a dilemma during modelling extraction as it

---

is difficult to differentiate between the phase and model mixing terms. Hence, a novel technique is employed through the engineering of a multi-tone  $A_{21}(t)$  stimulus, involving a carrier phase and amplitude modulation components. This allows the separation of the magnitude and phase components of  $B_{21}(t)$  device's response, which can be independently observed. More details are provided in the following section.

### 5.3 BEHAVIOURAL MODEL EXTRACTION FOR MULTI-TONE STIMULUS

The work presented, so far, in this chapter has focused on model identification using a two-tone stimulus. A phase modulated signal  $a_{21,2}$  spaced 1kHz from the main tone  $a_{21,1}$  was utilised to identify phase model coefficients  $K_{p,q,m,n}$  with different modulated stimulus inputs.

The challenge in using the Cardiff behavioural model is to select the required mixing terms correctly. Recent work has focused on using mixing order [8] and targeted load-pull measurements [7] to aid in the selection of the required mixing terms. In this section, the model complexity identification concept has been extended to include both magnitude and phase related mixing terms. Through the engineering of a multi-tone  $A_{21}(t)$  stimulus, involving a carrier phase and amplitude modulation components, the spectra of the device  $B_{21}(t)$  response enables clear identification of model complexity by avoiding

spectral overlap of the associated mixing terms. This is considered an essential step in correctly and accurately modelling the device by, allowing, for the first time, the ability to visualize all the mixing terms. Furthermore, formulating the model coefficient least mean square (LMS) extraction process using the FFT transformed data provides for a very robust, direct extraction, solution for model coefficient determination.

#### 5.4 MODEL IDENTIFICATION FOR MULTI-TONE STIMULUS

The main-tone frequency and the centre tone of the receivers ( $a_{21,1}$ ) were set to 1GHz. The selected phase and amplitude modulated load-pull signal consists of tones, ( $a_{21,2}$ ,  $a_{21,3}$  and  $a_{21,4}$ ), offset at frequencies 39kHz, 43kHz and 47kHz respectively. This relates to phase modulation at 43kHz and amplitude modulations at 4kHz as follow.

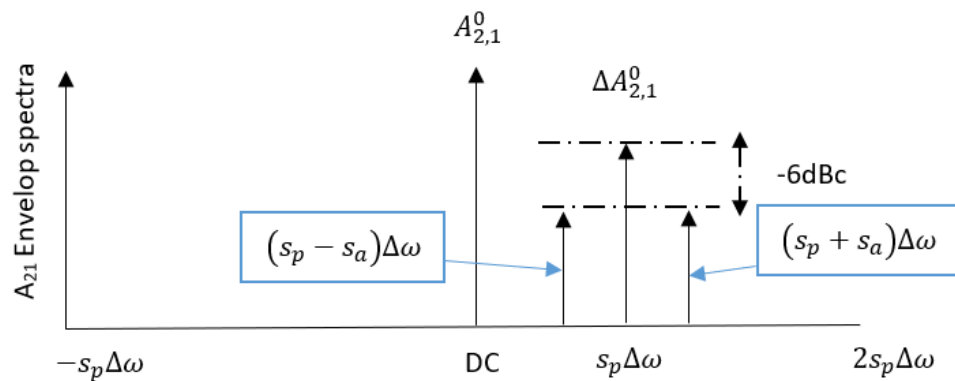


Figure 5-16: spectral tones of the four-tone stimulus.

The Cardiff Behavioural Model, which is based on the application of signal mixing, provides a theoretically robust framework for describing non-linear behaviour.

$$B_{p,h}(|A_{11}|) = Q_{1,1}^h \left( \sum_{r=0}^{r=\infty} \sum_{n=-\infty}^{n=\infty} K_{p,h,m,n} (|A_{11}|) |A_{21}|^{m=|n|+2r} \left( \left( Q_{21}/Q_{11} \right) \right)^n \right) \quad (5-6)$$

This model can be utilised within CAD design tools to predict fundamental design behaviour such as load-pull contours [4] [5]. However, the robustness and accuracy of these predictions is dependent on the selection of the necessary model complexity,  $m$  and  $n$  range, and the accurate determination of the model coefficients  $K_{p,h,m,n}$ .

Generally, active load-pull systems inject a series of load-pull signals  $A_{2,1}$  using a CW stimulus at the carrier frequency  $\omega_c$ . The behavioural model is then extracted by curve-fitting to the measured  $B_{2,1}$  device response. An alternative approach would be to inject a time varying load-pull signal  $A_{2,1}(t)$  using a multi-tone stimulus.

$$A_{2,1}(t) = \frac{A_{2,1}^E(t)e^{j\omega_c t} + A_{2,1}^E(t)^* e^{-j\omega_c t}}{2} \quad (5-7)$$

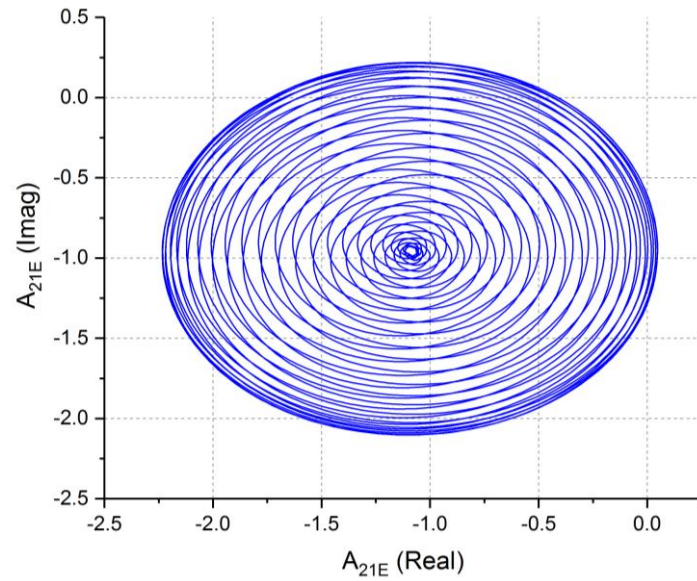
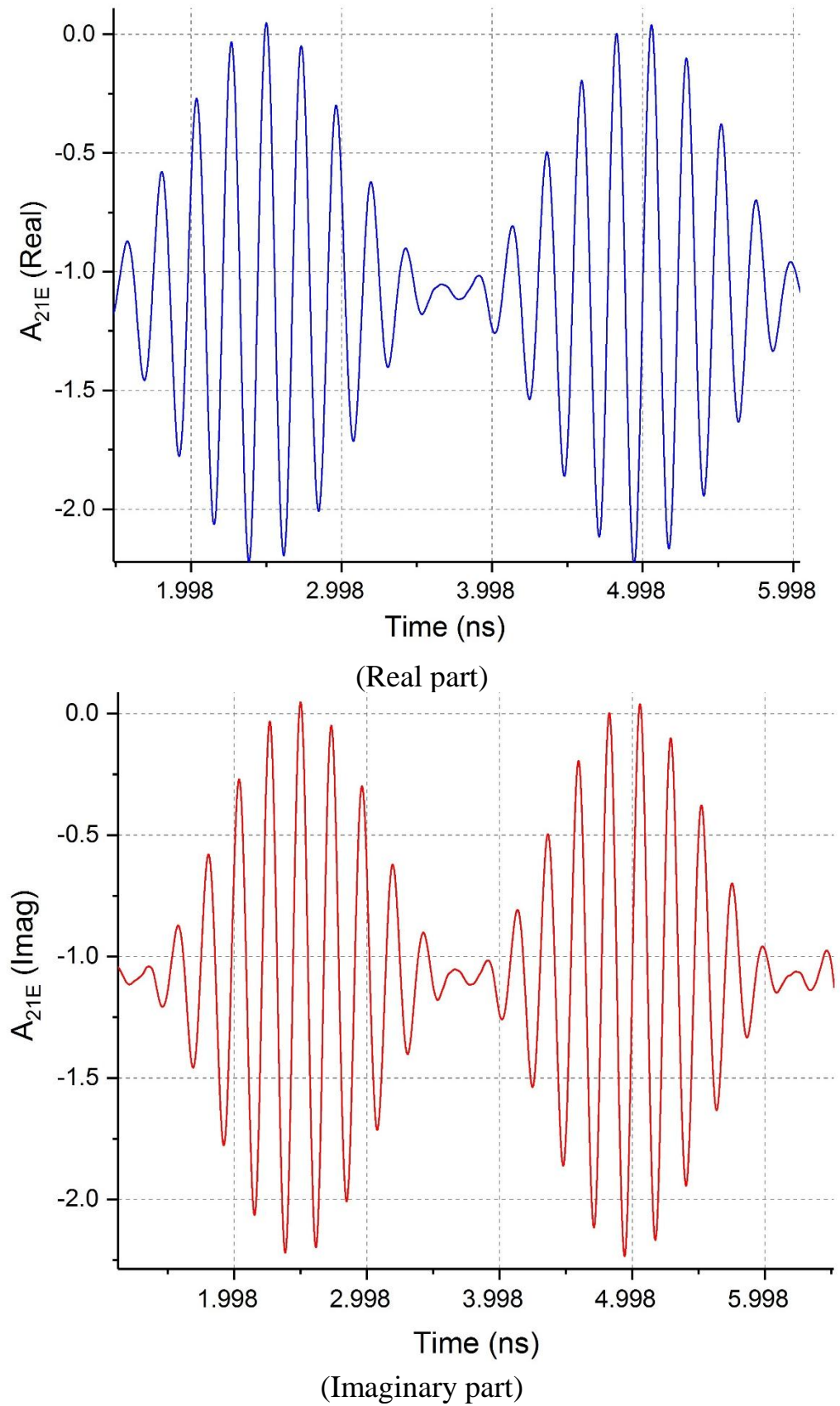


Figure 5-17: The  $A_{21}(t)$  stimulus to be injected into the DUT.

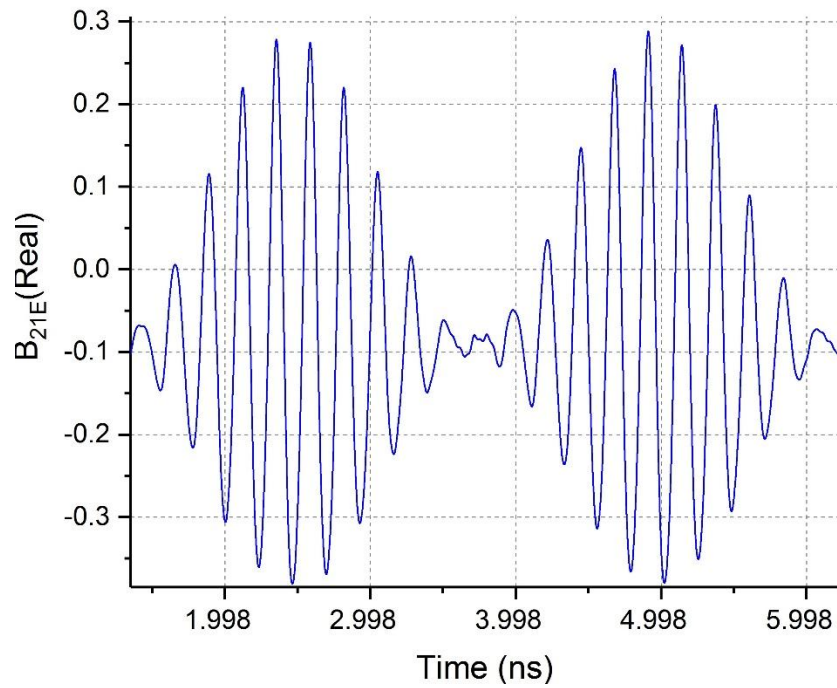
The key now is to engineer a novel excitation envelop signal  $A_{2,1}^E(t)$ , so that, from the resulting  $B_{2,1}^E(t)$  envelope response, it is possible to identify the required model complexity. Consider the following multi-tone stimulus:

$$A_{2,1}^E(t) = A_{2,1}^0(t) + \Delta A_{2,1} \quad (5-8)$$

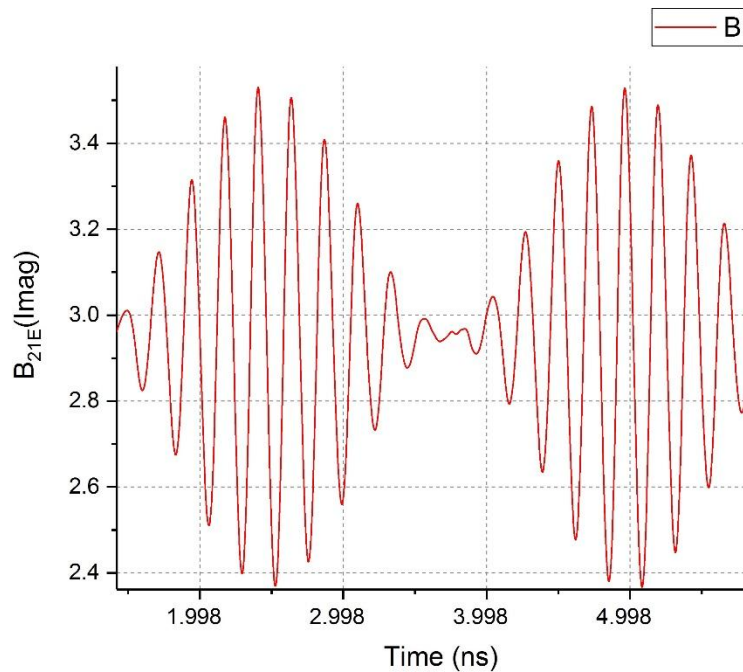
The time-varying signal is plotted below;

Figure 5-18: Time domain waveform of  $A_{21}^E$  envelop.

The  $B_{2,1}^E(t)$  the response of time varying signal is plotted as, shown in Figure 5-19.



(Real part)



(Imaginary part)

Figure 5-19: Time domain waveform of  $b_{2,1}^E$  envelop.

The  $A_{2,1}$  stimulus consists of a reference component  $A_{2,1}^0$  that defines the reference impedance about which the load-pull is performed and a variable component  $\Delta A_{2,1}$  that performs the load-pull. It is key to select  $\Delta A_{2,1}$  so that it provides for model identification and robust coefficient extraction. Consider the following three tone stimulus.

$$\Delta A_{2,1}^E(t) = \frac{A_{2,1}^{\Delta}}{2} (1 + \text{COS}(s_a \omega t) (\text{COS}(s_p \omega t) + j \text{SIN}(s_p \omega t))) \quad (5-9)$$

The selected three tone stimulus consists of a phase modulated component,  $\cos(s_p \Delta \omega t) + j \sin(s_p \Delta \omega t)$  which allows for identification of the model phase terms,  $(Q_{21}/Q_{11})^n$  and an amplitude modulated component  $\cos(s_a \Delta \omega t)$ , which allows for identification of the model amplitude terms,  $|A_{21}|^{m=|n|+2r}$ .

The magnitude of the phase modulation tone  $(\omega_c + s_p \Delta \omega)$ , was varied from -10dBc to -4dBc, referenced to the main (carrier) tone  $|A_{2,1}^0|$  while the other two tones  $(\omega_c + s_p \Delta \omega - s_a \Delta \omega)$  and  $(\omega_c + s_p \Delta \omega + s_a \Delta \omega)$ , provide for amplitude modulation and, were always set to be -6dBc referenced to the phase tone  $(\omega_c + s_p \Delta \omega)$ . Keeping the amplitude modulation tones at least -6dBc, relative to the phase modulation tone ensures phase inversion is avoided. In this thesis, the high frequency of  $(s_p \Delta \omega) = 43$  kHz was chosen for spectral clarity; however, it can be customized according to the estimated severity of non-linearity.

## 5.5 MATHEMATICAL EXTRACTION OF CARDIFF BEHAVIOURAL MODEL

Applying the Cardiff Behavioural Model to the phase normalized  $Q^h = 1$ , the envelope signal gives the following.

$$B_{2,1}^E(t) = \left( \sum_{r=0}^{r=\infty} \sum_{n=-\infty}^{n=\infty} M_{m,n} |\Delta A_{2,1}^E(t)|^{m=|n|+2r} \left( \frac{\Delta A_{2,1}^E(t)}{|\Delta A_{2,1}^E(t)|} \right)^n \right) \quad (5-10)$$

The spectrum of the envelope signal  $B_{2,1}^E(\Delta\omega)$  is therefore the sum of the spectra of the required model terms;

$$\begin{aligned} B_{2,1}^E\langle\Delta\omega\rangle &= \\ &\left( \sum_{r=0}^{r=\infty} \sum_{n=-\infty}^{n=\infty} M_{m,n} \text{fft} \left\langle \left| \Delta A_{2,1}^E(t) \right|^{m=|n|+2r} \left( \frac{\Delta A_{2,1}^E(t)}{|\Delta A_{2,1}^E(t)|} \right)^n \right\rangle \right) \\ &= \left( \sum_{r=0}^{r=\infty} \sum_{n=-\infty}^{n=\infty} M_{m,n} F_{m,n}^E\langle\Delta\omega\rangle \right) \end{aligned} \quad (5-11)$$

Analysis of the  $B_{2,1}^E\langle\Delta\omega\rangle$  spectrum allows the model complexity to be identified. Figure 5-20 shows the spectral model coefficients up to 5<sup>th</sup> order.

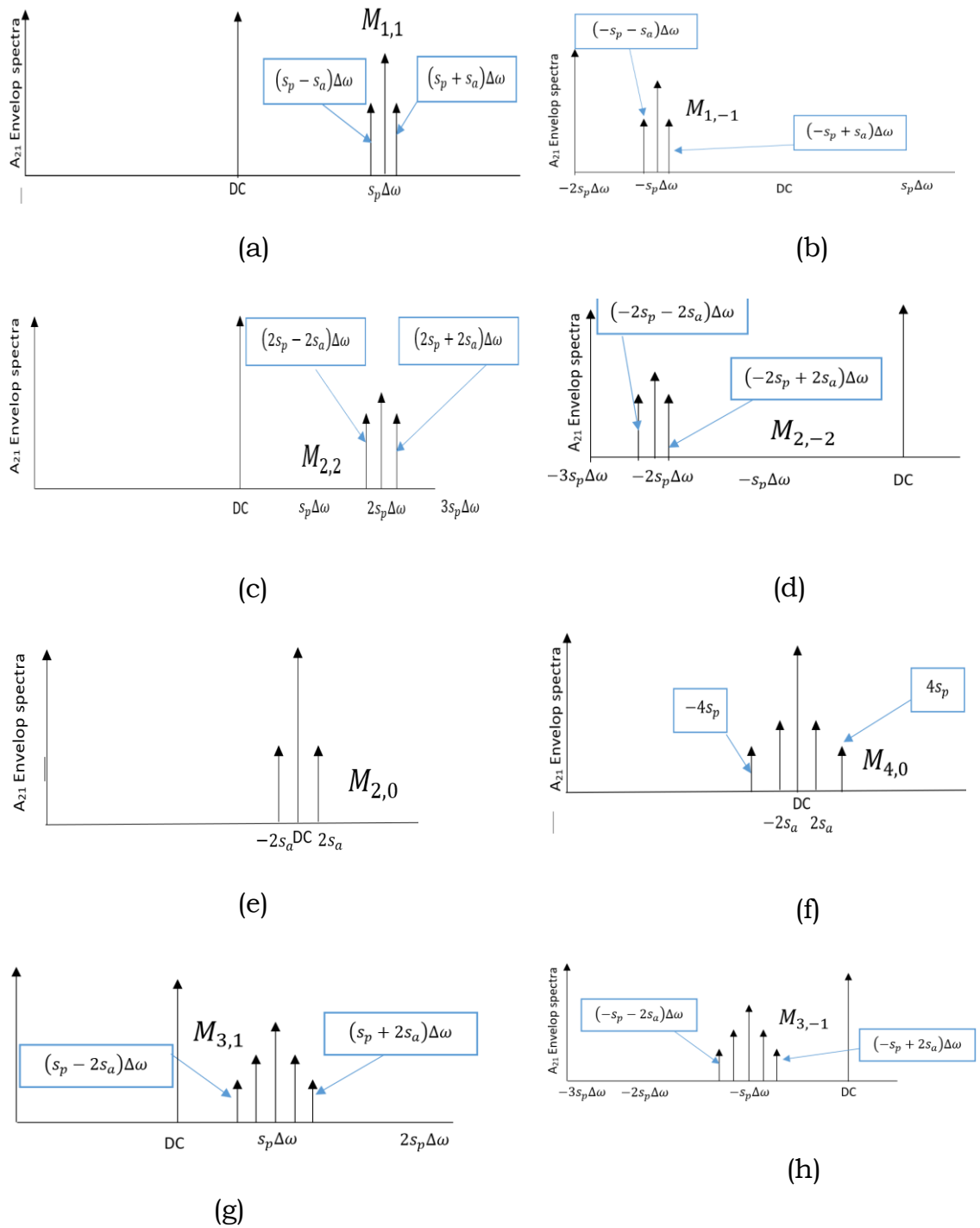


Figure 5-20: Model identification for different model orders.

The table below shows the extracted model coefficients linked to Figure 5-20.

Table 5-5: Extracted equations for different model orders.

Figure number	Model order	Mixing term	The equation for different model coefficient extraction
Figure 5-20(a)	1 <sup>st</sup> order	$M_{1,1}$	$ \Delta A_{2,1}^E(t) ^1 \left( \frac{\Delta A_{2,1}^E(t)}{ \Delta A_{2,1}^E(t) } \right)^{+1}$
Figure 5-20 (b)	3 <sup>rd</sup> order	$M_{1,-1}$	$ \Delta A_{2,1}^E(t) ^1 \left( \frac{\Delta A_{2,1}^E(t)}{ \Delta A_{2,1}^E(t) } \right)^{-1}$
Figure 5-20 (c)	3 <sup>rd</sup> order	$M_{2,2}$	$ \Delta A_{2,1}^E(t) ^2 \left( \frac{\Delta A_{2,1}^E(t)}{ \Delta A_{2,1}^E(t) } \right)^{+2}$
Figure 5-20 (d)	5 <sup>th</sup> order	$M_{2,-2}$	$ \Delta A_{2,1}^E(t) ^2 \left( \frac{\Delta A_{2,1}^E(t)}{ \Delta A_{2,1}^E(t) } \right)^{-2}$
Figure 5-20 (e)	3 <sup>rd</sup> order	$M_{2,0}$	$ \Delta A_{2,1}^E(t) ^2$
Figure 5-20 (f)	5 <sup>th</sup> order	$M_{4,0}$	$ \Delta A_{2,1}^E(t) ^4$
Figure 5-20 (g)	3 <sup>rd</sup> order	$M_{3,1}$	$ \Delta A_{2,1}^E(t) ^3 \left( \frac{\Delta A_{2,1}^E(t)}{ \Delta A_{2,1}^E(t) } \right)^{+1}$
Figure 5-20 (h)	5 <sup>th</sup> order	$M_{3,-1}$	$ \Delta A_{2,1}^E(t) ^3 \left( \frac{\Delta A_{2,1}^E(t)}{ \Delta A_{2,1}^E(t) } \right)^{-1}$

### 5.5.1 MODEL EXTRACTION

For the selected stimulus, the resulting spectra of each of the model components,  $F_{m,n}^E\langle\Delta_\omega\rangle$ , can be easily computed. Figure 5-21 shows the spectra of the down-converted  $B_{2,1}^E(t)$ , (the b-envelope about the fundamental tone) for a small load-pull area (phase tone = -10dBc). Highlighted on this figure are the model terms associated with the observed spectral lines. This demonstrates how the analysis of the  $B_{2,1}^E\langle\Delta_\omega\rangle$  spectra allow the required behavioural model complexity to be determined by accounting for all the tones clearly observed above the noise floor (ignoring the term  $M_{3,3}$  and  $M_{3,-3}$  as they are just above the noise floor and their contribution to the model are small). Note, the values of the individual model coefficients,  $M_{m,n}$ , can also be extracted from their respective spectral lines.

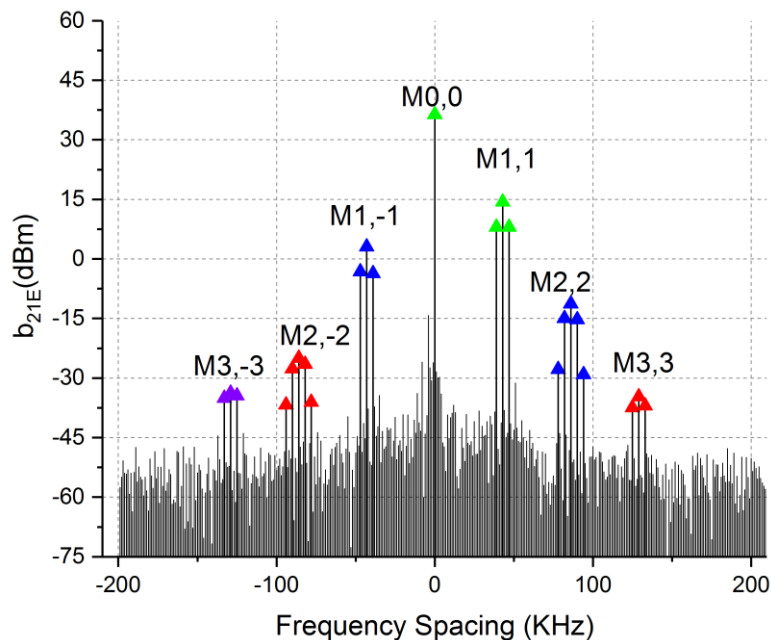


Figure 5-21:  $B_{2,1}^E$  spectrum showing 7<sup>th</sup> order coefficients for phase modulated tone = -10dBc.

The identified model, in this case, is as follows;

$$B_{2,1}^E(t) = M_{(0,0)} + M_{(1,1)} (\Delta A_{2,1}^E(t)) + M_{(1,-1)} (\Delta A_{2,1}^E(t))^{-1} + \quad (5-12)$$

$$+ M_{(2,2)} (\Delta A_{2,1}^E(t))^2 + M_{(2,-2)} (\Delta A_{2,1}^E(t))^{-2}$$

This can be written in the following matrix form;

$$[B_{2,1}^E(t)] = \left[ (\Delta A_{2,1}^E(t))^{-2} (\Delta A_{2,1}^E(t))^{-1} \ 1 \ (\Delta A_{2,1}^E(t))^1 (\Delta A_{2,1}^E(t))^2 \right] * \begin{bmatrix} M_{2,-2} \\ M_{1,-1} \\ M_{0,0} \\ M_{1,1} \\ M_{2,2} \end{bmatrix}$$

$$[B(t)] = [AA(t)] \times [M] \quad (5-13)$$

Apply the “least square curve-fitting” algorithm to the time-sequenced data allows for the determination of the model coefficients. This is what is typically done with load-pull data, which is in effect just a time sampled set of data.

$$[M] = \left[ (AA(t)^H AA(t))^{-1} \right] [AA(t)^H B(t)] \quad (5-14)$$

This matrix formulation is normally used in LMS extraction process to determine the values of the model coefficients from a set of load-pull measurements. Consider now the alternative formulation in the frequency domain.

$$[B_{2,1}^E \langle \Delta \omega \rangle] = \left[ \begin{array}{ccccccc} \text{fft}(\Delta A_{2,1}^E(t))^{-2} & \text{fft}(\Delta A_{2,1}^E(t))^{-1} & \text{fft}(1) & \text{fft}(\Delta A_{2,1}^E(t))^1 & \text{fft}(\Delta A_{2,1}^E(t))^2 & & \\ & & & & & & \end{array} \right] * \begin{bmatrix} M_{2,-2} \\ M_{1,-1} \\ M_{0,0} \\ M_{1,1} \\ M_{2,2} \end{bmatrix}$$

$$[B \langle \Delta \omega \rangle] = [FF \langle \Delta \omega \rangle] \times [M] \quad (5-15)$$

The matrix equation in (5-15), defined in the envelope frequency domain, can also be used to extract the model coefficients using in the least mean square (LMS) extraction process. Let us consider this matrix equation in more detail. Using the selected multi-tone stimulus and the model elements identified, this equation can be written, as shown in Figure 5-22. It is worth noting that the number of rows refers to the frequency index in the matrix while the number of columns denotes the number of required model coefficients. Here, the coefficients in this matrix were chosen based on the model complexity of the phase modulated signal equal to -10dBc. It is essential to highlight that the  $F_{m,n}^E$  matrix has a diagonal structure, hence, the model coefficient terms in this case, are extracted individually.



In the case of the individual model, coefficients are independently directly extracted from the measured data as follow:

$$\begin{bmatrix} B_{2,1}^E \left( (-2s_p - 4s_a)\Delta\omega \right) \\ B_{2,1}^E \left( (-2s_p - 2s_a)\Delta\omega \right) \\ B_{2,1}^E \left( (-2s_p)\Delta\omega \right) \\ B_{2,1}^E \left( (-2s_p + 2s_a)\Delta\omega \right) \\ B_{2,1}^E \left( (-2s_p + 4s_a)\Delta\omega \right) \end{bmatrix} = \begin{bmatrix} F_{2,-2}^E \left( (-2s_p - 4s_a)\Delta\omega \right) \\ F_{2,-2}^E \left( (-2s_p - 2s_a)\Delta\omega \right) \\ F_{2,-2}^E \left( (-2s_p)\Delta\omega \right) \\ F_{2,-2}^E \left( (-2s_p + 2s_a)\Delta\omega \right) \\ F_{2,-2}^E \left( (-2s_p + 4s_a)\Delta\omega \right) \end{bmatrix} \times M_{2,-2}$$

$$\begin{bmatrix} B_{2,1}^E \left( (-s_p - s_a)\Delta\omega \right) \\ B_{2,1}^E \left( (-s_p)\Delta\omega \right) \\ B_{2,1}^E \left( (-s_p + s_a)\Delta\omega \right) \end{bmatrix} = \begin{bmatrix} F_{1,-1}^E \left( (-s_p - s_a)\Delta\omega \right) \\ F_{1,-1}^E \left( (-s_p)\Delta\omega \right) \\ F_{1,-1}^E \left( (-s_p + s_a)\Delta\omega \right) \end{bmatrix} \times M_{1,-1}$$

$$\begin{bmatrix} B_{2,1}^E(0) \end{bmatrix} = [1] \times M_{0,0}$$

$$\begin{bmatrix} B_{2,1}^E \left( (s_p - s_a)\Delta\omega \right) \\ B_{2,1}^E \left( (s_p)\Delta\omega \right) \\ B_{2,1}^E \left( (s_p + s_a)\Delta\omega \right) \end{bmatrix} = \begin{bmatrix} F_{1,1}^E \left( (s_p - s_a)\Delta\omega \right) \\ F_{1,1}^E \left( (s_p)\Delta\omega \right) \\ F_{1,1}^E \left( (s_p + s_a)\Delta\omega \right) \end{bmatrix} \times M_{1,1}$$

$$\begin{bmatrix} B_{2,1}^E \left( (+2s_p - 4s_a)\Delta\omega \right) \\ B_{2,1}^E \left( (+2s_p - 2s_a)\Delta\omega \right) \\ B_{2,1}^E \left( (+2s_p)\Delta\omega \right) \\ B_{2,1}^E \left( (+2s_p + 2s_a)\Delta\omega \right) \\ B_{2,1}^E \left( (+2s_p + 4s_a)\Delta\omega \right) \end{bmatrix} = \begin{bmatrix} F_{2,2}^E \left( (+2s_p - 4s_a)\Delta\omega \right) \\ F_{2,2}^E \left( (+2s_p - 2s_a)\Delta\omega \right) \\ F_{2,2}^E \left( (+2s_p)\Delta\omega \right) \\ F_{2,2}^E \left( (+2s_p + 2s_a)\Delta\omega \right) \\ F_{2,2}^E \left( (+2s_p + 4s_a)\Delta\omega \right) \end{bmatrix} \times M_{2,2}$$

## 5.6 EXPERIMENTAL VERIFICATION

Figure 5-23 shows the comparison of the resultant  $B_{2,1}^E(t)$  for the modelled and measured data where the normalized mean square error (NMSE) equals -49.21dB.

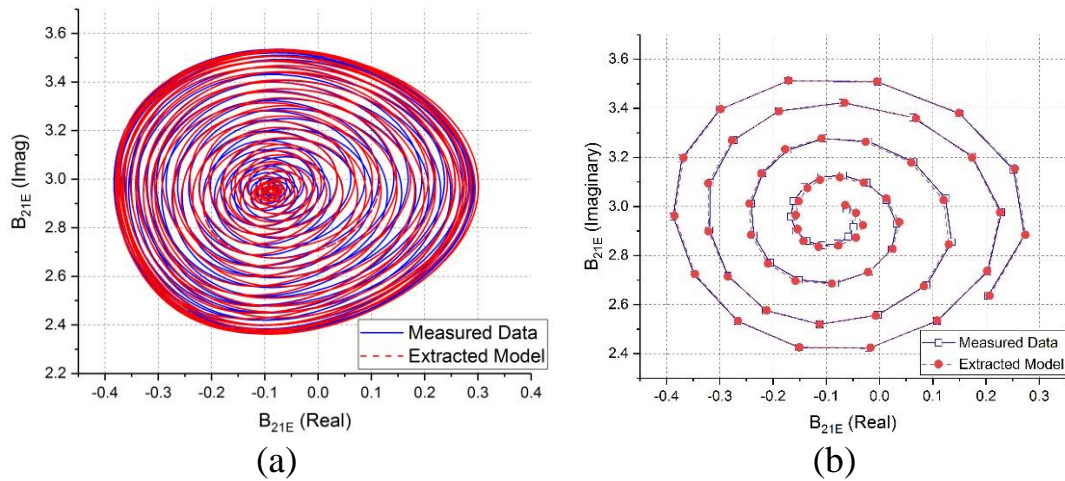


Figure 5-23:  $B_{2,1}^E(t)$  comparison for measured and modelled data for phase modulated tone=-10dBc.

- (a) Before decimated the  $B_{2,1}^E(t)$  array wherein number of points = 5882.
- (b) After decimated the  $B_{2,1}^E(t)$  array wherein number of points = 58.

Figure 5-24 identifies the area on the Smith Chart that the multi-tone signal has performed load-pull over. Depicted are measured and modelled load-pull impedances, generated from the  $a_{21}$  modulation spirals. Note, the good agreement between measured and modelled load impedance points.

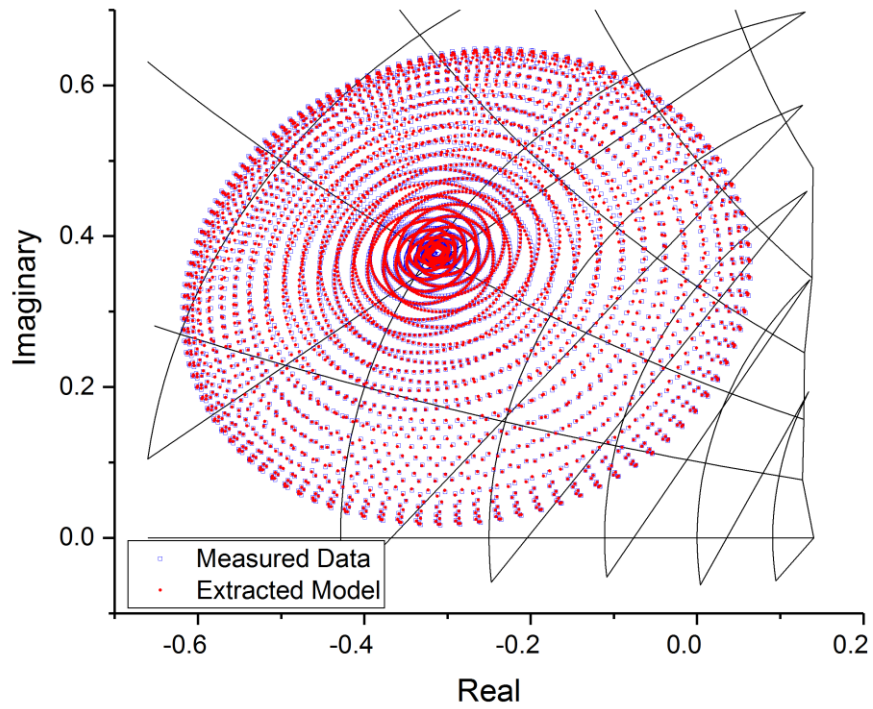
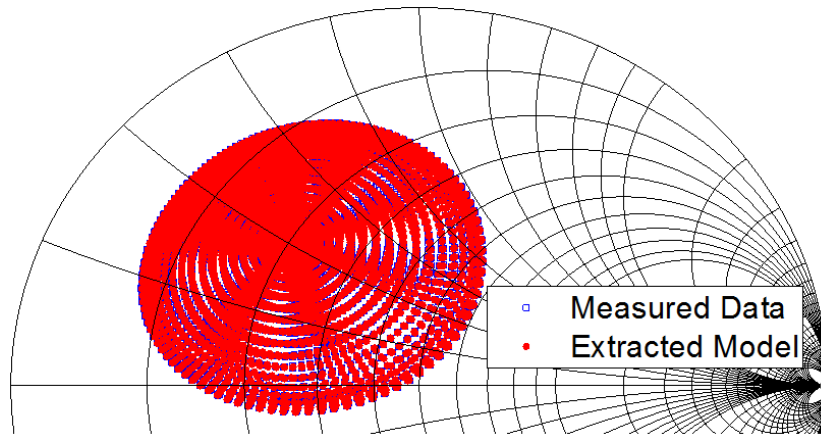


Figure 5-24: Modelled vs measured contour space for the load-modulation with phase modulated tone =-10dBc.

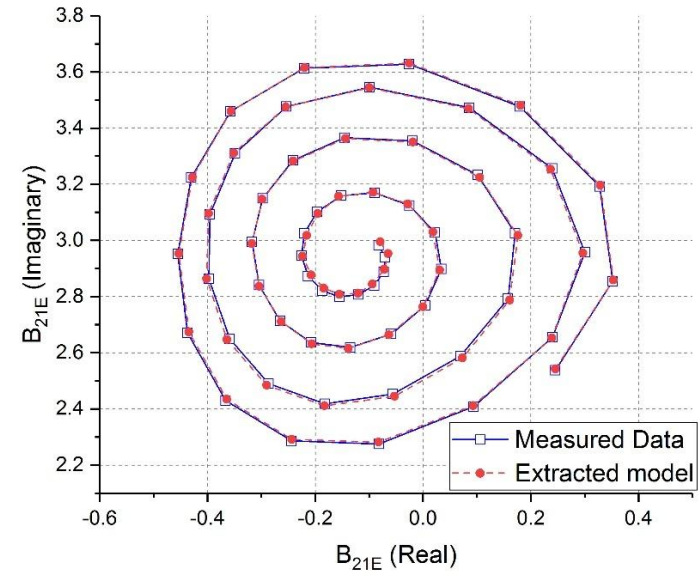
Consider now the case when the load-pull area on the Smith Chart is increased (see Figure 5-25) where the phase modulated tone equals -8dBc and -6dBc. The NMSE is listed in Table 5-6 for comparison between the modelled and measured gamma loads and different input stimuli.

Table 5-6: NMSE for different modulated signal inputs.

Figure number	Phase modulated signal input	Model Order	NMSE (dB)
Figure 5-25(a)	-8dBc	7 <sup>th</sup> order	-49.7
Figure 5-25(b)	-6dBc	7 <sup>th</sup> order	-47.2

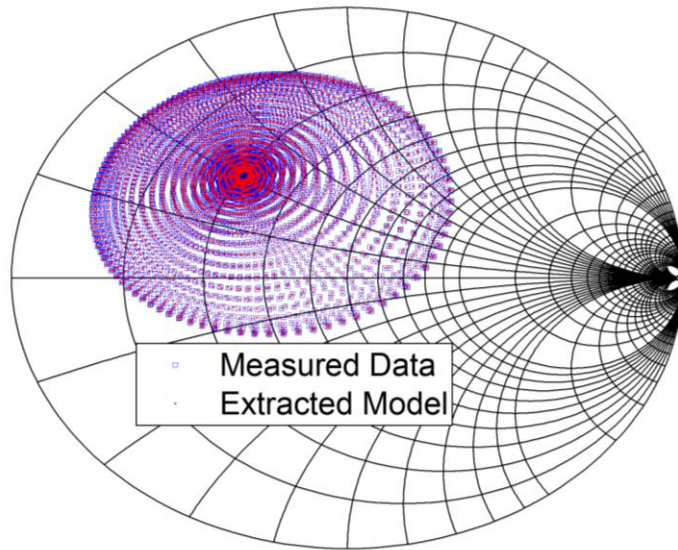


(a) Gamma load comparisons for measured and modelled data.

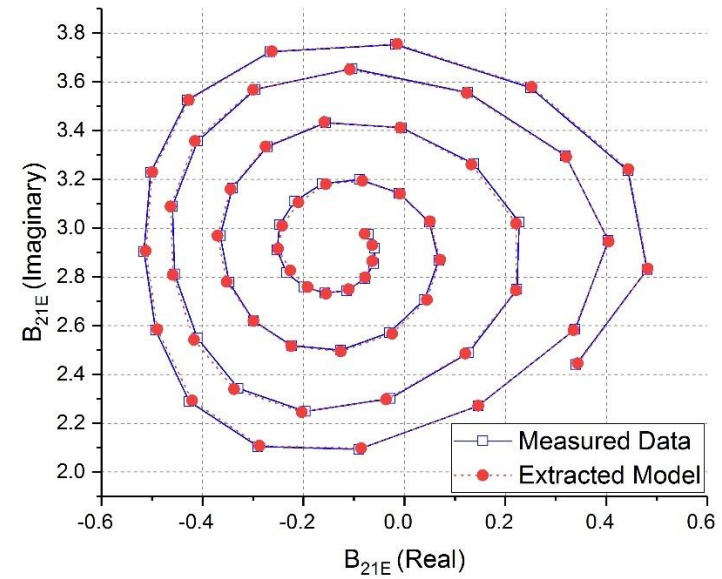


(b)  $B_{2,1}^E(t)$  comparison for measured and modelled data.

Figure 5-25: Comparison for measured and modelled data with phase modulated tone = -8dBc.



(a) Gamma load comparisons for measured and modelled data.



(b)  $B_{2,1}^E(t)$  comparison for measured and modelled data.

Figure 5-26: Comparison for measured and modelled data with phase modulated tone = -6dBc

Now concerning the case when the phase modulated tone equals -4dBc. Figure 5-27 highlights that in this case, more mixing terms can be identified, hence the need for a more complex (10 coefficients) Cardiff Model. Once identified, the model coefficients are then again determined using the matrix equation defined in the envelope domain to exploit the diagonal nature of the  $F_{m,n}^E(t)$  matrix to provide for model coefficient extraction rather than fitting.

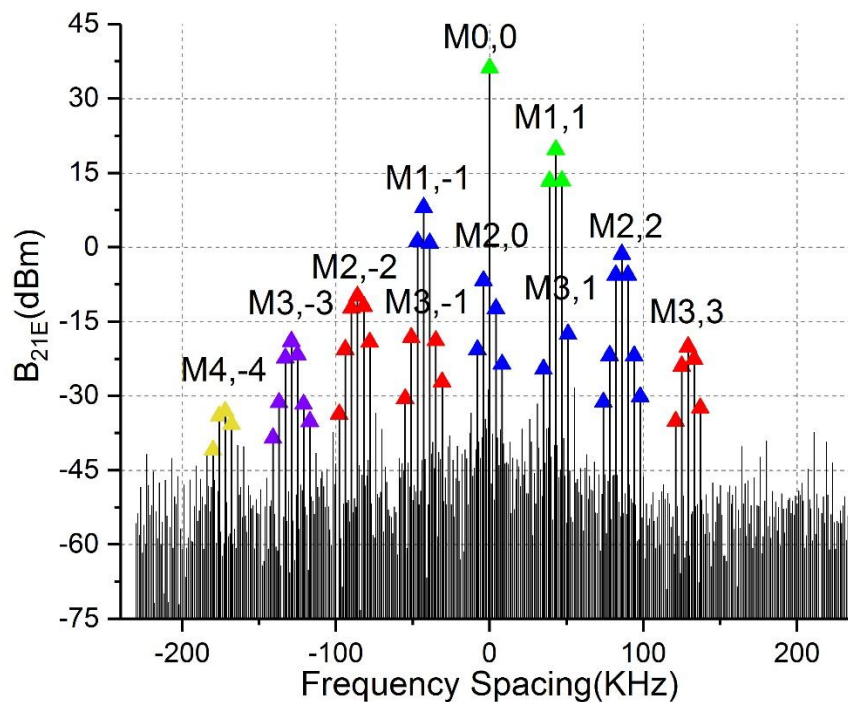


Figure 5-27:  $B_{2,1}^E$  spectrum showing 9<sup>th</sup> order coefficients for phase modulated tone = -4dBc.

It should be highlighted that each colour denotes a specific order in the model. For instance, green refers to the 1<sup>st</sup> order, blue indicates 3<sup>rd</sup> order, and red indicates 5<sup>th</sup> order while purple denotes 7<sup>th</sup> order, finally, yellow refers to the 9<sup>th</sup> order. Note the terms  $M_{4,-4}$  is just above the noise floor and so give only a small contribution and so have not been included in the model.

Figure 5-28 shows how the load-pull area on the Smith Chart has been significantly increased. Also shown are the measured and modelled load points. Figure 5-29 shows the load-pull contours and how they are matched to the optimum load of CW measurements as mentioned earlier in chapter 3.

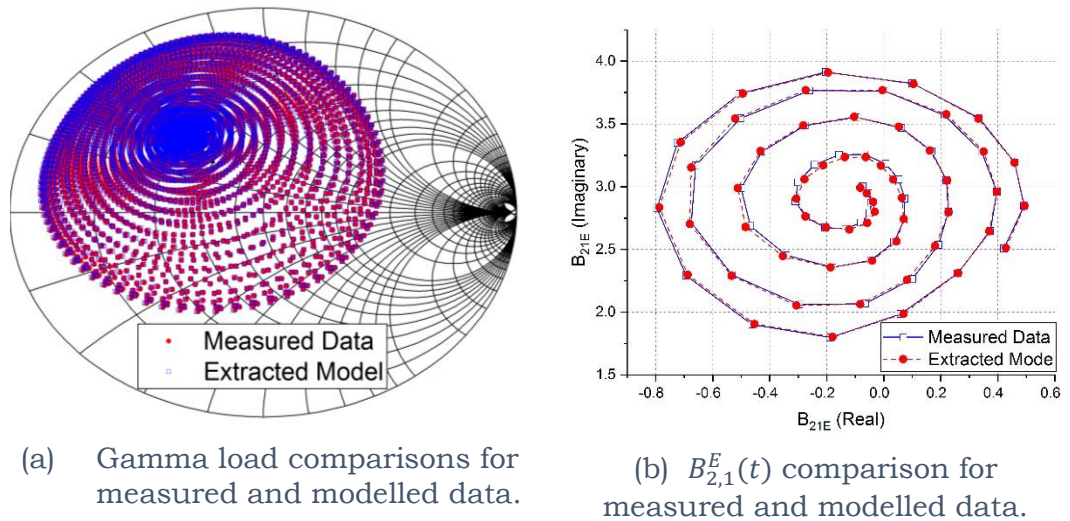


Figure 5-28: Comparison for modelled and measured phase modulated signal=-4dBc with NMSE= -41.99dB.

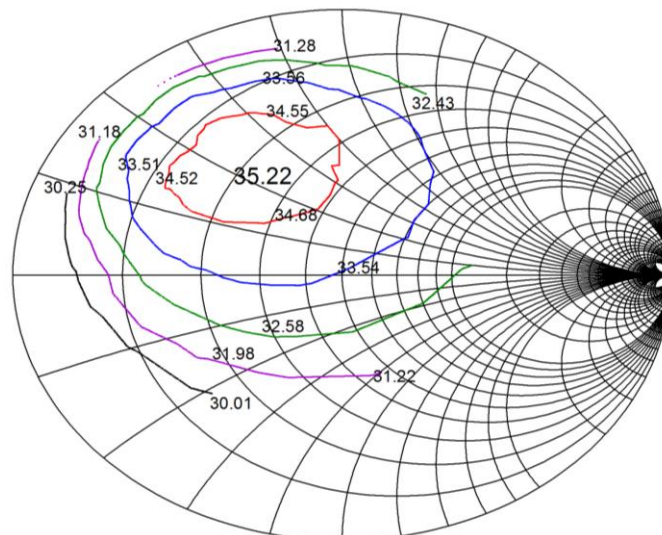


Figure 5-29: Power contours for phase modulated tone of -4dBc.

---

## 5.7 CHAPTER SUMMARY

A new technique, exploiting two-tone measurements, for the correct determination of Cardiff Model phase coefficients has been introduced. Using this technique, to utilize phase modulated tone ( $a_{21,2}$ ) with the main-tone ( $a_{21,1}$ ), and the FFT were able to explore the mixing term above the noise floor which allows to move from the phase domain to the frequency domain. The amplitude offset between the phase modulated tone and the main tone causes the asymmetry between the tones which makes some mixing terms appear while others are below the noise floor. Seven measurements ( $|a_{21,2}| = -6\text{dBc}$  to  $+6\text{dBc}$ ) were done for different  $|a_{21,2}|$  power offset. By increasing the offset power level  $|a_{21,2}|$ , more terms appeared, which indicated the need for a more complex model.

The analytical X-parameter model formulation has been shown to remain accurate until  $|a_{21,2}| = 2\text{dBc}$ . However, higher order formulations are required for better accuracy with increasing  $|a_{21,2}|$  power levels. The  $|a_{21,2}|$  perturbation has been increased to cover a substantial area of the Smith Chart and is accurately modelled by an 11<sup>th</sup> order phase polynomial. This approach allows for the maximum model complexity to be identified directly from measurements, hence allowing for the direct extraction of both the maximum model order as well as the associated coefficients.

---

Using impedance targets obtained from the two-tone measurements, the model analysis was performed for CW measurements over the same area in the Smith Chart and shows that the model identification can directly be applied to CW measurements for accurate models (NMSE < 40dB). When extending from contours of fixed amplitude to areas involving both mag and phase variation, it can be observed that new magnitude mixing terms, that share the same phase location, but have a different magnitude dependency need to be included. Since the magnitude terms are superimposed on the phase terms, this makes it difficult to differentiate both terms during model extraction.

Therefore, a new novel approach was utilized to perturb the load with extra two-tones (AM-modulation) around the phase-modulated tone. This allowed for the observation of the magnitude and phase mixing terms separately. This approach provides the determination of the required Cardiff Model complexity directly from measured data. The approach exploits the fact that the multi-tone measurements support the Fourier Transformation of the measured envelope time domain data into the envelope frequency domain. The engineered multi-tone stimulus ensures that the resulting spectra of the  $B_{2,1}^E(t)$  signal, allows for the identification of the necessary model terms along with the direct extraction of the model coefficients.

Four different measurements were performed, starting with a phase modulated signal of magnitude -10dBc from the main tone and ending at -4dBc from the main tone. For each measurement, the model complexity and its related model coefficients were shown. In addition, this chapter uses the NMSE metric to analyse the accuracy of the model extraction for each measurement and how the load-pull measured area affects the NMSE. The extracted model for phase modulated signal equals -10dBc has been shown to accurately model the measured load-pull data with an NMSE of -49.21dB. In addition, exploiting FFT in LMS extraction process provides a very robust, direct extraction, solution for model coefficient determination. Finally, the capability of the measurement system with a dynamic range of more than 80dB, for 4 kHz spacing, allows for the observation of more model terms above the noise floor.

## REFERENCES

1. Kurokawa, K., *Power Waves and the Scattering Matrix*. IEEE Transactions on Microwave Theory and Techniques, 1965. **13**(2): p. 194-202.
2. Root, D., *Polyharmonic distortion modeling*. IEEE microwave magazine, 2006. **7**(3): p. 44-57.
3. Root, D., et al., X-parameters: The new paradigm for measurement, modeling, and design of nonlinear RF and microwave components. Microwave Engineering Europe, 2008(12): p. 16.
4. Woodington, S., et al. Behavioral model analysis of active harmonic load-pull measurements. in 2010 IEEE MTT-S International Microwave Symposium. 2010. IEEE.
5. Bell, J., et al. Behavioral model analysis using simultaneous active fundamental load-pull and harmonic source-pull measurements at X-band. in Microwave Symposium Digest (MTT), 2011 IEEE MTT-S International. 2011. IEEE.
6. Wisell, D. and M. Isaksson. Derivation of a behavioral RF power amplifier model with low normalized mean-square error. in Microwave Conference, 2007. European. 2007. IEEE.
7. Hussein, T., et al. Automating the Accurate Extraction and Verification of the Cardiff Model via the Direct Measurement of Load-Pull Power Contours. in 2018 IEEE/MTT-S International Microwave Symposium-IMS. 2018. IEEE.
8. Moure, M.R., et al. Direct extraction of an admittance domain behavioral model from large-signal load-pull measurements. in 2017 IEEE MTT-S International Microwave Symposium (IMS). 2017.

---

## CHAPTER 6

### CONCLUSION AND FUTURE WORK

#### 6.1 CONCLUSION

The objectives of this thesis have been successfully achieved. It extends the capability of an accurate high-speed load-pull system for CW measurements, based on PXI components to encompass multi-tone excitation as well. The realised measurement system with high dynamic range was used for the first time to perform time-varying load-pull measurements to advance the extraction of the Cardiff Behavioural model from these load-pull measurements. A multi-tone stimulus using a combination of phase and amplitude modulation allows for the model coefficients to be directly extracted from the measured data avoiding the need for “curve-fitting”. In addition, the multi-tone capability was utilised to provide for the direct extraction of device S-parameters and the system source impedance data in real time during load-pull measurements. By computing the input reflection coefficient ( $\Gamma_{in}$ ) using small-signal measurements helped to validate the stability analysis and provide information for further analysis. Also, calculating “Ts” aids the computation of  $G_A$  and  $G_T$  with no extra cost. The following paragraphs describe the conclusions, chapter-by-chapter, in more detail.

Chapter 2 has reviewed the evolution of RF measurements techniques started from linear measurements to the non-linear world (such as NVNA) where the harmonics are considered under the large signal stimulus. Later, this breakthrough was useful to be used in load-pull systems for CW measurements. Moving forward, the development in load-pull measurement systems under multi-tone or modulated signals is presented showing the usefulness and limitation in RF applications. At last, a brief description of the PXIe modules-based measurement system was included. It showed the capability of having high-speed and accurate RF measurements for CW measurements, which later shows the attitude to extend the work to develop the system for multi-tone measurements.

Chapter 3 highlighted the importance of ensuring the correct triggering and phase alignment of such a system and the need to calibrate over the modulation bandwidth. Phase alignment is essential for the generation and measurement of the used defined multi-tone stimulus. Over large modulation band widths, it was shown that assuming the error coefficient was constant results in an erroneous measured and incorrect measurement of load-pull contours. This was resolved by calibration across the modulation bandwidth.

---

Two examples of the use of the multi-tone capability linked to fundamental load-pull were developed. In chapter 3, the multi-tone capability was utilised to provide for the direct extraction of device S-parameters and the system source impedance data in real time during load-pull measurements. This was done via the inclusion of two tickle-tones with different offset frequencies. Studies were undertaken to determine the necessary tone spacing and the power level of the tickle-tones with regards to the main tone required to allow for the accurate determination of this additional information without distorting the fundamental large signal measurements. It shows that the tickle tone can be set to -20dBc (from the main tone), which is considered optimal for extracting accurate data. By computing the input reflection coefficient ( $\Gamma_{in}$ ) using small-signal measurements helped to validate the stability analysis and provide information for further analysis. Also, calculating  $\Gamma_s$  aids the computation of  $G_A$  and  $G_T$  with no extra cost as the dynamic range of the measurement system is high which set the tickle tone at different power offsets. The chapter ends with displaying the unstable area on the Smith Chart while presenting different load and different power level inputs to the DUT.

---

In chapter 5 the multi-tone capability was used to perform time-varying load-pull measurements. A key focus was the selection of these time-varying load-pull multi-tone stimulus to advance the extraction of the Cardiff Behavioural model from these load-pull measurements. Initially, the correct determination of the Cardiff Model phase coefficients by exploiting two-tone measurements was investigated. This approach utilizing phase modulated tone ( $a_{21,2}$ ) with the main tone ( $a_{21,1}$ ), and the FFT to detect the mixing term above the noise floor. Several measurements ( $|a_{21,2}| = -6\text{dBc}$  to  $+6\text{dBc}$ ) have been performed to observe more terms which means the more complex model is required. The analytical X-parameter model formulation has been used for comparison with the Cardiff model which shows accurate results until  $|a_{21,2}| = 2\text{dBc}$ , small coverage of the Smith Chart. Measurements confirmed that higher order polynomial calculation is required for better accuracy with increasing  $|a_{21,2}|$  power levels, large coverage of the Smith Chart. The  $|a_{21,2}|$  perturbation set to  $+6\text{dBc}$  which covers a substantial area of the Smith Chart, accurate modelled necessitates an 11<sup>th</sup> order phase polynomial.

The impedance loads obtained from the two-tone measurements have been used as a target for CW measurements over the same area in the Smith Chart. This verification shows that the model identification can directly be applied to CW measurements for accurate models when  $\text{NMSE} < 40\text{dB}$ .

---

Despite presenting an accurate approach of identifying the Cardiff Model phase coefficients, it is still problematic to differentiate the magnitude mixing terms above the noise floor as the magnitude and phase mixing terms share the same phase location, and their magnitude dependency is different. Therefore, a new novel approach has been successfully applied to perturb the load with four tones (Involving carrier phase and amplitude modulation component) to observe the magnitude and phase mixing term separately. The realised technique provides identification of the required Cardiff Model complexity directly from measured data. The engineered multi-tone stimulus ensures that no interference of the resulting spectra of the  $B_{2,1}^E(t)$  the signal occurred, which allows to identify the necessary model terms along with the direct extraction of the model coefficients. The performed model for phase modulated signal =-10dBc shows good agreement between the modelled and the measured load-pull data with NMSE =-49.21dB. Finally, utilising FFT in LMS extraction process, provides a very robust, direct extraction, solution for model coefficient determination where the  $F_{m,n}^E$  matrix has a diagonal structure; therefore, the model coefficient terms can be extracted individually.

---

## 6.2 FUTURE WORK

While the aim in this thesis to develop high speed and accurate measurement system, based on PXIe module to generate and receive multi-tone signals has been achieved, further work is still required to fully optimise the LabVIEW code and add more functionality to achieve better performance and cover the end-user requirements. This section is set to offer some suggestions to upgrade the work as follow:

- The work in chapter 5 was based on fundamental load-pull, however, the concept presented could be extended the work also at the second harmonic. For example, controlling the second harmonic stimulus while setting the perturbation load of the second harmonic ( $a_{22}$ ) with different frequency spacing. This approach would give more insight about the mixing terms identification such as  $(2\omega_2 - \omega_1)$ ,  $(2\omega_1 - \omega_2)$ ,  $(3\omega_2 - 2\omega_1)$  and  $(2\omega_2 - 3\omega_1)$  etc. On the other hand, having a second harmonic data with DC as well, would allow to have a complete set of data to be used in CAD software for RF designers.
  
- Moreover, having a flexible and expandable system presented in terms of software and the hardware would allow for further development, such as a multi-tone load-pull to investigate the linearity of high-power amplifiers through analysing IMD products.

- The work about the stability analysis in chapter 3 can be extended further using the same condition with the same device model in CAD simulation to be compared with the extracted measured data in active load-pull measurement. It is a sanity check, which is ultimately important for RF designers.
  
- Although the instantaneous bandwidth of the Receiver (the bandwidth of the ADC) =50MHz, the work in this thesis has utilised the bandwidth between (-500 to +500) KHz. This gives a chance to extend the work to check the memory effects to include the whole receiver bandwidth. 'Memory' refers here to a dynamic dispersion of the device characteristics, which can be observed as a function of signal bandwidth. It becomes difficult to meet the required linear PA. Memory effects are considered the main burden in the design of highly linear power amplifiers in wireless communication systems.

## APPENDIX A

### PRESENTING THE MEASUREMENT SYSTEM'S SOFTWARE

The software of the realised measurement system should be run first by the LabVIEW project. Next, go running Master UI folder, which then ends up to EDITED LoadPull GUI.vi as shown in figure A.1.

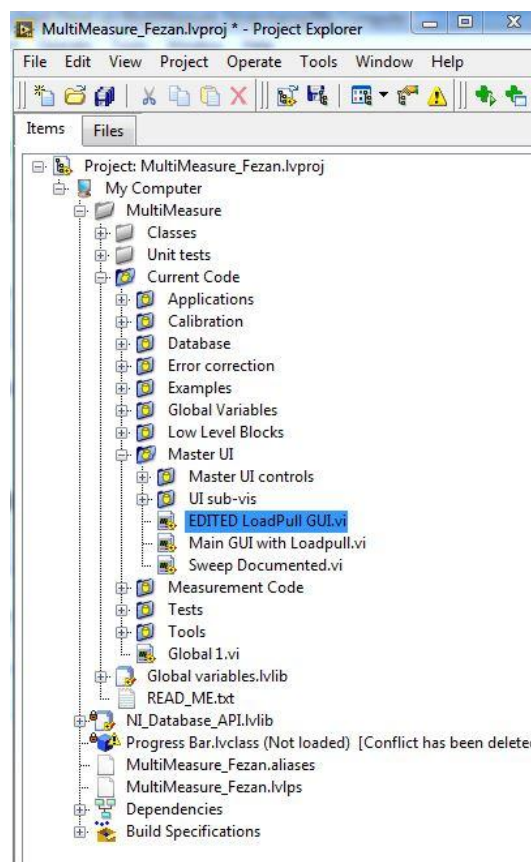


Figure A-1: project menu of the realised measurement system

The main GUI (Graphical user interface), as shown below, has different options to go, for instance, the calibration manager, CW load-pull, multi-tone load-pull, and the DC control. The work in this thesis demonstrates on multi-tone load-pull option.

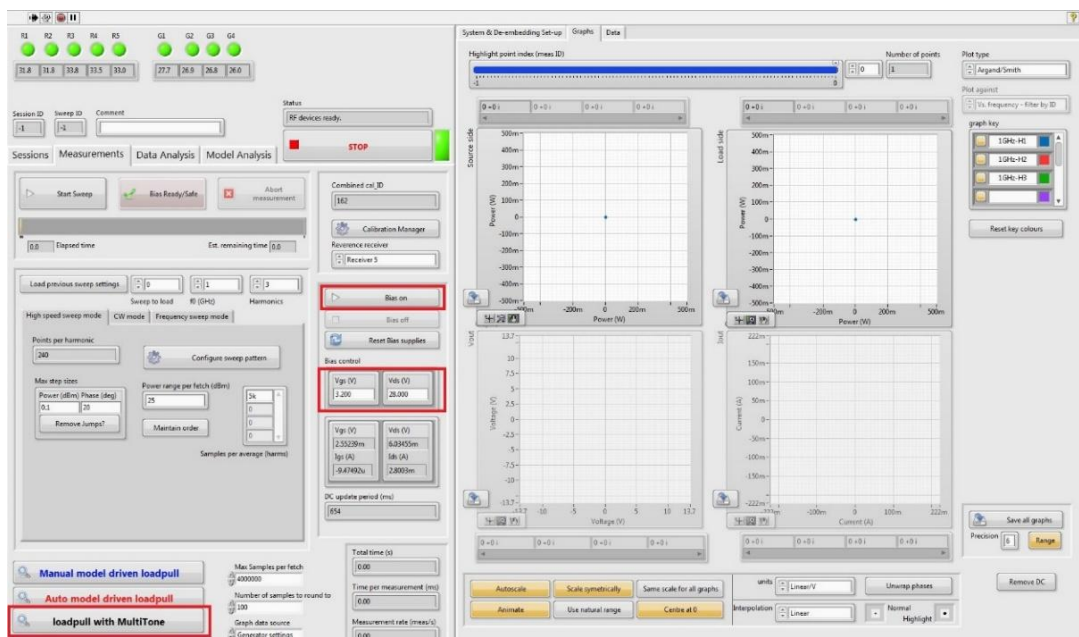


Figure A-2: The main GUI of the measurement software

Figure A-3 provides the end-user with several graphs settings for both the main-tone and multi-tone and for both the generators and the receivers. As can be seen, the carrier frequency of the generator and the centre frequency of the receiver are both set to 1GHz. Also, the duration time which is used to define the number of samples after multiplying with the sampling frequency. To generate the multi-tone, an array is used with providing the frequency, amplitude (dBm) and the phase for each tone.

The first index is dedicated to defining the main tone while others are used according to the number of utilised tones. Here, the second tone is turned off which means it is set to -150 dBm.

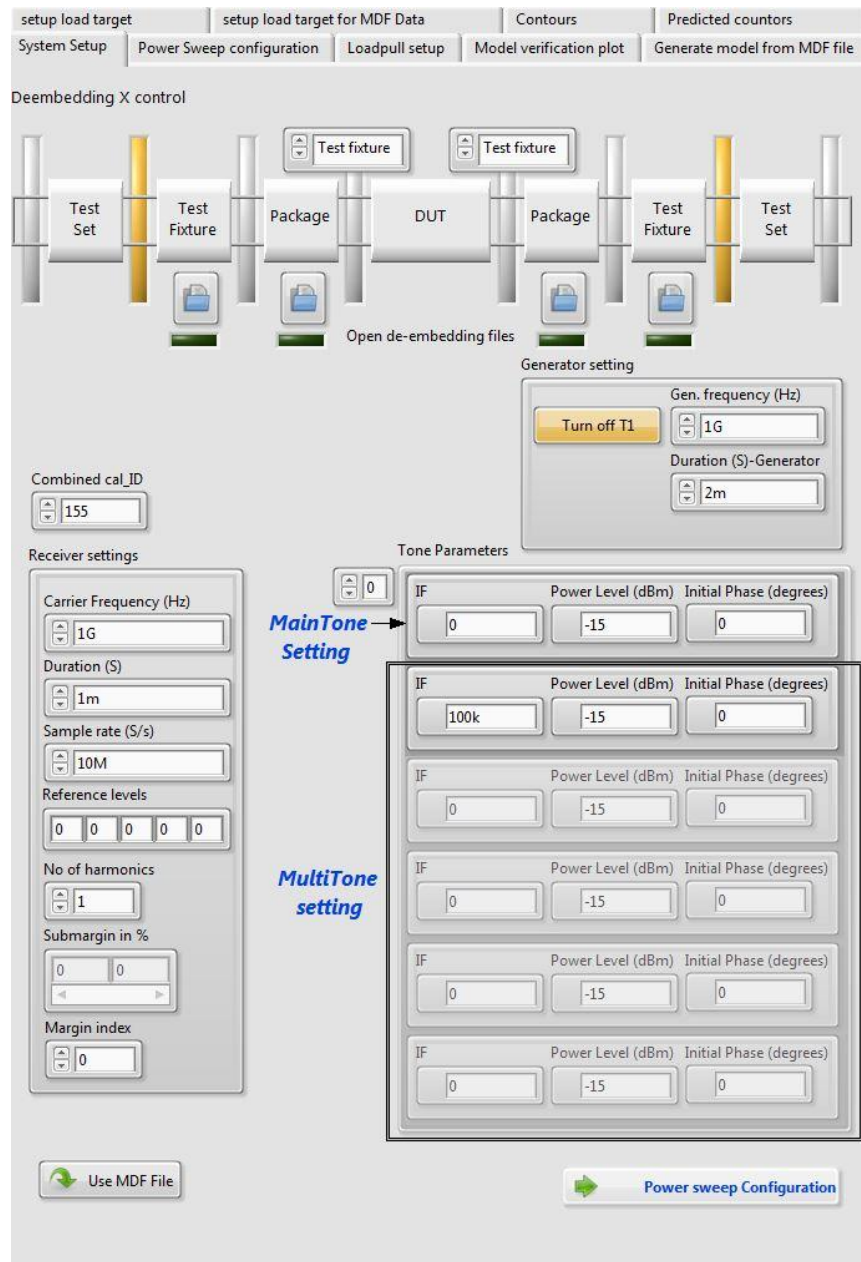


Figure A-3: The front panel of the multi-tone load-pull measurements software.



The following step is defining the impedances grid shape and the range of the  $a_{21}$  to be used in the initial load-pull measurement as shown below.

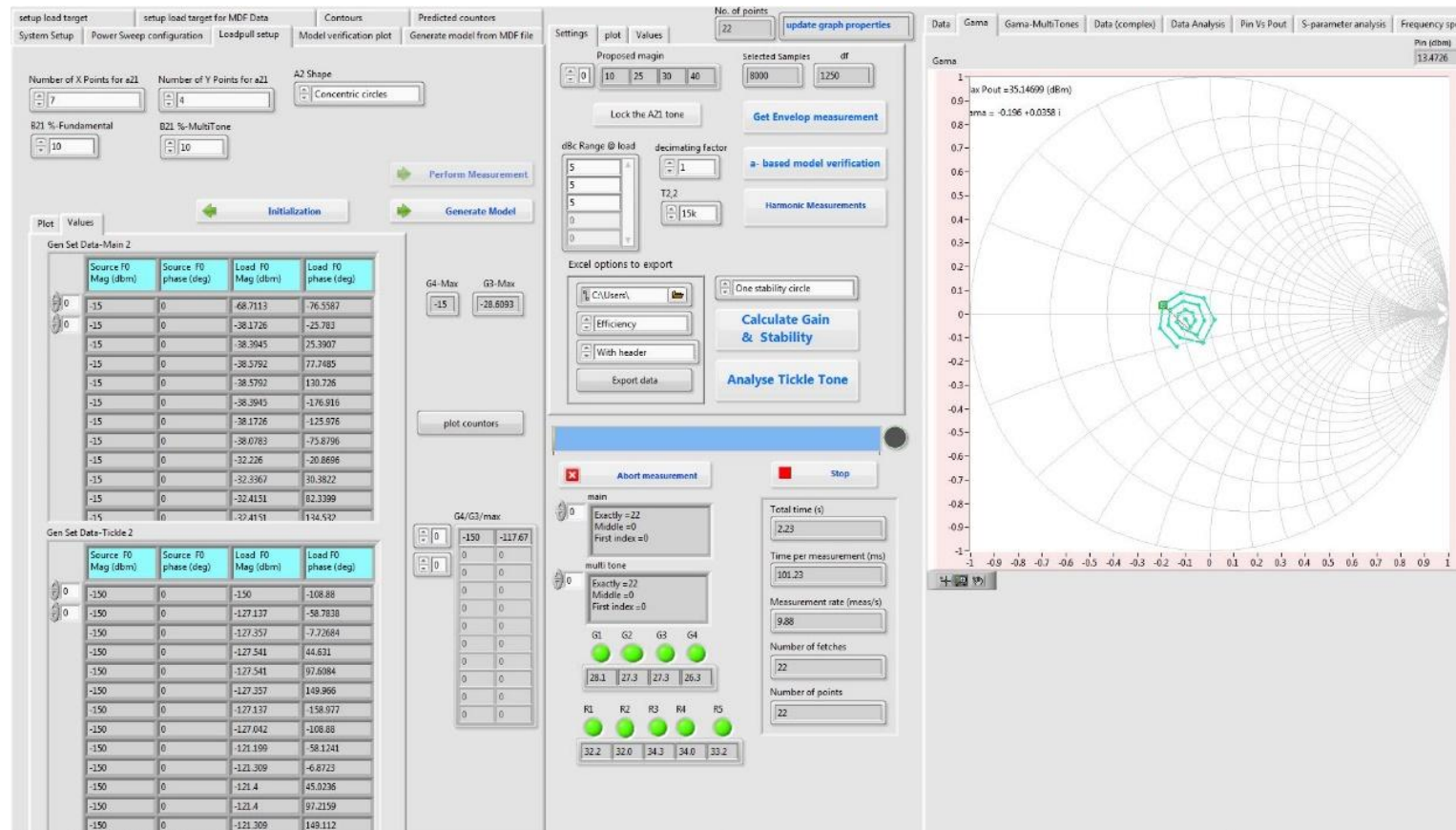


Figure A-5: Initial load-pull measurements around 50 Ohm.

Figure A-6 shows an open window to select the required exponents of magnitude and phase followed by model verification for both the measured data and the extracted model. Here, the NMSE metric is presented as an indication of the accuracy between  $b_{21}$  predicted and  $b_{21}$  measured. An option is provided to regenerate the model in case more accuracy is required for a different set of magnitude and phase exponents.

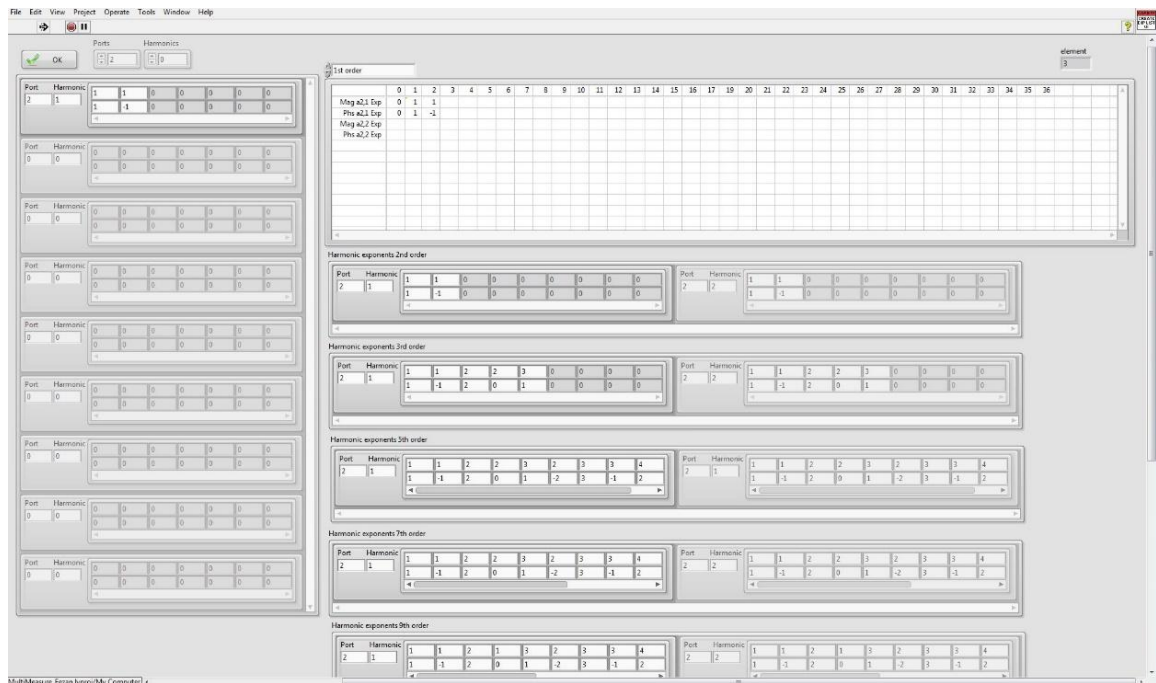


Figure A-6: Model's exponent matrix generator

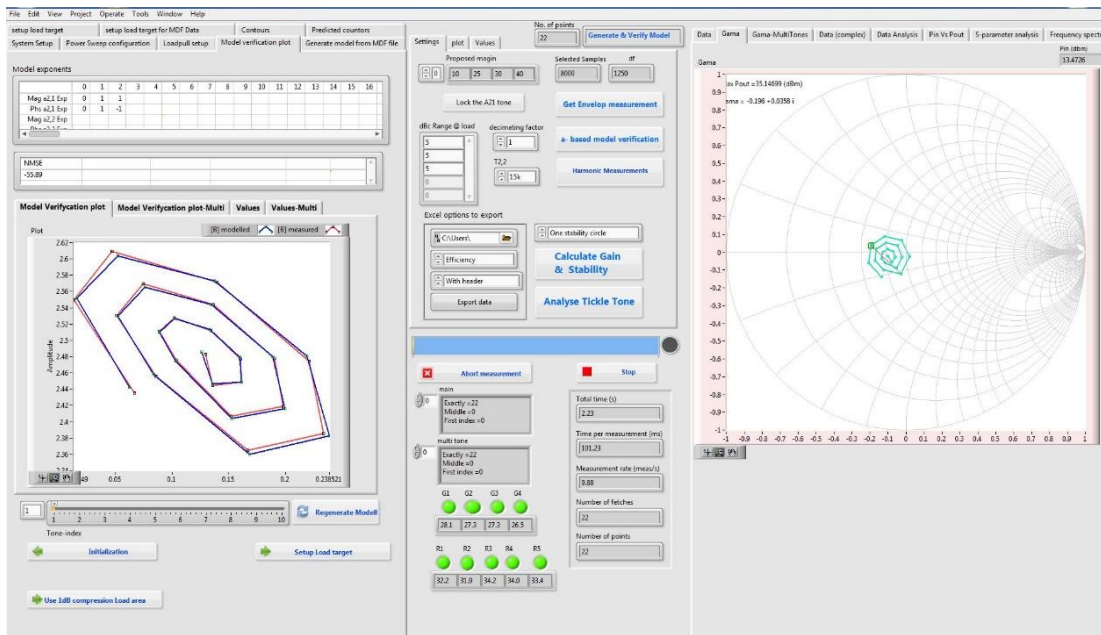


Figure A-7: Comparison between measured and modelled data.

The initial load-pull measurement was set around the 50 Ohm, after that the load-based model is employed to track the optimum load<sup>1</sup>. Setting the load targets for the next load-pull measurement is shown in figure A.8. Several options are provided to set the next load-pull setup for the main tone and the multi-tone as well. It is worth mentioning that the second-harmonic load-pull setting is existing in this code, but extra verifications are needed to approve it.

<sup>1</sup> More details can be found in Al-Husseini's thesis

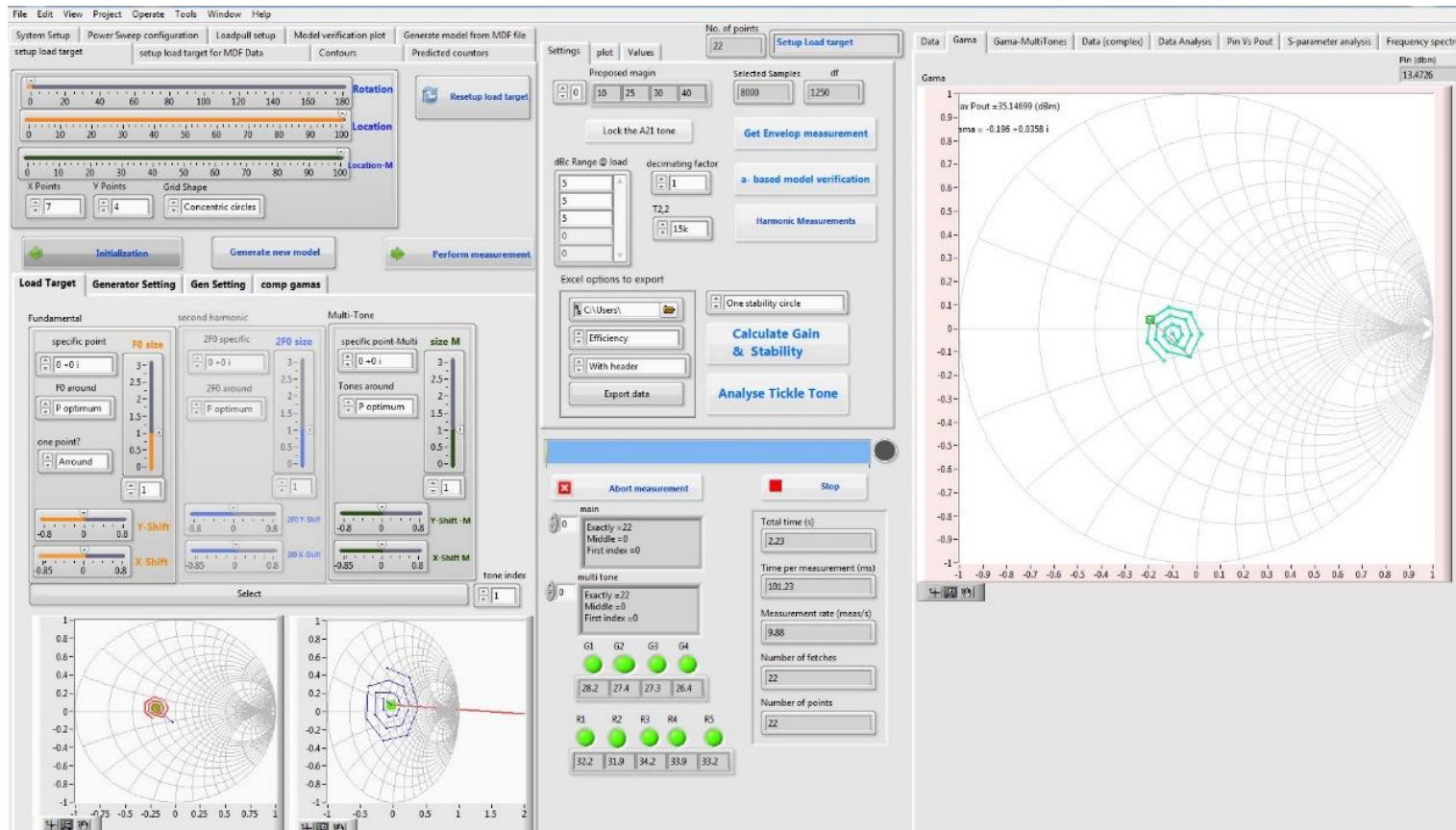


Figure A-8: fundamental load-pull targets set-up.

Figure A-9 shows the next step of the implemented load-pull measurement on the right while the comparison between  $\Gamma_{load}$  of measured and modelled data is shown on the left.

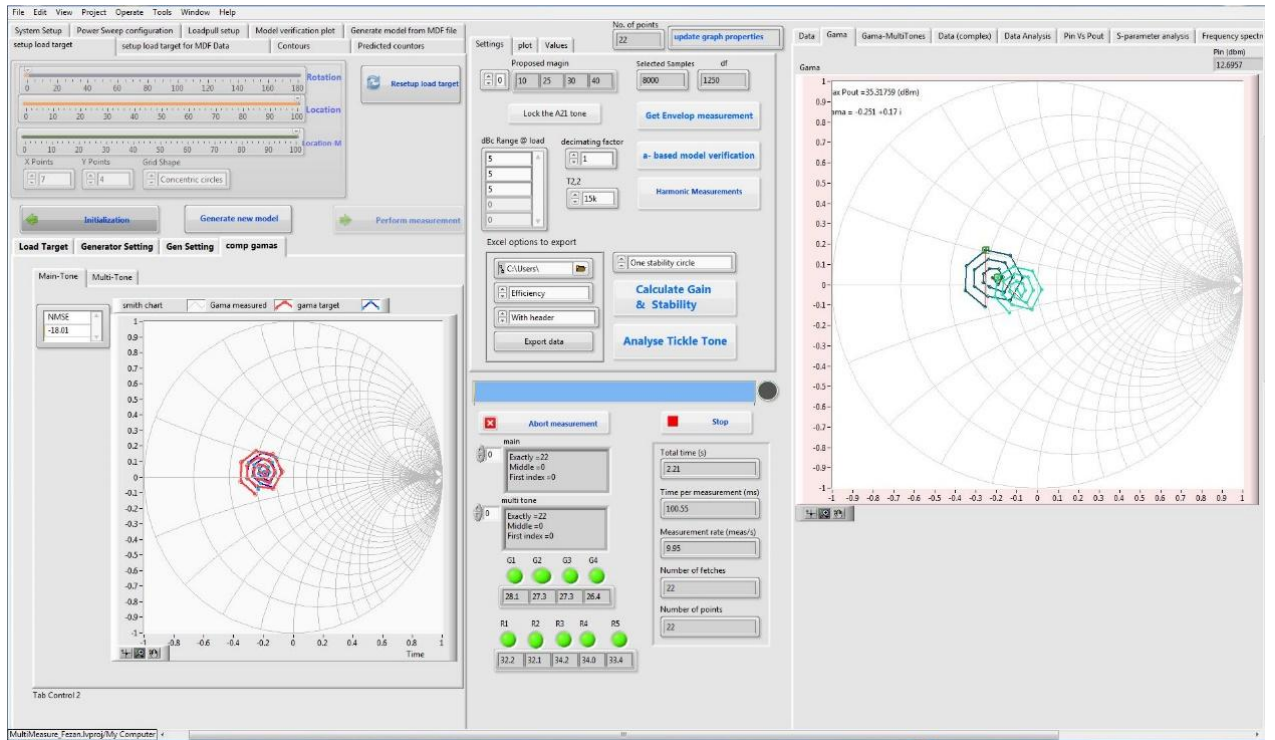


Figure A-9: The resultant load-pull measurement of the next step.

## APPENDIX B

### Two-Tone Trigonometric Equations

$$V_1(t) = A_1 \cos(2\pi f_1 t), \quad V_2(t) = A_2 \cos(2\pi f_2 t),$$

$$V(t) = V_1 + V_2 = A_1 \cos(\omega_1 t) + A_2 \cos(\omega_2 t),$$

$$B_{p,h} = \sum_{n=0}^n a_n v^n(t) = a_0 + a_1 v(t) + a_2 v^2(t) + a_3 v^3(t) + \dots + a_n v^n(t)$$

$$= a_0 + a_1 [A_1 \cos(\omega_1 t) + A_2 \cos(\omega_2 t)]$$

$$+ a_2 [A_1 \cos(\omega_1 t) + A_2 \cos(\omega_2 t)]^2$$

$$+ a_3 [A_1 \cos(\omega_1 t) + A_2 \cos(\omega_2 t)]^3$$

$$+ a_4 [A_1 \cos(\omega_1 t) + A_2 \cos(\omega_2 t)]^4$$

$$+ a_5 [A_1 \cos(\omega_1 t) + A_2 \cos(\omega_2 t)]^5$$

#### Some Trigonometric Identities

$$\cos^2 X = \frac{1 + \cos 2x}{2}$$

$$\cos \alpha \cos \beta = \frac{\cos(\alpha - \beta) + \cos(\alpha + \beta)}{2}$$

$$\cos^3 X = \frac{3\cos x + \cos 3x}{4}$$

$$\text{For } a_2 [A_1 \cos(\omega_1 t) + A_2 \cos(\omega_2 t)]^2 = a_2 A_1^2 \cos^2(\omega_1 t) + a_2 2 A_1 A_2 \cos(\omega_2 t) \cos(\omega_1 t) + a_2 A_2^2 \cos^2(\omega_2 t)$$

$$= a_2 \frac{A_1^2}{2} + \frac{A_1^2}{2} \cos(2\omega_1 t) + a_2 [A_1 A_2 \cos(\omega_1 t - \omega_2 t) + A_1 A_2 \cos(\omega_2 t + \omega_1 t)] + a_2 \frac{A_2^2}{2} + \frac{A_2^2}{2} \cos(2\omega_2 t)$$

$$= \frac{1}{2} a_2 (A_1^2 + A_1^2 \cos(2\omega_1 t)) + 2 A_1 A_2 \cos(\omega_1 t - \omega_2 t) + 2 A_1 A_2 \cos(\omega_2 t + \omega_1 t) + A_2^2 + A_2^2 \cos(2\omega_2 t)$$

For  $a_3[A_1 \cos(\omega_1 t) + A_2 \cos(\omega_2 t)]^3$

$$= A_1^3 \cos^3(\omega_1 t) + 3 A_1^2 A_2 \cos^2(\omega_1 t) \cos(\omega_2 t) + 3 A_1 A_2^2 \cos(\omega_1 t) \cos^2(\omega_2 t) + A_2^3 \cos^3(\omega_2 t)$$

$$= \frac{1}{4} (A_1^3 \cos(3\omega_1 t) + 3 A_1^3 \cos(\omega_1 t)) + 3 A_2 \cos(\omega_2 t) \left( \frac{1}{2} A_1^2 + \frac{1}{2} A_1^2 \cos(2\omega_1 t) \right) + 3 A_1 \cos(\omega_1 t) \left( \frac{1}{2} A_2^2 + \frac{1}{2} A_2^2 \cos(2\omega_2 t) \right) + \frac{1}{4} (A_2^3 \cos(3\omega_2 t) + 3 A_2^3 \cos(\omega_2 t))$$

$$= \frac{1}{4} (A_1^3 \cos(3\omega_1 t) + 3 A_1^3 \cos(\omega_1 t)) + \frac{3}{2} A_1^2 A_2 \cos(\omega_2 t) + \frac{3}{2} A_1^2 A_2 \cos(2\omega_1 t) \cos(\omega_2 t) + \frac{3}{2} A_1 A_2^2 \cos(\omega_1 t) + \frac{3}{2} A_2^2 A_1 \cos(2\omega_2 t) \cos(\omega_1 t) + \frac{1}{4} (A_2^3 \cos(3\omega_2 t) + 3 A_2^3 \cos(\omega_2 t))$$

$$= \frac{1}{4} A_1^3 \cos(3\omega_1 t) + \frac{3}{4} A_1^3 \cos(\omega_1 t) + \frac{3}{2} A_1^2 A_2 \cos(\omega_2 t) + \frac{3}{4} A_1^2 A_2 (\cos(2\omega_1 t - \omega_2 t) + \cos(2\omega_1 t + \omega_2 t)) + \frac{3}{2} A_2^2 A_1 \cos(\omega_1 t) + \frac{3}{4} A_2^2 A_1 (\cos(2\omega_2 t - \omega_1 t) + \cos(2\omega_2 t + \omega_1 t)) + \frac{1}{4} A_2^3 \cos(3\omega_2 t) + \frac{3}{4} A_2^3 \cos(\omega_2 t)$$

$$= \frac{1}{4} a_3 [A_1^3 \cos(3\omega_1 t) + 9 A_1^3 \cos(\omega_1 t) + 3 A_1^2 A_2 \cos(2\omega_1 t - \omega_2 t) + 3 A_1^2 A_2 \cos(2\omega_1 t + \omega_2 t) + 3 A_1^2 A_2 \cos(2\omega_2 t - \omega_1 t) + 3 A_1^2 A_2 \cos(2\omega_2 t + \omega_1 t) + A_2^3 \cos(3\omega_2 t) + 9 A_2^3 \cos(\omega_2 t)]$$

**Some Useful tips**

$$\frac{a}{b} - \frac{c}{d} = \left( \frac{a}{b} \times \frac{d}{d} \right) - \left( \frac{c}{d} \times \frac{b}{b} \right) = \frac{ad - bc}{bd}$$

For  $a_5[A_1 \cos(\omega_1 t) + A_2 \cos(\omega_2 t)]^5$

$$A_1^5 \cos^5(\omega_1 t) + 5 A_1^4 A_2 \cos^4(\omega_1 t) \cos(\omega_2 t) + 5 A_1 A_2^4 \cos(\omega_1 t) \cos^4(\omega_2 t) + 10 A_1^3 A_2^2 \cos^3(\omega_1 t) \cos^2(\omega_2 t) + 10 A_1^2 A_2^3 \cos^2(\omega_1 t) \cos^3(\omega_2 t) + A_2^5 \cos^5(\omega_2 t)$$

$$\frac{1}{16} (10 A_1^5 \cos(\omega_1 t) + 5 A_1^5 \cos(3 \omega_1 t) + A_1^5 \cos(5 \omega_1 t)) = \frac{10}{16} A_1^5 \cos(\omega_1 t) + \frac{5}{16} A_1^5 \cos(3 \omega_1 t) + \frac{1}{16} A_1^5 \cos(5 \omega_1 t)$$

$$+ 5 A_2 \cos(\omega_2 t) \left[ \frac{1}{8} (4 A_1^4 \cos(2 \omega_1 t) + A_1^4 \cos(4 \omega_1 t) + 3 A_1^4) \right]$$

$$= 5 A_2 \cos(\omega_2 t) \left[ \frac{4}{8} A_1^4 \cos(2 \omega_1 t) + \frac{1}{8} A_1^4 \cos(4 \omega_1 t) + \frac{3}{8} A_1^4 \right]$$

$$= \frac{20}{8} A_1^4 A_2 \cos(2 \omega_1 t) \cos(\omega_2 t) + \frac{5}{8} A_1^4 A_2 \cos(4 \omega_1 t) \cos(\omega_2 t) + \frac{15}{8} A_1^4 A_2 \cos(\omega_2 t)$$

$$= \frac{20}{16} A_1^4 A_2 \cos(2 \omega_1 t - \omega_2 t) + \frac{20}{16} A_1^4 A_2 \cos(2 \omega_1 t + \omega_2 t) + \frac{5}{16} A_1^4 A_2 \cos(4 \omega_1 t - \omega_2 t) + \frac{5}{16} A_1^4 A_2 \cos(4 \omega_1 t + \omega_2 t) + \frac{15}{8} A_1^4 A_2 \cos(\omega_2 t)$$

$$+ 5 A_1 \cos(\omega_1 t) \left[ \frac{1}{8} (4 A_2^4 \cos(2 \omega_2 t) + A_2^4 \cos(4 \omega_2 t) + 3 A_2^4) \right] = 5 A_1 \cos(\omega_1 t) \left[ \frac{4}{8} A_2^4 \cos(2 \omega_2 t) + \frac{1}{8} A_2^4 \cos(4 \omega_2 t) + \frac{3}{8} A_2^4 \right]$$

$$= \frac{20}{8} A_2^4 A_1 \cos(2 \omega_2 t) \cos(\omega_1 t) + \frac{5}{8} A_2^4 A_1 \cos(4 \omega_2 t) \cos(\omega_1 t) + \frac{15}{8} A_2^4 A_1 \cos(\omega_1 t)$$

$$= \frac{20}{16} A_2^4 A_1 \cos(2 \omega_2 t - \omega_1 t) + \frac{20}{16} A_2^4 A_1 \cos(2 \omega_2 t + \omega_1 t) + \frac{5}{16} A_2^4 A_1 \cos(4 \omega_2 t - \omega_1 t) + \frac{5}{16} A_2^4 A_1 \cos(4 \omega_2 t + \omega_1 t) + \frac{15}{8} A_2^4 A_1 \cos(\omega_1 t)$$

Continue with 5<sup>th</sup> order .....

$$\begin{aligned}
 & +10 \mathbf{A}_1^3 \mathbf{A}_2^2 \cos^3(\omega_1 t) \cos^2(\omega_2 t) = 10 \left[ \left( \frac{1}{4} \mathbf{A}_1^3 \cos(3\omega_1 t) + \frac{3}{4} \mathbf{A}_1^3 \cos(\omega_1 t) \right) \left( \frac{1}{2} \mathbf{A}_2^2 + \frac{1}{2} \mathbf{A}_2^2 \cos(2\omega_2 t) \right) \right] \\
 & = 10 \left[ \frac{1}{8} \mathbf{A}_1^3 \mathbf{A}_2^2 \cos(3\omega_1 t) + \frac{1}{8} \mathbf{A}_1^3 \mathbf{A}_2^2 \cos(3\omega_1 t) \cos(2\omega_2 t) + \frac{3}{8} \mathbf{A}_1^3 \mathbf{A}_2^2 \cos(\omega_1 t) + \frac{3}{8} \mathbf{A}_1^3 \mathbf{A}_2^2 \cos(2\omega_2 t) \cos(\omega_1 t) \right] \\
 & = 10 \left[ \frac{1}{8} \mathbf{A}_1^3 \mathbf{A}_2^2 \cos(3\omega_1 t) + \frac{1}{16} \mathbf{A}_1^3 \mathbf{A}_2^2 \cos(3\omega_1 t - 2\omega_2 t) + \frac{1}{16} \mathbf{A}_1^3 \mathbf{A}_2^2 \cos(3\omega_1 t + 2\omega_2 t) + \frac{3}{8} \mathbf{A}_1^3 \mathbf{A}_2^2 \cos(\omega_1 t) + \frac{3}{16} \mathbf{A}_1^3 \mathbf{A}_2^2 \cos(2\omega_2 t - \omega_1 t) + \frac{3}{16} \mathbf{A}_1^3 \mathbf{A}_2^2 \cos(2\omega_2 t + \omega_1 t) \right] \\
 & = \frac{10}{8} \mathbf{A}_1^3 \mathbf{A}_2^2 \cos(3\omega_1 t) + \frac{10}{16} \mathbf{A}_1^3 \mathbf{A}_2^2 \cos(3\omega_1 t - 2\omega_2 t) + \frac{10}{16} \mathbf{A}_1^3 \mathbf{A}_2^2 \cos(3\omega_1 t + 2\omega_2 t) + \frac{30}{8} \mathbf{A}_1^3 \mathbf{A}_2^2 \cos(\omega_1 t) + \frac{30}{16} \mathbf{A}_1^3 \mathbf{A}_2^2 \cos(2\omega_2 t - \omega_1 t) + \frac{30}{16} \mathbf{A}_1^3 \mathbf{A}_2^2 \cos(2\omega_2 t + \omega_1 t)
 \end{aligned}$$

$$\begin{aligned}
 & + 10 \mathbf{A}_1^2 \mathbf{A}_2^3 \cos^2(\omega_1 t) \cos^3(\omega_2 t) = 10 \left[ \left( \frac{1}{2} \mathbf{A}_1^2 + \frac{1}{2} \mathbf{A}_1^2 \cos(2\omega_1 t) \right) \left( \frac{1}{4} \mathbf{A}_2^3 \cos(3\omega_2 t) + \frac{3}{4} \mathbf{A}_2^3 \cos(\omega_2 t) \right) \right] \\
 & = 10 \left[ \frac{1}{8} \mathbf{A}_1^2 \mathbf{A}_2^3 \cos(3\omega_2 t) + \frac{3}{8} \mathbf{A}_1^2 \mathbf{A}_2^3 \cos(\omega_2 t) + \frac{1}{8} \mathbf{A}_1^2 \mathbf{A}_2^3 \cos(3\omega_2 t) \cos(2\omega_1 t) + \frac{3}{8} \mathbf{A}_1^2 \mathbf{A}_2^3 \cos(2\omega_1 t) \cos(\omega_2 t) \right] \\
 & = 10 \left[ \frac{1}{8} \mathbf{A}_1^2 \mathbf{A}_2^3 \cos(3\omega_2 t) + \frac{3}{8} \mathbf{A}_1^2 \mathbf{A}_2^3 \cos(\omega_2 t) + \frac{1}{16} \mathbf{A}_1^2 \mathbf{A}_2^3 \cos(3\omega_2 t - 2\omega_1 t) + \frac{1}{16} \mathbf{A}_1^2 \mathbf{A}_2^3 \cos(3\omega_2 t + 2\omega_1 t) + \frac{3}{16} \mathbf{A}_1^2 \mathbf{A}_2^3 \cos(2\omega_1 t - \omega_2 t) + \frac{3}{16} \mathbf{A}_1^2 \mathbf{A}_2^3 \cos(2\omega_1 t + \omega_2 t) \right] \\
 & = \frac{10}{8} \mathbf{A}_1^2 \mathbf{A}_2^3 \cos(3\omega_2 t) + \frac{30}{8} \mathbf{A}_1^2 \mathbf{A}_2^3 \cos(\omega_2 t) + \frac{10}{16} \mathbf{A}_1^2 \mathbf{A}_2^3 \cos(3\omega_2 t - 2\omega_1 t) + \frac{10}{16} \mathbf{A}_1^2 \mathbf{A}_2^3 \cos(3\omega_2 t + 2\omega_1 t) + \frac{30}{16} \mathbf{A}_1^2 \mathbf{A}_2^3 \cos(2\omega_1 t - \omega_2 t) + \frac{30}{16} \mathbf{A}_1^2 \mathbf{A}_2^3 \cos(2\omega_1 t + \omega_2 t) \\
 & + \mathbf{A}_2^5 \cos^5(\omega_2 t) = \frac{1}{16} (10 \mathbf{A}_2^5 \cos(\omega_2 t) + 5 \mathbf{A}_2^5 \cos(3\omega_2 t) + \mathbf{A}_2^5 \cos(5\omega_2 t)) = \frac{10}{16} \mathbf{A}_2^5 \cos(\omega_2 t) + \frac{5}{16} \mathbf{A}_2^5 \cos(3\omega_2 t) + \frac{1}{16} \mathbf{A}_2^5 \cos(5\omega_2 t)
 \end{aligned}$$

$$\begin{aligned}
&= \left[ \frac{10}{16} A_1^5 \cos(\omega_1 t) + \frac{15}{8} A_2^4 A_1 \cos(\omega_1 t) + \frac{30}{8} A_1^3 A_2^2 \cos(\omega_1 t) \right] + \left[ 10 A_2^5 \cos(\omega_2 t) + \frac{15}{8} A_1^4 A_2 \cos(\omega_2 t) + \frac{30}{8} A_1^2 A_2^3 \cos(\omega_2 t) \right] + \left[ \frac{20}{16} A_1^4 A_2 \cos(2\omega_1 t - \omega_2 t) + \frac{30}{16} A_1^2 A_2^3 \cos(2\omega_1 t - \omega_2 t) \right] \\
&+ \left[ \frac{20}{16} A_1^4 A_2 \cos(2\omega_1 t + \omega_2 t) + \frac{30}{16} A_1^2 A_2^3 \cos(2\omega_1 t + \omega_2 t) \right] + \left[ \frac{20}{16} A_2^4 A_1 \cos(2\omega_2 t - \omega_1 t) + \frac{30}{16} A_1^3 A_2^2 \cos(2\omega_2 t - \omega_1 t) \right] + \left[ \frac{20}{16} A_2^4 A_1 \cos(2\omega_2 t + \omega_1 t) + \frac{30}{16} A_1^3 A_2^2 \cos(2\omega_2 t + \omega_1 t) \right] \\
&+ \left[ \frac{5}{16} A_1^5 \cos(3\omega_1 t) + \frac{10}{8} A_1^3 A_2^2 \cos(3\omega_1 t) \right] + \left[ \frac{5}{16} A_2^5 \cos(3\omega_2 t) + \frac{10}{8} A_1^2 A_2^3 \cos(3\omega_2 t) \right] + \left[ \frac{10}{16} A_1^3 A_2^2 \cos(3\omega_1 t - 2\omega_2 t) \right] + \left[ \frac{10}{16} A_1^2 A_2^3 \cos(3\omega_2 t - 2\omega_1 t) \right] \\
&+ \left[ \frac{10}{16} A_1^3 A_2^2 \cos(3\omega_1 t + 2\omega_2 t) \right] + \left[ \frac{10}{16} A_1^2 A_2^3 \cos(3\omega_2 t + 2\omega_1 t) \right] + \left[ \frac{5}{16} A_2^4 A_2 \cos(4\omega_2 t - \omega_1 t) \right] + \left[ \frac{5}{16} A_2^4 A_1 \cos(4\omega_2 t + \omega_1 t) \right] \\
&+ \left[ \frac{5}{16} A_1^4 A_2 \cos(4\omega_1 t + \omega_2 t) \right] + \left[ \frac{5}{16} A_1^4 A_2 \cos(4\omega_1 t - \omega_2 t) \right] + \left[ \frac{1}{16} A_1^5 \cos(5\omega_1 t) \right] + \left[ \frac{1}{16} A_2^5 \cos(5\omega_2 t) \right] \\
&= \frac{25}{4} \cos(\omega_1 t) + \frac{25}{4} \cos(\omega_1 t) + \frac{25}{8} \cos(2\omega_1 t - \omega_2 t) + \frac{25}{8} \cos(2\omega_1 t + \omega_2 t) + \frac{25}{8} \cos(2\omega_2 t - \omega_1 t) + \frac{25}{8} \cos(2\omega_2 t + \omega_1 t) + \frac{25}{16} \cos(3\omega_1 t) + \frac{25}{16} \cos(3\omega_2 t) + 8 \cos(3\omega_1 t - 2\omega_2 t) \\
&+ \frac{5}{8} \cos(3\omega_2 t - 2\omega_1 t) + \frac{5}{8} \cos(3\omega_1 t + 2\omega_2 t) + \frac{5}{8} \cos(3\omega_2 t + 2\omega_1 t) + \frac{5}{16} \cos(4\omega_2 t - \omega_1 t) + \frac{5}{16} \cos(4\omega_2 t + \omega_1 t) + \frac{5}{16} \cos(4\omega_1 t + \omega_2 t) + \frac{5}{16} \cos(4\omega_1 t - \omega_2 t) \\
&+ \frac{1}{16} A_1^5 \cos(5\omega_1 t) + \frac{1}{16} A_2^5 \cos(5\omega_2 t)
\end{aligned}$$

